Directional Light Scattering and Absorption Enhancement by Nanoparticles and Nanoparticle Clusters with their Applications in Solar Energy Harvesting

by

Rongheng Li

A dissertation submitted in partial fulfillment
of the requirements for the degree of
Doctor of Philosophy
(Mechanical Sciences and Engineering)
in the University of Michigan - Dearborn
2019

Doctoral Committee:

Professor Ben Q. Li, Chair
Professor Pravansu Mohanty
Professor Yasha Yi
Associate Professor Joe Fujiou Lo

Rongheng Li

rongheng@umich.edu

ORCID iD: 0000-0003-3580-7499

DEDICATION

To my father, mother and sister.

ACKNOWLEDGEMENTS

First and foremost, I would like to thank my advisor, Dr. Ben Q. Li, for all his insight, guidance and patience. His inspiring advice always encourages me to challenge difficulties. His extraordinary support during my graduate studies journey is invaluable to me.

Second, I am grateful to my thesis committee members: Dr. Pravansu Mohanty, Dr. Yasha Yi and Dr. Joe Fujiou Lo, for their insightful comments and encouragement.

I would thank all my friends and colleagues I have gained during my research journey. In particular, I would like to thank Mr. Linyan Xiang, Dachuan Wu and Huan Yang for the exhilarating discussion and memorable moments we stay together.

Finally, thank my family for supporting me throughout my Master and Ph.D. study.

TABLE OF CONTENTS

LIST OF FIGURES

ABSTRACT

This thesis presents a computational study of the directional light scattering and absorption enhancement by nanoparticles and clusters of nanoparticles. The computational algorithm is based on the Mie electromagnetic-scattering theory with the addition-theorem recursive algorithm for electromagnetic scattering particles. Nanoparticles or nanoparticle aggregates are made into forward scattering of incident light by tuning the electric and corresponding magnetic modes of each particles in the cluster. Lossless broaden band forward scattering nanoparticle cluster is designed for the photovoltaic application. These nanoparticles and nanoparticle aggregates are incorporated into thin film solar cells and their performances in harvesting solar energy are evaluated and optimized by the use of Finite-Difference Time-Domain (FDTD) numerical method. Extensive simulations were carried out to identify the directional scattering nanoparticles and/or nanoparticle aggregates and to design solar cells incorporated with these nanoparticles. Analysis was conducted, with help of both analytical and numerical solutions, to explore fundamental physical mechanism governing light-particle and inter-particle interactions in nanoparticles and nanoparticle-thin film solar systems. Computed results for various nanoparticle-thin film solar configurations demonstrate that significant enhancement of light absorption in solar cell absorption can be obtained with the directional scattering nanoparticle and/or nanoparticle clusters over the solar cells enhanced by non-directional scattering particles reported in literature.

CHAPTER 1

Introduction

1.1 Motivation

Solar energy refers to the radiant light from the Sun, which can be collected and utilized with a range of technologies i.e., photovoltaic [1], solar thermal collector [2] and solar chemical process [3]. Recently, thin film silicon solar cell is studied as one potential class of photovoltaics to replace the crystalline silicon panels in present use [4]. A great advantage of the thin film cell technology is that the overall thickness is about 1/100 that of a typical crystal silicon cell. This translates into significant savings in materials and manufacturing costs, let along the environment impact. A crucial problem that has constrained the wide acceptance of the thin-film cell is its relatively low energy conversion efficiency. Consequently, enhancing the solar conversion efficiency of these cells is an important research subject in both theory and experiment. Among all different types of the energy losses throughout the entire energy converting processes, the absorption loss accounts for a significant portion. Different approaches have been proposed to increase the light absorption inside the thin film solar cells so as to increase the conversion efficiency. Distinct classes of nanostructures, i.e., honeycomb textured substrates [5-7], nano-photonic structures [8-10], moth-eye structures [11-13], metal nanoparticle arrays [14,15], nanocylinders [16], nanopillar [17], nanogratings [18] and photon upconversion materials [19], have been proposed for solar harvesting with some success.

Plasmonic nanostructures have engendered extraordinary interest for its unique energy conversion properties [20]. The outstanding absorption at the desired frequency is beneficial for

various applications, i.e., biosensing [21-23], hyperthermia therapy [24-26], solar water splitting [27-29], solar desalination [30-32] and optofluidic control [33-35]. The mechanism behind is localized surface plasmon resonance (LSPR), which originates from the collective oscillation of electrons. As the development of computing science and nanotechnology, lots of simulations and experiments focused on plasmonic nanostructures are implemented. Distinct classes of nanostructures, i.e., nanospheres, nanolens [36-38], nanobowls [39-41], nanogratings [42-44] and nanorods [45-47] are utilized for boosting the absorption in different applications. The optical behavior of each configuration is differed by a couple of parameters such as shape, size and material, which could be determined according to different applications.

1.2 Literature Review

Nanospherical structures with two distinct functions, i.e. directional light scattering or light absorption enhancement, are investigated and developed for the solar energy application.

For the first class, nanospherical particles with plasmonic effects, i.e., metal nanoparticles, are one of the most widely studied nanostructures for solar applications because of its relatively large scattering ability. A vast amount of published work, including simulations and experiments, focuses on trapping the light into different types of solar cells by incorporating various nanospherical structure, i.e., nanospheres, nanoshells and core/shell nanostructures. Beak et al. incorporated Ag nanoparticles into the anodic buffer layer of organic photovoltaic, which provided abundant light absorption enhancement to the active layer [48]. Qu et al. employed Au-citrate core/shell nanoparticles in the absorption layer of thin film organic photovoltaic, which led to 110% enhancement of the light [49]. Moreover, the metal core and the absorption layer are detached by the dielectric shell, which prevents the metal to be the recombination center. Grandidier et al. applied nanosphere array of dielectric material atop of thin film amorphous silicon solar cell [50],

where the whisper-gallery modes are excited. The light is guided to the cells, which significantly enhances the absorption. Meanwhile, the utilization of the dielectric material can avoid the heat loss which occurs in the case of metal nanoparticle. Yang et al. designed a silicon thin-film solar cell configuration with partially embedded SiO_2 spheres on the front side [51]. The optimized half-embedded spheres show a broadband, wide angle, and strong optical absorption with more than 56% enhancement in light-conversion efficiency. Wang et al. further enhanced the light absorption by utilizing high refractive index nanoparticle arrays. The SiO_2, Si_3N4 and TiO_2 nanosphere arrays are applied atop thin film silicon solar cells [52]. The light absorption enhancement with the arrangement of these particles is attributed to the coupling of incident light into transverse electric waveguide modes in the silicon thin film. They found that the higher refractive index, the more enhancement of light trapping.

Vast of work is also conducted for the second class, which absorbs significant solar energy by the nanoparticles and releases to the surrounding medium. Structures such as nanospheres, nanoshells and nano core/shell particles are intensively investigated in both theory and experiment. Liu et al. investigated the energy absorption enhancement using gold nanoshells in hyperthermia therapy application [53]. According to the calculations for different forms of nanoshells, i.e., 1-D chains, 2-D arrays, and 3-D clusters, they showed that the interparticle distance influences both field enhancement and surface plasmon resonance position. Olson et al. synthesized hollow gold-silver double-shell nanospheres and characterized the optical properties [54]. The combination of the two metal shells broadened the absorption profile. Ge et al. fabricated Au/SiO2 nanoparticles with the dielectric layer thickness various from 15 to 45 nm. They demonstrated that the surface plasmon resonance absorption peak can be shifted to red via increase Au particle size or SiO_2 thickness. Wang et al. studied the thermal conversion efficiency of solar energy by dispersing

carbon-gold core/shell nanoparticles in water [55]. The resulting solar absorption efficiency factor reaches 1.5 for the spherical case. This is attributed to field enhancement by the localized plasmon resonance at the surface of the gold layer, which leads to the enhancement of the absorption inside the carbon core. Ishii *et al.* fabricated germanium nanoparticles through reactive thermal arc plasma method [56]. Strong Mie resonance enhanced light absorption is observed, which is applicable for water heating and vaporization.

The above works showed light absorption performance could be enhanced by various nanospherical core/shell structures and different materials, i.e., metals and dielectric layers. The physical mechanisms behind can be explained in two aspects. First, the total absorption is mainly from the electric dipole, which is generated from the metal materials. Second, the addition of lossless dielectric layer moves the absorption peak while has no contribution to the total absorption efficiency because that the imaginary part of its refractive index is nearly zero.

1.3 Objectives of Present Research

The two major objectives of this research are to develop presents a general methodology for design and application of the forward or backward scattering nanoparticle cluster for enhancement of absorption in thin-film Si solar cells, and design core/shell nanoparticle aggregate with superior absorption for solar thermal application.

For light scattering nanoparticles, various numerical studied are implemented. The lossless nanoparticle array so designed, with its refractive index twice as that of the medium, possesses excellent forward scattering over a wide wavelength range. The peak wavelength of the scattering efficiency can be tuned by changing the radius of the nanospheres. Moreover, the energy can be further scattered into the solar cell by partially burying the nanoparticle inside the silicon slab. To verify the feasibility of the developed nanostructure for the solar application, the complete optical

and electrical processes for the entire configuration are simulated by using Lumerical FDTD software package. The result reveals that the light absorption enhancement of the active layer is much more pronounced than that with other popular classes of nanostructures, i.e., Ag nanoparticle, moth eye structure and honeycomb structure on the same dimensional scale.

For light absorbing nanoparticles, we propose a metal-semiconductor core/shell nanospherical particles, which exhibits both electric and magnetic dipoles. That is, the magnetic dipole component, which comes from the semiconductor material, can also contribute to the total absorption. By varying the thickness of each layer, the peak of the electric and magnetic dipoles can be tuned to the same wavelength. In other word, without losing the tunable peak wavelength feature, the total absorption efficiency at the specific wavelength can be largely enhanced compared to the situation of metal-dielectric core/shell structures. Moreover, the overlapping feature of the developed core/shell nanoparticle can be held for different wavelength regions for the different application by simply changing the thickness of each layer. In addition, this feature can also be obtained for different surrounding media, i.e., air and water.

1.4 Scope of Present Research

In this study, seven sections are discussed. Chapter 2 presents the mathematical description of the physical phenomena. Chapter 3 lists the analytical solution and numerical simulation methodology of the governing equations for the designed nanostructures. Chapter 4 presents the forward scattering nanoparticle cluster and its application in thin film Si solar cells. Chapter 5 discusses the light absorption enhancement of GaAs solar cell with combined structure consists of forward scattering particles and backward scattering nanograting. Chapter 6 depicts the light absorbing core/shell nanoparticles, which can be applied for solar thermal energy application. Chapter 7 presents the backward scattering nanoparticle clusters.

CHAPTER 2

Problem Statement

Let us consider a cluster of particles shown in Figure 2.1, where multilayered core/shell nanoparticles are placed at different positions. An incident light with **k** as the traveling direction strikes the nanoshell aggregates. As a result, a portion of the light is absorbed inside the nanoparticles, while the other portion is scattered towards other particles. This process repeats until the light finally escapes from the overall cluster.

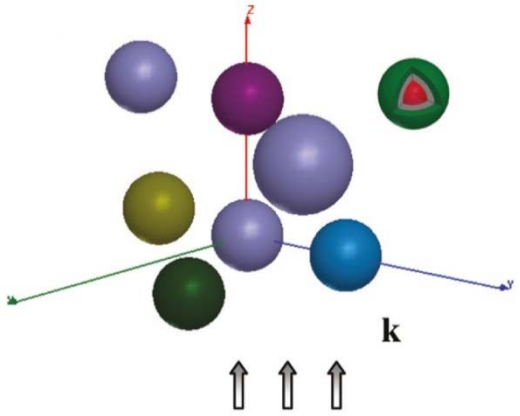

Figure 2.1: Electromagnetic multiscattering by multilayered multiparticles

The optical phenomenon of light incident onto a cluster of spherical nanoparticles is described by the Maxwell equations. In a source free region, the Maxwell equations reduce to the wave equations [57],

$$\nabla^2\mathbf{E} + k^2\mathbf{E} = \mathbf{0}, \nabla\cdot\mathbf{E} = 0, \mathbf{B} = -(i/\omega)\nabla\times\mathbf{E} \tag{2.1}$$

$$\nabla^2\mathbf{B} + k^2\mathbf{B} = \mathbf{0}, \nabla\cdot\mathbf{B} = 0, \mathbf{E} = -(i/\omega)\nabla\times\mathbf{E} \tag{2.2}$$

where **E** and **H** correspond to the electric and magnetic fields, and $k^2 = \omega m/c$ with m being the refractive index and c the speed of light. The procedure of obtaining the analytical solution to equations (1) and (2) for the system in Figure 2.1 involves the Mie solution for a single particle and the vector addition theorem. For solar energy application, the optical process of the entire structure, which includes the designed nanoparticle cluster and solar cell film, can be simulated numerically by utilizing the Finite-Difference Time-Domain (FDTD) method. The detailed procedures for both analytical and numerical methods are explained in the following chapter.

CHAPTER 3

Methodology

The analytical and numerical solution to the Maxwell equations are briefly presented in the following consequence. The analytical solution to the light scattering by a single solid sphere is demonstrated firstly. The solution is further extended to multilayered sphere, multiple sphere and multiple multilayered particles. To obtain pleasurable convergence and reduce the calculation, the recursive algorithm for multilayered sphere is demonstrated. Moreover, the first Kerker's condition, which is used for maximized forward and minimized backward, is presented. In addition, the numerical FDTD (finite-difference time-domain) method is described. The accuracy is validated by comparing the light scattering efficiency of a single Ag nanoparticle with that of the analytical solution.

3.1 Analytical Solution

3.1.1 Light Scattering by a Solid Nanosphere

The analytical study of the light absorption and scattering by a sphere is derived by the Mie theory [58], which solves the Maxwell equations for a sphere in spherical coordinate. The plane wave is expanded in spherical coordinate, followed by applying the boundary conditions between the sphere and the surrounding media. Then the system equations can be formed, and the scattering coefficients are obtained by solving the system equations.

To develop the solutions for electric and magnetic field **E** and **B**, the scalar wave equation is considered firstly.

$$\nabla^2\psi + k^2\psi = 0 \tag{3.1}$$

The solution of the scalar wave equation can be obtained by the method of separation of variables,

$$\psi = \sum_{l=0}^{\infty}\sum_{m=-1}^{m=1}(A_{lm}j_l(kr)+B_{lm}y_l(kr))p_l^m(\theta)e^{im\phi} = \sum_{l=0}^{\infty}\sum_{m=-1}^{m=1}(A'_{lm}j_l(kr)+B'_{lm}y_l(kr))Y_{lm}(\theta,\varphi) \quad (3.2)$$

where $j_l(kr)$ and $y_l(kr)$ are the first and second kind of spherical Bessel functions, and Y_{lm} is the spherical harmonics.

Then, the divergence free condition

$$\begin{aligned}\nabla\cdot\mathbf{E}&=0\\ \nabla\cdot\mathbf{B}&=0\end{aligned} \quad (3.3)$$

is satisfied by constructing functions from the scalar wave functions, which is defined as below,

$$\mathbf{M}=\nabla\times(r\psi),\quad N=k^{-1}\nabla\times\mathbf{M}=k^{-1}\nabla\times\nabla\times(r\psi) \quad (3.4)$$

The divergence free condition can be easily proved since the dot on a curl is always zero. The solutions for the electric filed **E** and the magnetic field **B** are further constructed,

$$\mathbf{E}=\sum_{l=1}^{\infty}\sum_{m=-1}^{m=1}(a_{lm}\mathbf{M}+b_{lm}\mathbf{N})$$

$$\mathbf{B}=-(i/\omega)\nabla\times\mathbf{E}=-(i/\omega)\sum_{l=1}^{\infty}\sum_{m=-1}^{m=1}(a_{lm}\nabla\times\mathbf{M}+b_{lm}\nabla\times\mathbf{N})=-(ik/\omega)\sum_{l=1}^{\infty}\sum_{m=-1}^{m=1}(a_{lm}\mathbf{N}+b_{lm}\mathbf{M}) \quad (3.5)$$

By introducing $\mathbf{X}_{lm}$ function,

$$\mathbf{X}_{lm}(\theta,\varphi)=\frac{1}{\sqrt{l(l+1)}}\mathbf{L}Y_{lm}(\theta,\varphi) \quad (3.6)$$

where **L** is the angular momentum operator,

$$\mathbf{L}=-ir\times\nabla=-ir\times\left(\hat{e}_r\frac{\partial}{\partial r}+\hat{e}_\theta\frac{1}{r}\frac{\partial}{\partial\theta}+\hat{e}_\varphi\frac{1}{r\sin\theta}\frac{\partial}{\partial\varphi}\right)=-i\hat{e}_\varphi\frac{\partial}{\partial\theta}+i\hat{e}_\theta\frac{1}{\sin\theta}\frac{\partial}{\partial\varphi}; \quad (3.7)$$

The **M** and **N** functions can be expresses by $\mathbf{X}_{lm}$,

$$\mathbf{M}_{lm} = -r \times \nabla \psi_{lm} = -i\mathbf{L}\psi_{lm} = -i\sqrt{l(l+1)}\, j_l(kr)\mathbf{X}_{lm}(\theta,\varphi)$$

$$\mathbf{N}_{lm} = k^{-1}\nabla \times \mathbf{M}_{lm} = -ik^{-1}\nabla \times (j_l(kr)\mathbf{X}_{lm}(\theta,\varphi))\sqrt{l(l+1)} \tag{3.8}$$

The electromagnetic fields may then be written as

$$\mathbf{E} = \sum_{l=1}^{\infty}\sum_{m=-1}^{m=1}(c_{lm} j_l(kr)\mathbf{X}_{lm} + d_{lm}k^{-1}\nabla \times (j_l(kr)\mathbf{X}_{lm})),$$

$$\mathbf{H} = -(i/\omega\mu)\nabla \times \mathbf{E} = -\frac{ik}{\omega\mu}\sum_{l=1}^{\infty}\sum_{m=-1}^{m=1}(c_{lm}k^{-1}\nabla \times (j_l(kr)\mathbf{X}_{lm}) + d_{lm} j_l(kr)\mathbf{X}_{lm}) \tag{3.9}$$

For a solid sphere, the income, internal and scattered fields are further expressed as

$$\mathbf{E}_i = \sum_{l=1}^{\infty}(c^i_{l,\pm} j_l(kr)\mathbf{X}_{l,\pm1} + d^i_{l,\pm}k^{-1}\nabla \times (j_l(kr)\mathbf{X}_{l,\pm1}))$$

$$\mathbf{H}_i = -(i/\omega\mu)\nabla \times \mathbf{E}_s = -\frac{ik}{\omega\mu}\sum_{l=1}^{\infty}\left(c^i_{l,\pm}k^{-1}\nabla \times (j_l(kr)\mathbf{X}_{l,\pm1}) + d^i_{l,\pm} j_l(kr)\mathbf{X}_{l,\pm1}\right)$$

$$\mathbf{E}_c = \sum_{l=1}^{\infty}(c^c_{l,\pm} j_l(kr)\mathbf{X}_{l,\pm1} + d^c_{l,\pm}k^{-1}\nabla \times (j_l(kr)\mathbf{X}_{l,\pm1}))$$

$$\mathbf{H}_c = -(i/\omega\mu)\nabla \times \mathbf{E}_a = -\frac{ik}{\omega\mu}\sum_{l=1}^{\infty}\left(c^c_{l,\pm}k^{-1}\nabla \times (j_l(kr)\mathbf{X}_{l,\pm1}) + d^c_{l,\pm} j_l(kr)\mathbf{X}_{l,\pm1}\right)$$

$$\mathbf{E}_s = \sum_{l=1}^{\infty}(c^s_{l,\pm} h^{(1)}_l(kr)\mathbf{X}_{l,\pm1} + d^s_{l,\pm}k^{-1}\nabla \times (h^{(1)}_l(kr)\mathbf{X}_{l,\pm1}))$$

$$\mathbf{H}_s = -(i/\omega\mu)\nabla \times \mathbf{E}_s = -\frac{ik}{\omega\mu}\sum_{l=1}^{\infty}\left(c^s_{l,\pm}k^{-1}\nabla \times (h^{(1)}_l(kr)\mathbf{X}_{l,\pm1}) + d^s_{l,\pm} h^{(1)}_l(kr)\mathbf{X}_{l,\pm1}\right) \tag{3.10}$$

where h_l is the Hankel functions, which is more suitable for the scattered field since it represents an outgoing wave. Subscripts *i*, *c* and *s* represent the income, inside the sphere and scattered field, respectively.

By assuming the surrounding medium to be vacuum and plugging the expression of all the field components to the boundary conditions at the interface between the sphere and surrounding medium,

$$(\mathbf{E}_s + \mathbf{E}_i)\times\mathbf{n} = \mathbf{E}_c \times\mathbf{n}, \qquad (\mathbf{H}_s + \mathbf{H}_i)\times\mathbf{n} = \mathbf{H}_c \times\mathbf{n} \tag{3.11}$$

the system equations can be formed as

$$\begin{aligned} c^s_{l,\pm1}\xi_l(x)m + c^i_{l,\pm1}\psi_l(x)m &= c^c_{l,\pm1}\psi_l(mx) \\ d^s_{l,\pm1}\xi'_l(x)m + d^i_{l,\pm1}\psi'_l(x)m &= d^c_{l,\pm1}\psi'_l(mx) \\ c^s_{l,\pm1}\xi'_l(x) + c^i_{l,\pm1}\psi'_l(x) &= c^c_{l,\pm1}\psi'_l(mx) \\ d^s_{l,\pm1}\xi_l(x) + d^i_{l,\pm1}\psi_l(x) &= d^c_{l,\pm1}\psi_l(mx) \end{aligned} \tag{3.12}$$

with $\psi_n(\rho) = \rho j_n(\rho), \qquad \chi_n(\rho) = -\rho y_n(\rho), \qquad \xi(\rho) = \rho h^{(1)}_n(\rho) = \psi_n(\rho) - i\chi_n(\rho)$

The coefficients are obtained by solving the system equations,

$$c^c_{l,\pm1} = c^i_{l,\pm1}\frac{m\psi_l(x)\xi'_l(x) - m\psi'_l(x)\xi_l(x)}{\psi_l(mx)\xi'_l(x) - m\psi'_l(mx)\xi_l(x)}, \qquad c^s_{l,\pm1} = -c^i_{l,\pm1}\frac{\psi_l(mx)\psi'_l(x) - m\psi'_l(mx)\psi_l(x)}{\psi_l(mx)\xi'_l(x) - m\psi'_l(mx)\xi_l(x)}$$

$$d^c_{l,\pm1} = d^i_{l,\pm1}\frac{m\psi_l(x)\xi'_l(x) - m\psi'_l(x)\xi_l(x)}{m\psi_l(mx)\xi'_l(x) - \psi'_l(mx)\xi_l(x)}, \qquad d^s_{l,\pm1} = -d^i_{l,\pm1}\frac{m\psi_l(mx)\psi'_l(x) - \psi'_l(mx)\psi_l(x)}{m\psi_l(mx)\xi'_l(x) - \psi'_l(mx)\xi_l(x)} \tag{3.13}$$

The time-average flow of scattered energy is obtained by integrating the scattered Poynting vector,

$$W_{sca} = 0.5\mathrm{Re}\int_{4\pi}(\mathbf{E}_s \times \mathbf{H}_s^{*})\cdot\mathbf{n}r^2 d\Omega = \frac{0.5}{\omega\mu k}\sum_{l=1}^{\infty}\left(c^{*s}_{l,\pm1}c^s_{l,\pm1} + d^{*s}_{l,\pm1}d^s_{l,\pm1}\right) \tag{3.14}$$

The scattering cross section is defined by the ratio of the scattered energy and the intensity of the income electromagnetic wave I_{inc},

$$C_{sca} = \frac{W_{sca}}{I_{inc}} = \frac{1}{k^2E_0^2}\sum_{l=1}^{\infty}\sum_{m=-1}^{1}\left(c^{*s}_{lm}c^s_{lm} + d^{*s}_{lm}d^s_{lm}\right) \tag{3.15}$$

The scattering efficiency is the scattering cross section divided by the geometrical cross-section πa^2,

$$Q_{\text{sca}} = \frac{C_{\text{sca}}}{\pi a^2} = \frac{1}{\pi a^2 k^2 E_0^2} \sum_{l=1}^{\infty} \sum_{m=-1}^{1} \left(c_{lm}^{*s} c_{lm}^{s} + d_{lm}^{*s} d_{lm}^{s} \right) \tag{3.16}$$

3.1.2 Light Scattering by a Nanoshell or Coated Nanoparticle

To obtain the solution for the scattering of a coated sphere, the boundary condition between the core and the shell should be considered. Assume the solid core with radius a and a shell with radius b. The related fields are expanded as follows,

$$\begin{aligned}
&\mathbf{E}_s = \sum_{l=1}^{\infty} (c_{l,\pm1}^{s} h_l^{(1)}(kr)\mathbf{X}_{l,\pm1} + d_{l,\pm1}^{s} k^{-1} \nabla \times (h_l^{(1)}(kr)\mathbf{X}_{l,\pm1})) \\
&\mathbf{H}_s = -(i/\omega\mu)\nabla \times \mathbf{E}_s = -\frac{ik}{\omega\mu} \sum_{l=1}^{\infty} \left(c_{l,\pm1}^{s} k^{-1} \nabla \times (h_l^{(1)}(kr)\mathbf{X}_{l,\pm1}) + d_{l,\pm1}^{s} h_l^{(1)}(kr)\mathbf{X}_{l,\pm1} \right) \\
&\mathbf{E}_i = \sum_{l=1}^{\infty} (c_{l,\pm1}^{i} j_l(kr)\mathbf{X}_{l,\pm1} + d_{l,\pm1}^{i} k^{-1} \nabla \times (j_l(kr)\mathbf{X}_{l,\pm1})) \\
&\mathbf{H}_i = -(i/\omega\mu)\nabla \times \mathbf{E}_s = -\frac{ik}{\omega\mu} \sum_{l=1}^{\infty} \left(c_{l,\pm1}^{i} k^{-1} \nabla \times (j_l(kr)\mathbf{X}_{l,\pm1}) + d_{l,\pm1}^{i} j_l(kr)\mathbf{X}_{l,\pm1} \right) \\
&\mathbf{E}_c = \sum_{l=1}^{\infty} (c_{l,\pm1}^{c} j_l(kr)\mathbf{X}_{l,\pm1} + d_{l,\pm1}^{c} k^{-1} \nabla \times (j_l(kr)\mathbf{X}_{l,\pm1})) \\
&\mathbf{H}_c = -(i/\omega\mu)\nabla \times \mathbf{E}_c = -\frac{ik}{\omega\mu} \sum_{l=1}^{\infty} \left(c_{l,\pm1}^{c} k^{-1} \nabla \times (j_l(kr)\mathbf{X}_{l,\pm1}) + d_{l,\pm1}^{c} j_l(kr)\mathbf{X}_{l,\pm1} \right)
\end{aligned} \tag{3.17}$$

$$\begin{aligned}
&\mathbf{E}_h = \sum_{l=1}^{\infty} (f_{l,\pm1}^{h} j_l(kr)\mathbf{X}_{l,\pm1} + g_{l,\pm1}^{h} k^{-1} \nabla \times (j_l(kr)\mathbf{X}_{l,\pm1}) + v_{l,\pm1}^{h} y_l(kr)\mathbf{X}_{l,\pm1} + w_{l,\pm1}^{h} k^{-1} \nabla \times (y_l(kr)\mathbf{X}_{l,\pm1})) \\
&\mathbf{H}_h = -(i/\omega\mu)\nabla \times \mathbf{E}_h = -\frac{ik}{\omega\mu} \sum_{l=1}^{\infty} (f_{l,\pm1}^{h} k^{-1} \nabla \times (j_l(kr)\mathbf{X}_{l,\pm1}) + g_{l,\pm}^{h} j_l(kr)\mathbf{X}_{l,\pm1} + v_{l,\pm1}^{h} k^{-1} \nabla \times (y_l(kr)\mathbf{X}_{l,\pm1}) + w_{l,\pm1}^{h} y_l(kr)\mathbf{X}_{l,\pm1})
\end{aligned}$$

where subscripts *i*, *h*, c and *s* represent the income wave, field in shell, field inside the core and scattered field, respectively. By plugging the expression of all the field components to the boundary conditions at the core/shell interface and the shell-medium interface,

$$\begin{aligned}
&\mathbf{E}_h \times \mathrm{n} = \mathbf{E}_c \times \mathrm{n}, \qquad &&\mathbf{H}_h \times \mathrm{n} = \mathbf{H}_c \times \mathrm{n}, \qquad at \;\; r = a \\
&(\mathbf{E}_s + \mathbf{E}_i) \times \mathrm{n} = \mathbf{E}_h \times \mathrm{n}, \qquad &&(\mathbf{H}_s + \mathbf{H}_i) \times \mathrm{n} = \mathbf{H}_h \times \mathrm{n}, \qquad at \;\; r = b
\end{aligned} \tag{3.18}$$

the system equations can be formed as

$$f^h_{l,\pm1}\psi_l(m_2x)m_1 + v^h_{l,\pm1}\chi_l(m_2x)m_1 - c^c_{l,\pm1}\psi_l(m_1x)m_2 = 0$$

$$g^h_{l,\pm1}\psi\,'(m_2x)m_1 + w^h_{l,\pm1}\chi\,'(m_2x)m_1 - d^c_{l,\pm1}\psi\,'(m_1x)m_2 = 0 \tag{3.19}$$

$$f^h_{l,\pm1}\psi_l\,'(m_2x) + v^h_{l,\pm1}\chi_l\,'(m_2x) - c^c_{l,\pm1}\psi_l\,'(m_1x) = 0$$

$$g^h_{l,\pm1}\psi_l(m_2x) + w^h_{l,\pm1}\chi_l(m_2x) - d^c_{l,\pm1}\psi_l(m_1x) = 0$$

$$f^h_{l,\pm1}\psi_l(m_2y) + v^h_{l,\pm1}\chi_l(m_2y) - c^s_{l,\pm1}\xi_l(y)m_2 = c^i_{l,\pm1}\psi_l(y)m_2$$

$$g^h_{l,\pm1}\psi_l\,'(m_2y) + w^h_{l,\pm1}\chi_l\,'(m_2y) - d^s_{l,\pm1}\xi_l\,'(y)m_2 = d^i_{l,\pm1}\psi_l\,'(y)m_2$$

$$f^h_{l,\pm1}\psi_l\,'(m_2y) + v^h_{l,\pm1}\chi_l\,'(m_2y) - c^s_{l,\pm1}\xi_l\,'(y) = c^i_{l,\pm1}\psi_l\,'(y)$$

$$g^h_{l,\pm1}\psi_l(m_2y) + w^h_{l,\pm1}\chi_l(m_2y) - d^s_{l,\pm1}\xi_l(y) = d^i_{l,\pm1}\psi_l(y)$$

The coefficients are obtained by solving the system equations,

$$c^s_{l,\pm1} = -c^i_{l,\pm1}\frac{m_2\psi_l(y)[\psi_l\,'(m_2y) - B_l\chi_l\,'(m_2y)] - \psi_l\,'(y)[\psi_l(m_2y) - B_l\chi_l(m_2y)]}{m_2\xi_l(y)[\psi_l\,'(m_2y) - B_l\chi_l\,'(m_2y)] - \xi_l\,'(y)[\psi_l(m_2y) - B_l\chi_l(m_2y)]}$$

$$c^c_{l,\pm1} = \frac{-c^i_{l,\pm1}m_2[\psi_l(y)\xi_l\,'(y) - \psi_l\,'(y)\xi_l(y)][\psi_l\,'(m_2x) - B_l\chi_l\,'(m_2x)]}{\psi_l\,'(m_1x)\{m_2\xi_l(y)[\psi_l\,'(m_2y) - B_l\chi_l\,'(m_2y)] - \xi_l\,'(y)[\psi_l(m_2y) - B_l\chi_l(m_2y)]\}}$$
$$= \frac{c^i_{l,\pm1}m_1m_2[\psi_l(y)\xi_l\,'(y) - \psi_l\,'(y)\xi_l(y)][\psi_n(m_2x)\chi_n\,'(m_2x) - \psi_n\,'(m_2x)\chi_n(m_2x)]}{C_l\,\{m_2\xi_l(y)[\psi_l\,'(m_2y) - B_l\chi_l\,'(m_2y)] - \xi_l\,'(y)[\psi_l(m_2y) - B_l\chi_l(m_2y)]\}}$$

$$d^s_{l,\pm1} = -d^i_{l,\pm1}\frac{\psi_l(y)[\psi_l\,'(m_2y) - A_l\chi_l\,'(m_2y)] - m_2\psi_l\,'(y)[\psi_l(m_2y) - A_l\chi_l(m_2y)]}{\xi_l(y)[\psi_l\,'(m_2y) - A_l\chi_l\,'(m_2y)] - m_2\xi_l\,'(y)[\psi_l(m_2y) - A_l\chi_l(m_2y)]}$$

$$d^c_{l,\pm1} = \frac{d^i_{l,\pm1}m_2[\xi_l\,'(y)\psi_l(y) - \xi_l(y)\psi_l\,'(y)][\psi_l(m_2x) - A_l\chi_l(m_2x)]}{\psi_l(m_1x)\{\xi_l(y)[\psi_l\,'(m_2y) - A_l\chi_l\,'(m_2y)] - m_2\xi_l\,'(y)[\psi_l(m_2y) - A_l\chi_l(m_2y)]\}}$$
$$= \frac{d^i_{l,\pm1}m_1m_2[\chi_l\,'(m_2x)\psi_l(m_2x) - \chi_l(m_2x)\psi_l\,'(m_2x)][\xi_l\,'(y)\psi_l(y) - \xi_l(y)\psi_l\,'(y)]}{D_l\,\{\xi_l(y)[\psi_l\,'(m_2y) - A_l\chi_l\,'(m_2y)] - m_2\xi_l\,'(y)[\psi_l(m_2y) - A_l\chi_l(m_2y)]\}} \tag{3.20}$$

$$f^c_{l,\pm1} = \frac{-c^i_{l,\pm1}m_2[\psi_l(y)\xi_l\,'(y) - \psi_l\,'(y)\xi_l(y)]}{m_2\xi_l(y)[\psi_l\,'(m_2y) - B_l\chi_l\,'(m_2y)] - \xi_l\,'(y)[\psi_l(m_2y) - B_l\chi_l(m_2y)]}$$

$$v_{l,\pm1}^{h}=\frac{-c_{l,\pm1}^{i}m_2B_l[\psi_l(y)\xi_l\,'(y)-\psi_l\,'(y)\xi_l(y)]}{m_2\xi_l(y)[\psi_l\,'(m_2y)-B_l\chi_l\,'(m_2y)]-\xi_l\,'(y)[\psi_l(m_2y)-B_l\chi_l(m_2y)]}$$

$$g_{l,\pm1}^{h}=\frac{-d_{l,\pm1}^{i}m_2[\xi_l\,'(y)\psi_l(y)-\xi_l(y)\psi_l\,'(y)]}{\xi_l(y)[\psi_l\,'(m_2y)-A_l\chi_l\,'(m_2y)]-m_2\xi_l\,'(y)[\psi_l(m_2y)-A_l\chi_l(m_2y)]}$$

$$w_{l,\pm1}^{h}=\frac{-d_{l,\pm1}^{i}m_2A_l[\xi_l\,'(y)\psi_l(y)-\xi_l(y)\psi_l\,'(y)]}{\xi_l(y)[\psi_l\,'(m_2y)-A_l\chi_l\,'(m_2y)]-m_2\xi_l\,'(y)[\psi_l(m_2y)-A_l\chi_l(m_2y)]}$$

where

$$A_l=\frac{m_2\psi_l(m_2x)\psi_l\,'(m_1x)-m_1\psi_l\,'(m_2x)\psi_l(m_1x)}{m_2x_l(m_2x)\psi_l\,'(m_1x)-m_1x_l\,'(m_2x)\psi_l(m_1x)}$$

$$B_l=\frac{m_2\psi_l(m_1x)\psi_l\,'(m_2x)-m_1\psi_l\,'(m_1x)\psi_l(m_2x)}{m_2x_l\,'(m_2x)\psi_l(m_1x)-m_1x_l(m_2x)\psi_l\,'(m_1x)} \tag{3.21}$$

$$C_n=m_2x_n\,'(m_2x)\psi_n(m_1x)-m_1x_n(m_2x)\psi_n\,'(m_1x)$$

$$D_l=m_2x_l(m_2x)\psi_l\,'(m_1x)-m_1x_l\,'(m_2x)\psi_l(m_1x)$$

3.1.3 Recursive Algorithm for Multilayered Nanoparticle

For multilayered spherical structure, the number of the obtained system equations is increased with the number of the layers. To obtain pleasurable convergence and reduce the calculation, the recursive algorithm for multilayered sphere is introduced [59]. For a core/shell particle with totally l layers, the electric and magnetic field of lth layer can be expanded,

$$\mathbf{E}_l=\sum_{n=1}^{\infty}E_n[c_n^l\mathbf{M}_{o1n}^{(1)}-id_n^l\mathbf{N}_{e1n}^{(1)}+ia_n^l\mathbf{N}_{e1n}^{(3)}-b_n^l\mathbf{M}_{o1n}^{(3)}]$$

$$\mathbf{H}_l=-\frac{k_l}{\omega\mu}\sum_{n=1}^{\infty}E_n[d_n^l\mathbf{M}_{e1n}^{(1)}+ic_n^l\mathbf{N}_{o1n}^{(1)}-ib_n^l\mathbf{N}_{o1n}^{(3)}-b_n^l\mathbf{M}_{e1n}^{(3)}] \tag{3.22}$$

The boundary condition between lth layer and (l+1)th layer is as following form,

$$(\mathbf{E}_{l+1}-\mathbf{E}_l)\times\hat{\mathbf{e}}_r = 0$$
$$(\mathbf{H}_{l+1}-\mathbf{H}_l)\times\hat{\mathbf{e}}_r = 0 \tag{3.23}$$

By substitution and solving the system equation, the efficiencies for the lth layer can be obtained as

$$d_n^l = d_n^{l+1}\frac{\psi_n(m_{l+1}x_1)-A_n^{l+1}\zeta_n(m_{l+1}x_1)}{\psi_n(m_lx_1)-A_n^l\zeta_n(m_lx_1)}$$
$$c_n^l = c_n^{l+1}\frac{m_l}{m_{l+1}}\frac{\psi_n(m_{l+1}x_1)-B_n^{l+1}\zeta_n(m_{l+1}x_1)}{\psi_n(m_lx_1)-B_n^l\zeta_n(m_lx_1)} \tag{3.24}$$
$$c_n^{L+1} = d_n^{L+1} = 1$$

where $A_n^l = \beta_n^l / d_n^l \quad B_n^l = \alpha_n^l / c_n^l$

Then, the recursion method starts with

$$A_n^l = B_n^l = 0$$

$$A_n^{l+1} = R_n(m_{l+1}x_1)\frac{m_{l+1}H_n^a(m_lx_l)-m_lD_n^{(1)}(m_{l+1}x_l)}{m_{l+1}H_n^a(m_lx_l)-m_lD_n^{(3)}(m_{l+1}x_l)}$$
$$B_n^{l+1} = R_n(m_{l+1}x_1)\frac{m_lH_n^b(m_lx_l)-m_{l+1}D_n^{(1)}(m_{l+1}x_l)}{m_lH_n^b(m_lx_l)-m_{l+1}D_n^{(3)}(m_{l+1}x_l)} \tag{3.25}$$

where

$$H_n^a(m_1x_1) = H_n^b(m_1x_1) = D_n^{(1)}(m_1x_1)$$
$$H_n^a(m_1x_1)\frac{R_n(m_1x_1)D_n^{(1)}(m_1x_1)-A_n{}^lD_n^{(3)}(m_1x_1)}{R_n(m_1x_1)-A_n{}^l}$$
$$H_n^b(m_1x_1)\frac{R_n(m_1x_1)D_n^{(1)}(m_1x_1)-B_n{}^lD_n^{(3)}(m_1x_1)}{R_n(m_1x_1)-A_n{}^l}$$

$$D_n^{(1)}(z) = \psi_n'(z)/\psi_n(z) \tag{3.26}$$
$$D_n^{(3)}(z) = \zeta_n'(z)/\zeta_n(z)$$

$$R_n(z) = \psi_n(z) / \zeta_n(z)$$

$d_n^l, c_n^l, \alpha_n^l,$ and β_n^l are then determined from A_n^l and B_n^l

3.1.4 Light Scattering by Multiple Nanospheres

For the multiparticle system, the income electromagnetic field for an individual particle is the summation of the income field and the scattered field from other particles. During the step for applying the boundary conditions, the vector addition theorem [60, 61] is applied to translate all the wave functions of other particles to the origin of the certain particle. The vector addition theorem for the spherical wave functions are derived as follows.

The solution of the scalar Helmholtz equation,

$$(\nabla^2 + k^2)u = 0 \tag{3.27}$$

is $u_{nm}^{(1)}(\mathbf{r}) = j_n(kr)Y_{nm}(\hat{\mathbf{r}})$, which has the integral representation,

$$u_{nm}^{(1)}(\mathbf{r}) = \frac{1}{4\pi i^n} \int Y_{nm}(\hat{\mathbf{k}}) \exp(i\mathbf{k} \cdot \mathbf{r})\, d\hat{\mathbf{k}}$$

For the coordinates defined as follows,

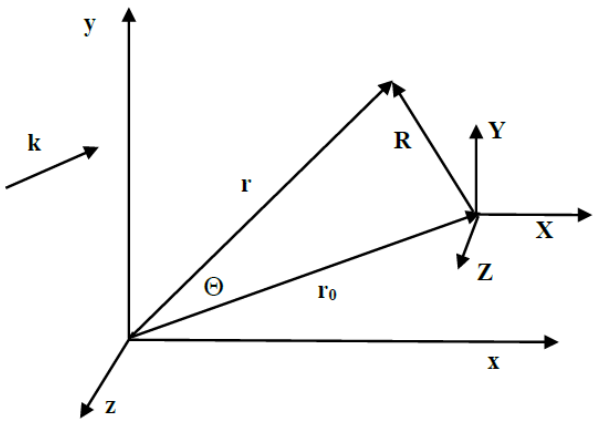

Figure 3.1: The coordinates for translation

The expansion of a plane wave is,

$$e^{ik\cdot r_0} = 4\pi\sum_{v=0}^{\infty}\sum_{\mu=-v}^{v} i^v Y_{v\mu}^*(\hat{\mathbf{k}})u_{v\mu}(\mathbf{r}_0) = 4\pi\sum_{v=0}^{\infty}\sum_{\mu=-v}^{v} i^v Y_{v\mu}^*(\hat{\mathbf{k}})j_v(kr_0)Y_{v\mu}(\hat{\mathbf{r}}) \tag{3.28}$$

When the origin is translated, the expression becomes,

$$u_{nm}^{(1)}(\mathbf{r}) = u_{nm}^{(1)}(\mathbf{r}_0+\mathbf{R}) = \frac{1}{4\pi i^n}\int Y_{nm}(\hat{\mathbf{k}})e^{ik\cdot r_0+ik\cdot \mathrm{R}}d\Omega_k = \int Y_{nm}(\hat{\mathbf{k}})\sum_{v,\mu} i^{v-n}Y_{v\mu}^*(\hat{\mathbf{k}})u_{v\mu}^{(1)}(\mathbf{r}_0)e^{ik\cdot \mathrm{R}}d\Omega_k$$

$$= \sum_{v,\mu} i^{v-n}u_{v\mu}^{(1)}(\mathbf{r}_0)\int Y_{nm}(\hat{\mathbf{k}})Y_{v\mu}^*(\hat{\mathbf{k}})e^{ik\cdot \mathrm{R}}d\Omega_k$$

$$= 4\pi\sum_{v,\mu}\int i^{v-n}Y_{nm}(\hat{\mathbf{k}})Y_{v\mu}^*(\hat{\mathbf{k}})\sum_{t,s} i^t Y_{ts}^*(\hat{\mathbf{k}})d\Omega_k u_{v\mu}^{(1)}(\mathbf{r}_0)u_{ts}(\mathbf{R}) \tag{3.29}$$

$$= 4\pi\sum_{v,\mu} i^{v-n}u_{v\mu}^{(1)}(\mathbf{r}_0)\sum_{t,s} i^t u_{ts}^{(1)}(\mathbf{R})\int Y_{ts}^*(\hat{\mathbf{k}})Y_{nm}(\hat{\mathbf{k}})Y_{v\mu}^*(\hat{\mathbf{k}})d\Omega_k$$

$$= \sum_{v,\mu} A(m,n;-\mu,v;\mathbf{R})u_{v\mu}^{(1)}(\mathbf{r}_0)$$

where

$$A(m,n;-\mu,v;\mathbf{R}) = 4\pi i^{v-n}\sum_{ts} i^t\int Y_{ts}^*(\hat{\mathbf{k}})Y_{nm}(\hat{\mathbf{k}})Y_{v\mu}^*(\hat{\mathbf{k}})d\Omega_k$$

$$= 4\pi i^{v-n}\sum_{p=|v-n|}^{v+n} i^p a_b(m,n;-\mu,v;p)u_{p(m-\mu)}^{(1)}(\mathbf{R})$$

with a_b being the Gaunt's coefficient.

For the Hankel function, the same derivation is used,

$$u_{nm}^{(3)}(\mathbf{r}) = u_{nm}^{(3)}(\mathbf{r}_0+\mathbf{R}) = \sum_{v,\mu} A(\mu,v;m,n;\mathbf{R})u_{v\mu}^{(1)}(\mathbf{r}_0), \qquad R > r_0$$

$$A(m,n;-\mu,v;\mathbf{R}) = 4\pi i^{v-n}\sum_{p=|v-n|}^{v+n} i^p a_b(m,n;\mu,v;p)u_{p(m-\mu)}^{(1)}(\mathbf{R}) \tag{3.30}$$

$$u_{nm}^{(3)}(\mathbf{r}) = u_{nm}^{(3)}(\mathbf{r}_0+\mathbf{R}) = 4\pi i^{v-n}\sum_{v,\mu} i^v\sum_{p} i^p a(\mu,v;m,n;p)u_{p(m-\mu)}^{(1)}(\mathbf{R})u_{v\mu}^{(3)}(\mathbf{r}_0), \qquad R > r_0$$

For the vector wave functions, the above addition theorem can be further extended. The vector wave expansion is

$$\mathbf{X_{nm}}(\hat{\mathbf{k}})\mathbf{e^{ikr}} \;=\; \mathbf{4\pi\pi}_{\mathbf{nm}}(\hat{\mathbf{k}}) \cdot \left(\sum_{\mathbf{v,\mu}} \mathbf{i}^{\mathbf{v}} [\mathbf{X}^{*}_{\mathbf{v\mu}}(\hat{\mathbf{k}})\mathbf{M}^{(1)}_{\mathbf{v\mu}}(\mathbf{r}) \;+\; \mathbf{T}^{*}_{\mathbf{v\mu}}(\hat{\mathbf{k}})\mathbf{N}^{(1)}_{\mathbf{v\mu}}(\mathbf{r})] \right)_{\mathbf{k}} \tag{3.31}$$

The addition theorem for the vector wave functions is

$$\begin{aligned}
&\mathbf{M}^{(1)}_{nm}(\mathbf{r}) = \mathbf{M}^{(1)}_{nm}(\mathbf{r}_0 + \mathbf{R}) = \frac{1}{4\pi i^n}\int \mathbf{X}_{nm}(\hat{\mathbf{k}}) e^{ik\cdot r_0 + ik\cdot \mathrm{R}} d\Omega_k \\
&= \int \mathbf{X}_{nm}(\hat{\mathbf{k}}) \cdot \left(\sum_{v,\mu} i^{v-n} [\mathbf{X}^{*}_{v\mu}(\hat{\mathbf{k}})\mathbf{M}_{v\mu}(\mathbf{r}_0) + \mathbf{T}^{*}_{v\mu}(\hat{\mathbf{k}})\mathbf{N}_{v\mu}(\mathbf{r}_0)] \right) e^{ik\cdot \mathrm{R}} d\Omega_k \\
&= \sum_{v,\mu} i^{v-n} \left(\int \mathbf{X}_{nm}(\hat{\mathbf{k}}) \cdot \mathbf{X}^{*}_{v\mu}(\hat{\mathbf{k}}) e^{i\mathrm{k}\cdot \mathrm{R}} d\Omega_k \mathbf{M}_{v\mu}(\mathbf{r}_0) + \int \mathbf{X}_{nm}(\hat{\mathbf{k}}) \cdot \mathbf{T}^{*}_{v\mu}(\hat{\mathbf{k}}) e^{i\mathrm{k}\cdot \mathrm{R}} d\Omega_k \mathbf{N}_{v\mu}(\mathbf{r}_0) \right) \\
&= \sum_{v,\mu} A^{v\mu}_{nm} \mathbf{M}^{(1)}_{v\mu}(\mathbf{r}_0) + B^{v\mu}_{nm} \mathbf{N}^{(1)}_{v\mu}(\mathbf{r}_0)
\end{aligned} \tag{3.32}$$

with

$$A^{v\mu}_{nm} = i^{v-n} \int \mathbf{X}_{nm}(\hat{\mathbf{k}}) \cdot \mathbf{X}^{*}_{v\mu}(\hat{\mathbf{k}}) e^{i\mathrm{k}\cdot \mathrm{R}} d\Omega_k$$

$$B^{v\mu}_{nm} = i^{v-n} \int \mathbf{X}_{nm}(\hat{\mathbf{k}}) \cdot \mathbf{T}^{*}_{v\mu}(\hat{\mathbf{k}}) e^{i\mathrm{k}\cdot \mathrm{R}} d\Omega_k = i^{v-n} \int i\hat{\mathbf{k}} \times \mathbf{X}_{nm}(\hat{\mathbf{k}}) \cdot \mathbf{X}^{*}_{v\mu}(\hat{\mathbf{k}}) e^{i\mathrm{k}\cdot \mathrm{r}_0} d\Omega_k \tag{3.33}$$

and the explicit form for $A^{v\mu}_{nm}$ and $B^{v\mu}_{nm}$ is

$$\begin{aligned}
A^{v\mu}_{nm}(i,j) &= (-1)^{\mu} i^{v-n} \frac{2v+1}{2v(v+1)} \\
&\times \sum_{p=|n-v|}^{n+v} i^{p} a(m,n;\; -\mu, v; p, p)[n(n+1) + v(v+1) \\
&\quad - p(p+1)] z_p(kr_{i,j}) p_p^{m-\mu}(\cos\theta_{i,j}) e^{i(m-\mu)\varphi_{i,j}}
\end{aligned}$$

$$\begin{aligned}
B^{v\mu}_{nm}(i,j) &= (-1)^{\mu} i^{v-n} \frac{(2v+1)}{2v(v+1)} \sum_{p=|n-v|+1}^{n+v+1} i^{p} [(n+v+1)^2 \\
&\quad - p^2][p^2 - (n-v)^2] a(m,n;\; -\mu, v; p, p-1) z_p \\
&\quad (kr_{i,j}) p_p^{m-\mu}(\cos\theta_{i,j}) e^{i(m-\mu)\varphi_{i,j}}
\end{aligned} \tag{3.34}$$

with

$$a(m, n, \mu, v, p, q) = (-1)^{m+\mu}(2p+1)$$

$$\sqrt{\frac{(n+m)!}{(n-m)!}\frac{(v+\mu)!}{(v-\mu)!}\frac{(p-m-\mu)!}{(p+m+\mu)!}}\begin{pmatrix} n & v & q \\ 0 & 0 & 0 \end{pmatrix}\begin{pmatrix} n & v & p \\ m & \mu & -m-v \end{pmatrix} \tag{3.35}$$

For a multiple solid spheres, the electric and magnetic field can be expanded as follows,

$$\mathbf{E}_i = \sum_{l=1}^{\infty}\sum_{m=-1}^{m=1}(c^i_{lm} j_l(kr)\mathbf{X}_{lm} + d^i_{lm} k^{-1}\nabla\times(j_l(kr)\mathbf{X}_{lm})) = \sum_{l=1}^{\infty}\sum_{m=-1}^{m=1}(c^i_{lm}\mathbf{M}^{(1)}_{lm} + d^i_{lm}\mathbf{N}^{(1)}_{lm})$$

$$\mathbf{E}_s = \sum_{l=1}^{\infty}\sum_{m=-1}^{m=1}(c^s_{lm} h^{(1)}_l(kr)\mathbf{X}_{lm} + d^s_{lm} k^{-1}\nabla\times(h^{(1)}_l(kr)\mathbf{X}_{lm})) = \sum_{l=1}^{\infty}\sum_{m=-1}^{m=1}(c^s_{lm}\mathbf{M}^{(3)}_{lm} + d^s_{lm}\mathbf{N}^{(3)}_{lm})$$

$$\mathbf{E}_1 = \sum_{l=1}^{\infty}\sum_{m=-1}^{m=1}(c^1_{lm} j_l(kr)\mathbf{X}_{lm} + d^1_{lm} k^{-1}\nabla\times(j_l(kr)\mathbf{X}_{lm})) = \sum_{l=1}^{\infty}\sum_{m=-1}^{m=1}(c^1_{lm}\mathbf{M}^{(1)}_{lm} + d^1_{lm}\mathbf{N}^{(1)}_{lm}) \tag{3.36}$$

$$\mathbf{H}_i = -\frac{ik}{\omega\mu}\sum_{l=1}^{\infty}\sum_{m=-1}^{m=1}(c^i_{lm} k^{-1}\nabla\times(j_l(kr)\mathbf{X}_{lm}) + d^i_{lm} j_l(kr)\mathbf{X}_{lm})$$

$$\mathbf{H}_s = -\frac{ik}{\omega\mu}\sum_{l=1}^{\infty}\sum_{m=-1}^{m=1}(c^s_{lm} k^{-1}\nabla\times(h^{(1)}_1(kr)\mathbf{X}_{lm}) + d^s_{lm} h^{(1)}_1(kr)\mathbf{X}_{lm})$$

$$\mathbf{H}_1 = -\frac{ik}{\omega\mu}\sum_{l=1}^{\infty}\sum_{m=-1}^{m=1}(c^1_{lm} k^{-1}\nabla\times(j_l(kr)\mathbf{X}_{lm}) + d^1_{lm} j_l(kr)\mathbf{X}_{lm})$$

By using the above addition theorem, the spherical harmonic expansion of the jth sphere can be related to that of the ith sphere,

$$\begin{aligned}\mathbf{M}^{(3)}_{lm}(j) &= \sum_{s=1}^{\infty}\sum_{t=-s}^{s}\left(A^{lm}_{st}(ji)\mathbf{M}^{(1)}_{st}(i) + B^{lm}_{st}(ji)\mathbf{N}^{(1)}_{st}(i)\right)\\ \mathbf{N}^{(3)}_{lm}(j) &= \sum_{s=1}^{\infty}\sum_{t=-s}^{s}\left(A^{lm}_{st}(ji)\mathbf{N}^{(1)}_{st}(i) + B^{lm}_{st}(ji)\mathbf{M}^{(1)}_{st}(i)\right)\end{aligned} \tag{3.37}$$

The total income field for the *i*th sphere becomes

$$
\begin{aligned}
\mathbf{E}_{ti}(i) &= \mathbf{E}_i(i) + \sum_{\substack{j=1 \\ j\neq i}}^{N} \mathbf{E}_s(j) \\
&= \sum_{l=1}^{\infty}\sum_{m=-1}^{1}\left(c_{lm}^{i,j}\mathbf{M}_{lm}^{(1)}(i) + d_{lm}^{i,j}(ji)\mathbf{N}_{lm}^{(1)}(i)\right) \\
&+ \sum_{l=1}^{\infty}\sum_{m=-1}^{1}\left(\sum_{\substack{j=1 \\ j\neq i}}^{N}\sum_{s=1}^{\infty}\sum_{t=-s}^{s}\left(d_{st}^{s,j}A_{lm}^{st}(ji) + c_{st}^{s,j}B_{lm}^{st}(ji)\right)\mathbf{N}_{lm}^{(1)}(i) + \left(c_{st}^{s,j}A_{lm}^{st}(ji) + d_{st}^{s,j}B_{lm}^{st}(ji)\right)\mathbf{M}_{lm}^{(1)}(i)\right) \\
&= \sum_{l=1}^{\infty}\sum_{m=-1}^{1}\left(\begin{array}{l}\left\{c_{lm}^{i,j} + \sum_{\substack{j=1 \\ j\neq i}}^{N}\sum_{s=1}^{\infty}\sum_{t=-s}^{s}\left(c_{st}^{s,j}A_{lm}^{st}(ji) + d_{st}^{s,j}B_{lm}^{st}(ji)\right)\right\}\mathbf{M}_{lm}^{(1)}(i) \\ + \left\{d_{lm}^{i,j} + \sum_{\substack{j=1 \\ j\neq i}}^{N}\sum_{s=1}^{\infty}\sum_{t=-s}^{s}\left(d_{st}^{s,j}A_{lm}^{st}(ji) + c_{st}^{s,j}B_{lm}^{st}(ji)\right)\right\}\mathbf{N}_{lm}^{(1)}(i)\end{array}\right) \\
&= \sum_{l=1}^{\infty}\sum_{m=-1}^{1}\left((c_{lm}^{i,j} + Q_{lm})\mathbf{M}_{lm}^{(1)}(i) + (d_{lm}^{i,j} + R_{lm})\mathbf{N}_{lm}^{(1)}(i)\right)
\end{aligned}
\tag{3.38}
$$

where

$$
\begin{aligned}
Q_{lm}(i) &= \sum_{\substack{j=1 \\ j\neq i}}^{N}\sum_{s=1}^{\infty}\sum_{t=-s}^{s}\left(c_{st}^{s,j}A_{lm}^{st}(ji) + d_{st}^{s,j}B_{lm}^{st}(ji)\right) \\
R_{lm}(i) &= \sum_{\substack{j=1 \\ j\neq i}}^{N}\sum_{s=1}^{\infty}\sum_{t=-s}^{s}\left(d_{st}^{s,j}A_{lm}^{st}(ji) + c_{st}^{s,j}B_{lm}^{st}(ji)\right)
\end{aligned}
\tag{3.39}
$$

By applying the boundary condition at the sphere surface,

$$
(\mathbf{E}_{ti}(i) + \mathbf{E}_s(i) - \mathbf{E}_1(i)) \times \mathbf{e}_r = 0, \qquad (\mathbf{H}_{ti}(i) + \mathbf{H}_s(i) - \mathbf{H}_1(i)) \times \mathbf{e}_r = 0 \tag{3.40}
$$

a system of four equations is obtained,

$$
\begin{aligned}
c_{l,\pm1}^{s,i}\xi_l(x)m + (c_{l,\pm1}^{i,j} + Q_{lm})\psi_l(x)m &= c_{l,\pm1}^{c,i}\psi_l(mx) \\
d_{l,\pm1}^{s,i}\xi_l'(x)m + (d_{l,\pm1}^{i,j} + R_{lm})\psi_l'(x)m &= d_{l,\pm1}^{c,i}\psi_l'(mx) \\
c_{l,\pm1}^{s,i}\xi_l'(x) + (c_{l,\pm1}^{i,j} + Q_{lm})\psi_l'(x) &= c_{l,\pm1}^{c,i}\psi_l'(mx) \\
d_{l,\pm1}^{s,i}\xi_l(x) + (d_{l,\pm1}^{i,j} + R_{lm})\psi_l(x) &= d_{l,\pm1}^{c,i}\psi_l(mx)
\end{aligned}
\tag{3.41}
$$

The coefficients can be obtained by solving the above system of equations,

$$c_{l,\pm1}^{c,i} = (c_{l,\pm1}^{i,j} + Q_{l,\pm1}) \frac{m\psi_l(x)\xi_l'(x) - m\psi_l'(x)\xi_l(x)}{\psi_l(mx)\xi_l'(x) - m\psi_l'(mx)\xi_l(x)}$$
$$d_{l,\pm1}^{c,i} = (d_{l,\pm1}^{i,j} + R_{l,\pm1}) \frac{m\psi_l(x)\xi_l'(x) - m\psi_l'(x)\xi_l(x)}{m\psi_l(mx)\xi_l'(x) - \psi_l'(mx)\xi_l(x)}$$

$$c_{l,\pm1}^{s,i} = -(c_{l,\pm1}^{i,j} + Q_{l,\pm1}) \frac{\psi_l(mx)\psi_l'(x) - m\psi_l'(mx)\psi_l(x)}{\psi_l(mx)\xi_l'(x) - m\psi_l'(mx)\xi_l(x)}$$
$$d_{l,\pm1}^{s,i} = -(d_{l,\pm1}^{i,j} + R_{l,\pm1}) \frac{m\psi_l(mx)\psi_l'(x) - \psi_l'(mx)\psi_l(x)}{m\psi_l(mx)\xi_l'(x) - \psi_l'(mx)\xi_l(x)} \tag{3.42}$$

Following the procedure given before, the total scattering cross section is calculated as

$$C_{sca} = \frac{W_{sca}}{I_{inc}} = \frac{1}{k^2 E_0^2} \sum_{l=1}^{\infty} \sum_{m=-1}^{m=1} \left(c_{lm}^{*s,T} c_{lm}^{s,T} + d_{lm}^{*s,T} c_{lm}^{s,T} \right) \tag{3.43}$$

where

$$c_{mn}^{s,T} = c_{mn}^{s,1} + Q_{mn}(1); \qquad d_{mn}^{s,T} = d_{mn}^{s,1} + R_{mn}(1)$$
$$Q_{mn}(i) = \sum_{\substack{j=1 \\ j\neq i}}^{N} \sum_{l=1}^{\infty} \sum_{k=-1}^{l} \left(c_{kl}^{s,j} A_{mn}^{kl}(ji) + d_{kl}^{s,j} B_{mn}^{kl}(ji) \right) = \sum_{\substack{j=1 \\ j\neq i}}^{N} \sum_{l=1}^{\infty} \sum_{k=-1,1} \left(c_{kl}^{s,j} A_{mn}^{kl}(ji) + d_{kl}^{s,j} B_{mn}^{kl}(ji) \right)$$
$$R_{mn}(i) = \sum_{\substack{j=1 \\ j\neq i}}^{N} \sum_{l=1}^{\infty} \sum_{k=-1}^{l} \left(d_{kl}^{s,j} A_{mn}^{kl}(ji) + c_{kl}^{s,j} B_{mn}^{kl}(ji) \right) = \sum_{\substack{j=1 \\ j\neq i}}^{N} \sum_{l=1}^{\infty} \sum_{k=-1,1} \left(d_{kl}^{s,j} A_{mn}^{kl}(ji) + c_{kl}^{s,j} B_{mn}^{kl}(ji) \right) \tag{3.44}$$
$$A_{mn}^{kl}(j1) = A_{kl,mn} = A_{l'm',lm} = \alpha_{mn}^{\mu\nu}; \qquad B_{mn}^{kl}(j1) = B_{kl,mn} = B_{l'm',lm} = \alpha_{mn}^{\mu\nu}$$

3.1.5 Light Scattering by Multilayered Multiparticles

With the procedures of the calculation of the scattering by a single multilayered spherical structure and that of the scattering by multiple solid sphere being given, the procedures for calculating the scattering by multiple multilayered particles are as follows.

Firstly, calculate the scattering coefficients (a_n and b_n) for each isolated multilayered particle as stated above, where a_n and b_n are the same as c_{lm}^{s} and d_{lm}^{s} given before, respectively.

Then, by using the addition theorem, translate all the income waves for *i*th particle, which are from the scattered field from other particles, to the origin of *i*th particle. Calculate the coefficients for *i*th particle and repeat the procedure for each other particles.

In addition, choose one particle as reference and translate all other particles to the center of the reference particle. Integrate the Poyting vector over a surface, which is large enough to include all the particles, to get the total scattered energy. Then, the total scattering efficiency is obtained through dividing by the incident irradiance,

$$Q_{\text{sca}} = \frac{2}{k^2 R^2} \sum_{n=1}^{\infty} (2n+1)(|a_n|^2 + |b_n|^2) \tag{3.45}$$

where k is the wave number, R is the radius of the nanosphere, n is the order of electric and magnetic multipole. an and bn are the effective electric and magnetic multipole scattering coefficients.

3.1.6 Condition for Maximized Forward Scattering

Based on the analytical solutions for the scattering, the far field scattering intensity is obtained. To begin with, the physical description of induced electric dipole and magnetic dipole inside the nanoparticle will be illustrated. Then, the condition for maximized forward scattering with backward scattering, which is proved as the first Kerker's condition [62], is briefly stated.

The light is assumed to propagate along the z-direction and be polarized in the x-direction. For metal particle, such as Ag sphere, the free electrons of the conduction band inside the nanoparticle will oscillate back and forth in accordance with the electromagnetic wave. For a certain wavelength, the magnitude of the oscillation is maximized, which corresponds to Surface Plasmon Resonance (SPR). The movement of the free electrons will contribute to an induced electric field. The magnitude of the induced electric field varies along the positive and negative direction of the x-axis, which leads to an electric dipole.

For a dielectric sphere, the electrons are bound inside the molecule. When light is applied, the displacement currents are formed by the movement of the bound electrons, which generates the electric dipole along the x-direction. The intensity of the induced electric dipole in the dielectric sphere is usually smaller than that in the pure metal, due to the electrons are bound inside the molecule rather than those are free in the metal.

The oscillation of the magnetic field of the incident light is along the positive and negative direction of the y-axis. For a dielectric sphere, the circulation displacement currents are introduced since the electrons execute a circular orbit in the plane perpendicular to the direction of the magnetic field. The magnetic dipole is further generated by the circulation displacement currents.

From Pointing's theorem, the energy flow in the scattered wave is [63]

$$S = \frac{1}{2}(E_\theta H_\phi^* - E_\phi H_\theta^*) \tag{3.46}$$

where $E_\theta, E_\phi, H_\theta, H_\phi$ are the transverse components with the expressions as

$$\begin{aligned} E_\phi &= \frac{H_\theta}{(m_2)} = -\frac{i\exp(-ik_2 r)}{k_2 r}\sin\phi \sum_{n=1}^{\infty}\frac{2n+1}{n(n+1)} \\ &\quad \times\left\{ a_n \frac{P_n^{(1)}(\cos\theta)}{\sin\theta} + b_n \frac{dP_n^{(1)}(\cos\theta)}{d\theta} \right\} \\ E_\theta &= -\frac{H_\phi}{(m_2)} = \frac{i\exp(-ik_2 r)}{k_2 r}\cos\phi \sum_{n=1}^{\infty}\frac{2n+1}{n(n+1)} \\ &\quad \times\left\{ a_n \frac{dP_n^{(1)}(\cos\theta)}{d\theta} + b_n \frac{P_n^{(1)}(\cos\theta)}{\sin\theta} \right\} \end{aligned} \tag{3.47}$$

where a_n and b_n represent the electric and magnetic multipoles. Since the contribution of the scattering from the higher orders are much less than that from the electric and magnetic dipole, only a_1 and b_1 are considered in this work.

Then, the normalized intensity of the scattered radiation in the far-field is expressed as

$$NSI(\theta,\varphi)=\frac{9}{4k^2}[\sin^2\varphi(a_1+b_1\cos\theta)^2+\cos^2\phi(a_1\cos\theta+b_1)]^2 \tag{3.48}$$

The scattering intensity in the forward direction is further obtained when θ=0°,

$$NSI(0,\varphi)=\frac{9}{4k^2}(a_1+b_1)^2 \tag{3.49}$$

while that in the backward direction is

$$NSI(180,\varphi)=\frac{9}{4k^2}(a_1-b_1)^2 \tag{3.50}$$

It can be shown that the forward to backward scattering ratio is maximized when a_1 is equal to b_1.

3.2 Numerical Simulation

3.2.1 Introduction to the Finite-Difference Time-Domain (FDTD) Method

The Finite-Difference Time-Domain (FDTD) method solves Maxwell's curl equations based on Yee Algorithm [64].

$$\frac{\partial\mathbf{D}}{\partial t}=\nabla\times\mathbf{H} \qquad \frac{\partial\mathbf{H}}{\partial t}=-\frac{1}{\mu_0}\nabla\times\mathbf{E}$$

$$\mathbf{D}(\omega)=-\varepsilon_0\varepsilon_r(\omega)\mathbf{E}(\omega) \tag{3.51}$$

where **H** is the magnetic field, **E** the electric field, **D** the displacement field, ω the frequency, and $\varepsilon_r(\omega)$ is the complex relative dielectric constant. The detailed procedures can be summarized follows:

1. Express all the derivatives appears in Maxwell's equations with finite differences.
2. By applying the boundary conditions, solve the resulting system equation to obtain the updated equation, where all the fields in next time step is expressed in terms of the fields in current time step.
3. Solve the electric and magnetic fields consequently with each time step.
4. Repeat the previous step until all the electric and magnetic fields are achieved through the simulation time domain.

With the electric and magnetic fields obtained, the light transmission, i.e., the total power passes a certain plane, can be calculated as

$$T(\lambda) = \frac{1}{2}\frac{\int \mathrm{Re}(\mathbf{P}(\lambda)^{\mathrm{Monitor}})\cdot dS}{\text{Source Power}} \tag{3.52}$$

where $T(\lambda)$ is the normalized transmission, while **P** is the Poynting vector. For the light scattering by nanoparticles, a box monitor, which consists of 6 plane monitors, is applied to measure the power flowing in and out of the sphere. As a result, the energy absorbed and scattered by the nanoparticle is obtained. Furthermore, the light absorption and scattering efficiency can be calculated through dividing the power by the source intensity and the particle area.

3.2.2 Validation of FDTD Accuracy

In this work, the numerical simulation is conducted by Lumerical FDTD package. To validate the accuracy of the numerical method, the light absorption and scattering efficiency of a nanosphere is investigated with both analytical solution and numerical method. The radius of the sphere is 50 nm and the refractive index equals to 5+0.4i. The mesh size for the numerical method is set to 1 nm. The scattering and absorption efficiency versus the size parameter for both methods are shown in Figure 3.2 and Figure 3.3, respectively.

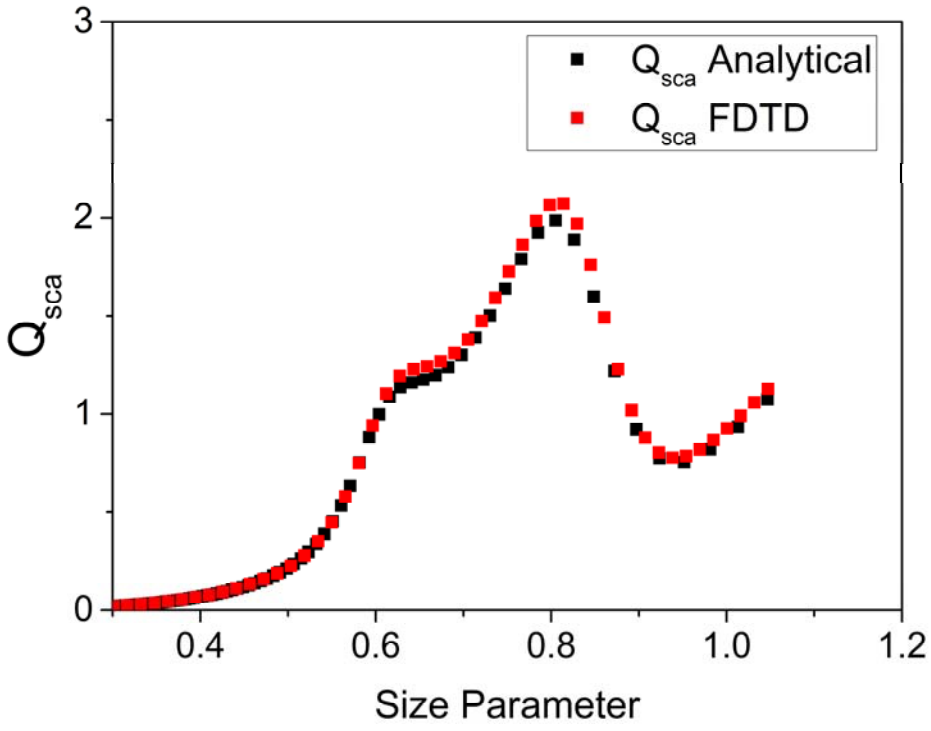

Figure 3.2: Light scattering efficiency of nanosphere calculated by both analytical and numerical methods.

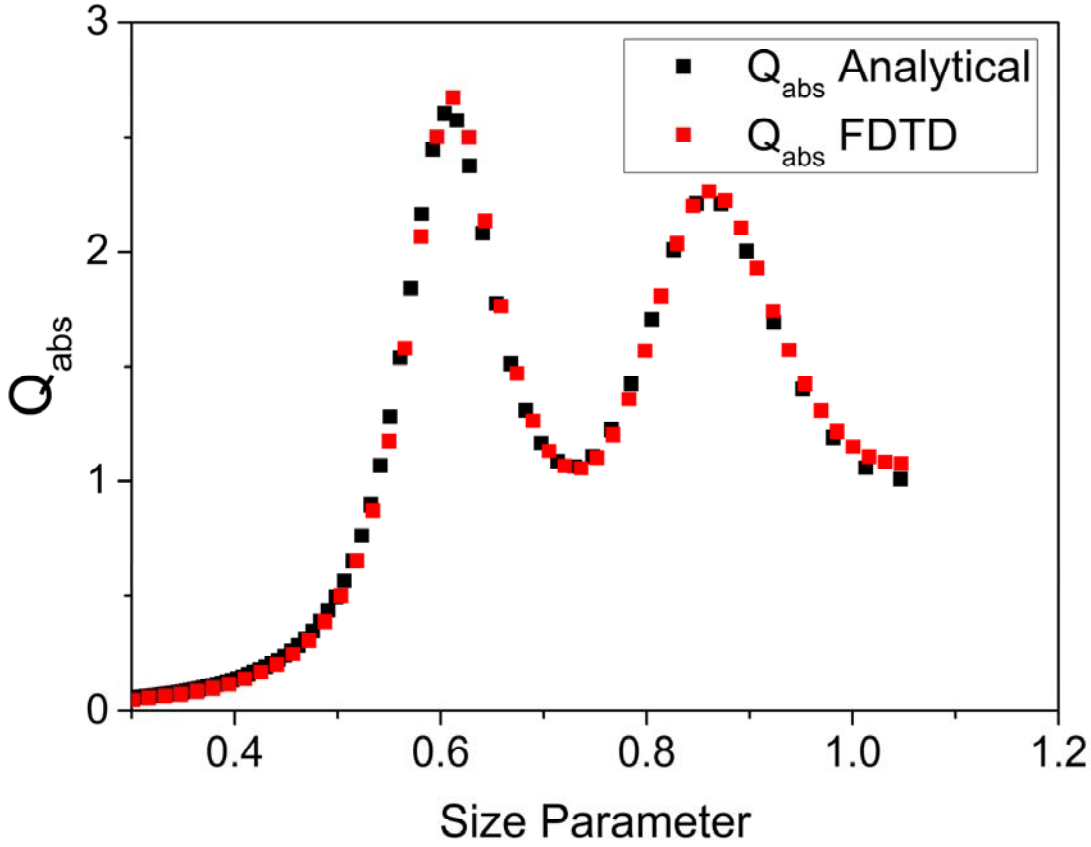

Figure 3.3: Light absorption efficiency of nanosphere calculated by both analytical and numerical methods.

It can be seen that the results from the numerical method fit well with the analytical solution. Moreover, the maximum difference between the numerical and analytical results are plotted versus the mesh size as shown in Figure 3.4. By reducing the mesh size, the numerical result approaches closer to the analytical one. However, the simulation time is also increased dramatically. Thus, the accuracy and appropriate mesh size, which is related to the particle size and refractive index, are determined and utilized in the simulations throughout this work.

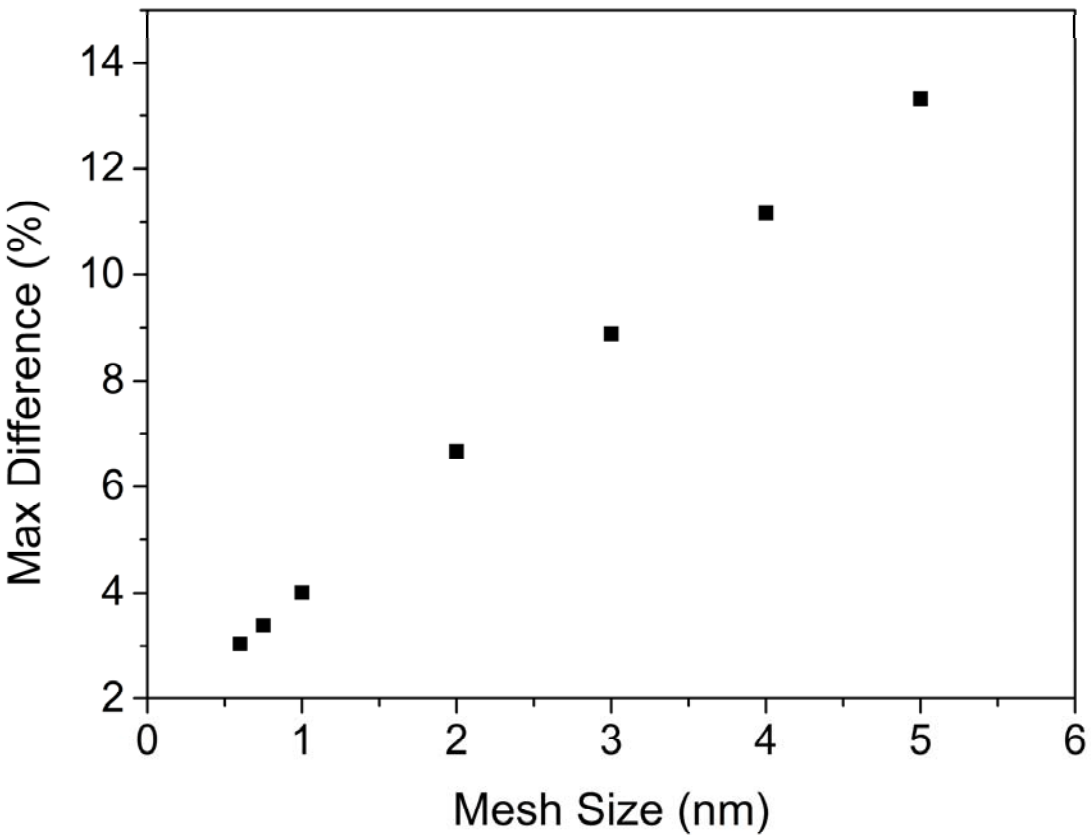

Figure 3.4: Maximum difference between numerical and analytical solution versus mesh size.

CHAPTER 4

Forward Light Scattering Nanoparticles for Silicon Solar Cell

4.1 Introduction

In this chapter, we present a lossless, strong forward-scattering nanostructure for high-performance light trapping over the solar spectrum. This solar harvesting configuration consists of forward-scattering nanoparticle arrays largely embraced in an appropriate medium and partially embedded in a silicon thin film. Nanoparticles or nanoparticle clusters processing better forward-scattering than other reported structures over a wide wavelength range were obtained by tuning their magnetic and electric responses via the change of either structural configurations or surrounding media or both. Results show that loseless TiO_2 nanoparticles embraced in a glass medium scatter light in forward direction and with partial embedding greatly increase the light trapping in a silicon substrate of varying thicknesses. In particular, the nanostructure, consisting of 500 nm TiO_2 nanoparticles embedded 90 nm into a 200 nm thin film silicon cell, yields an increment of 10.3 mA/cm^2 in short-circuit current density over the bare thin film silicon cell or absorbs 3.15 times as much light as the bare one.

4.2 Results and Discussion

Prior to employing the nanoparticles to thin film solar cells, the physical phenomena inside a nanoparticle under light illumination is considered. For a metal particle, such as an Ag nanosphere, the free electrons oscillate back and forth in response to the incident electromagnetic wave. At a certain wavelength, the magnitude of the oscillation is maximized, which corresponds to the localized Surface Plasmon Resonance (SPR). The collective oscillating free electrons act as an

oscillating electric dipole to produce an induced electric field. For a dielectric sphere, the electrons are bound inside the molecule. When light is applied, the displacement currents are formed by the movement of the bound electrons, which generates the electric dipole along the electric field direction of the incident light. The intensity of the induced electric dipole in the dielectric sphere is usually smaller than that in pure metals, since the electrons are bounded in dielectrics and are free in metals. For a dielectric sphere, the circulation displacement currents also occur since the electrons execute a circular orbit in a plane perpendicular to the direction of the magnetic field in response to the action of the magnetic field. These circulation displacement currents produce the effect of a magnetic dipole.

Figure 4.1 plots the scattering spectra of individual nanoparticle of different materials, e.g., Ag nanosphere and Si nanosphere, both of 80 nm in radius. In Figures 4.1(a) and (b) are shown the spectral responses of the total scattering efficiency and of the electric and magnetic dipoles denoted by a_1 and b_1, respectively. The results for electric and magnetic quadrupoles (a_2 and b_2) are also included for the purpose of comparison. The scattering patterns of all the resonance peaks, i.e., electric dipole of Ag nanosphere, electric dipole of Si nanosphere and magnetic dipole of Si nanosphere are plotted in Figures 4.1(c)-(e). Clearly, the resonance peak of Ag nanosphere is dominated by the electric dipole component (see Figure (a)), that is, the light is scattered evenly in both forward and backward directions, as displayed in Figure 4.1(c). Figure 2(b) illustrates that the Si nanosphere possesses both electric and magnetic dipoles. The scattering patterns at the peak wavelength of the electric and magnetic dipoles are displayed in Figure 4.1(d,e), which demonstrates that the individual dipole spreads the light equally in both forward and backward directions.

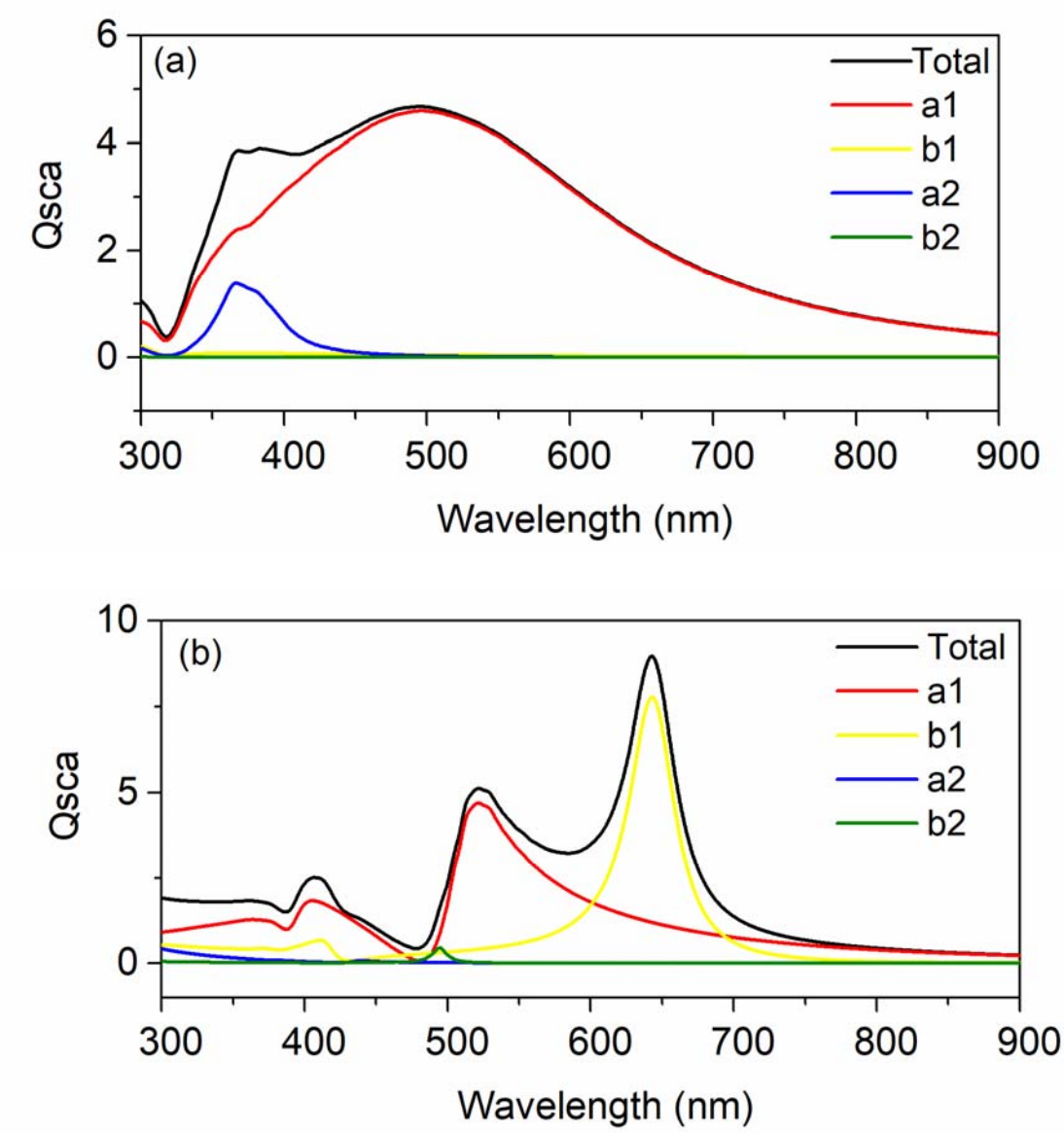
(a)
Total
a1
b1
a2
b2
Qsca
Wavelength (nm)
(b)
Total
a1
b1
a2
b2
Qsca
Wavelength (nm)

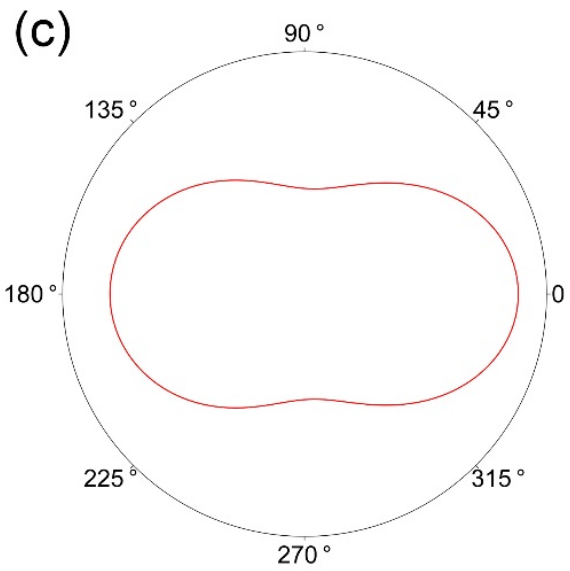
(c)
90 °
135 °
45 °
180 °
0
225 °
315 °
270 °

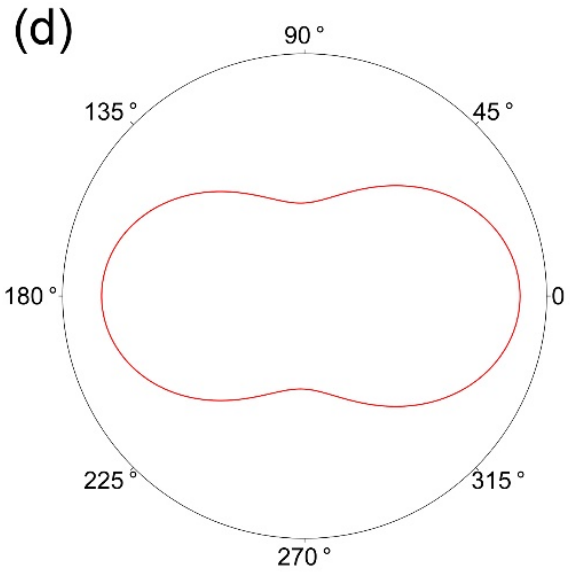
(d)
90 °
135 °
45 °
180 °
0
225 °
315 °
270 °

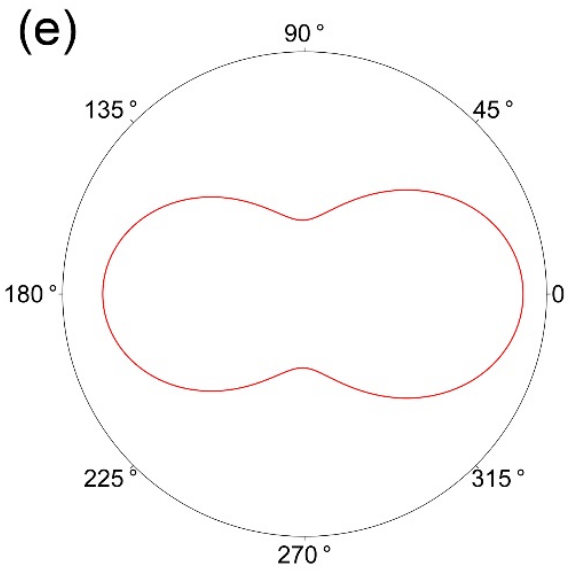

Figure 4.1: Total scattering efficiency with multiple contributions of (a) Ag nanosphere and (b) Si nanosphere. (c) The scattering pattern of Ag nanosphere at 500 nm. (d) (e) The Scattering pattern of Si nanosphere at 520 nm and 635 nm.

To achieve the first Kerker's condition, which requires the overlapping of the electric and magnetic dipoles, the metal-dielectric core/shell nanostructure is utilized. The resonance position of each mode can be tuned by varying the radii of spherical layers. The designed Si/Ag/Si three layered rattling structure is shown in Figure 4.2(a), where the radius of the inner Si core, Ag shell and outer Si shell is 50nm, 60nm and 80nm, respectively. The forward and backward scattering efficiencies of the Si/Ag/Si three layered structure is shown in Figure 4.2(b). Examination of the results indicates that the scattered light is mainly in the forward direction at the resonance peak. The total scattering efficiency and the contributions from each mode are shown in Figure 4.2(c). The electric dipole term equals to the magnetic counterpart at the wavelength of around 550nm, satisfying the first Kerker's condition. The scattering pattern in Figure 4.2(d) confirms that the three-layered structure scatters the incident light dominantly in the forward direction at its peak frequency.

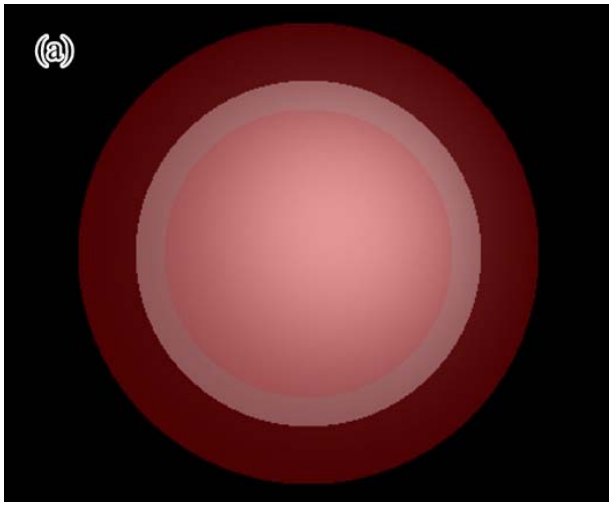
(a)

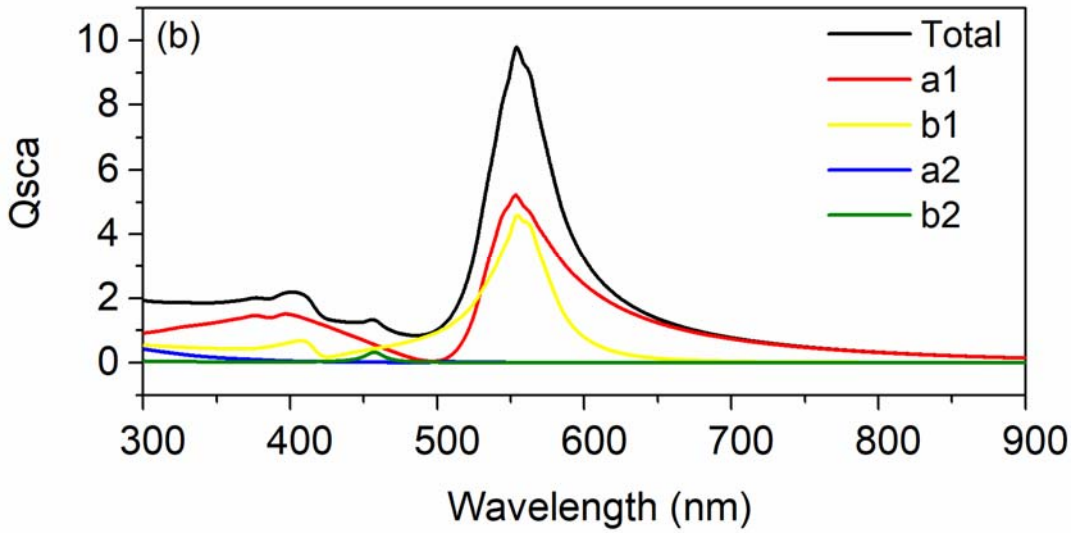
(b)
Total
a1
b1
a2
b2
Qsca
Wavelength (nm)
0
2
4
6
8
10
300
400
500
600
700
800
900

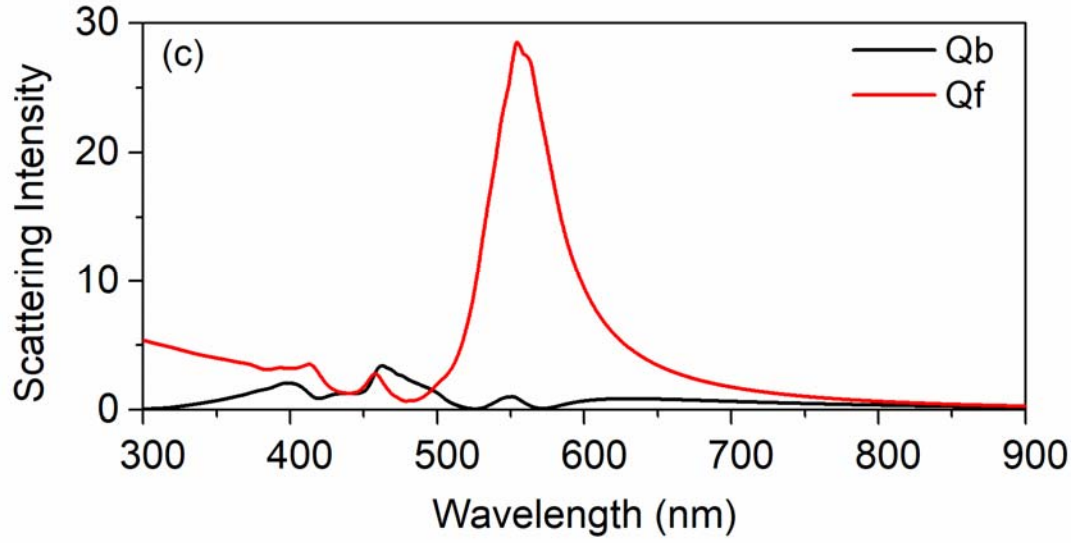
(c)
Qb
Qf
Scattering Intensity
Wavelength (nm)
0
10
20
30
300
400
500
600
700
800
900

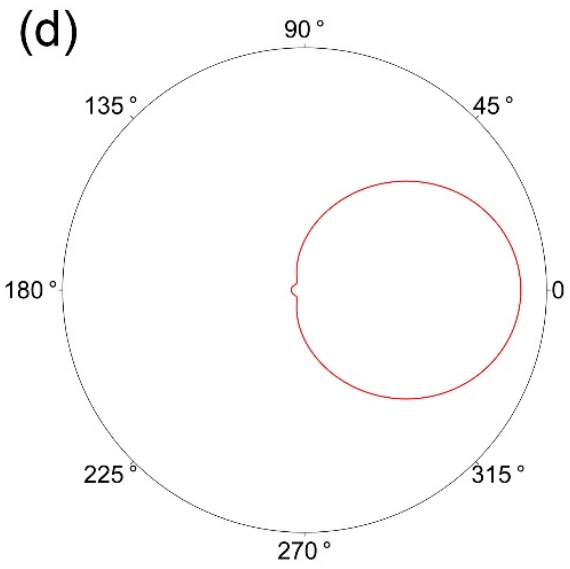

Figure 4.2: (a) The designed structure. (b) Total scattering efficiency with multiple contributions of the 50nm-60nm-80nm Si/Ag/Si three layered rattling structure. (c) The forward and backward scattering efficiency. (d) The Scattering pattern of Si/Ag/Si structure.

The above structure can lead to an extremely high scattering efficiency peak at the resonance frequency. However, for applications in solar cells, a broadband enhancement is preferred, which means the Kerker's condition needs to be satisfied over the effective solar spectrum. To investigate the influence of the refractive index on the scattering behavior, the forward and the backward scattering efficiencies for a r=150 nm nanoparticle with different *n* values (real part), i.e., 1.5, 2, 2.5, 3, 3.5 and 4 are calculated and the results are shown in Figure 4.3 (a) - (f). It is apparent that the maximum forward to backward scattering ratio is obtained if the refractive index ratio of the nanosphere over the medium is approximately at 2. The reason can be explained by analyzing the total scattering with each components plotted in Figure 4.4 (a) - (f). When the n value is relatively small, as shown in Figure 4.4 (a), the peak wavelengths of the electric and magnetic dipoles are roughly the same. As n increases in value, the peak wavelengths of both electric and magnetic dipoles shift to the right. Moreover, the peak of magnetic dipole moves more significantly than that of the electric dipole. The parameter n, in physics, represents

the ability of the molecule to attract the electrons around it, which is similar to the spring mass model. When n is small, the electrons inside each molecule are relatively “free”. As a consequence, the vibration of the electrons either in the electric dipole mode, where the electrons oscillate back and forth, or in the magnetic dipole mode, where the elections circulating in the peripheral direction are not affected much by the attraction force from the molecules. However, as n increases, the attraction becomes stronger. Thus, the electrons are “slowed down” for both modes, which leads to the lower peak frequency. Moreover, the circular path of electrons in the magnetic dipole mode is several times longer than that in the electric dipole mode, which results in the shifting of peak wavelength in magnetic dipole mode being more pronounced. This explains why these two dipole modes are separated in the spectrum plots above.

From the results above, it is also evident that a higher n value leads to a larger scattering efficiency. This may attributed to the fact that the refractive index is also interpreted as the ability to focus the light. In other words, a larger n value allows more incident energy to be focused, which contributes to a stronger scattered light.

To sum up above discussion, a rule to design the nanoparticle for broadband forward scattering is to select the material with a relatively high refractive index compared to that of the surrounding medium. In the meantime, the peaks of the electric and magnetic dipole modes are not separated much to lose the forward scattering behavior. Our further analysis, taken the above into consideration, shows that an optimal refractive index ratio of the nanosphere over the medium for broadband enhancement is about 2.

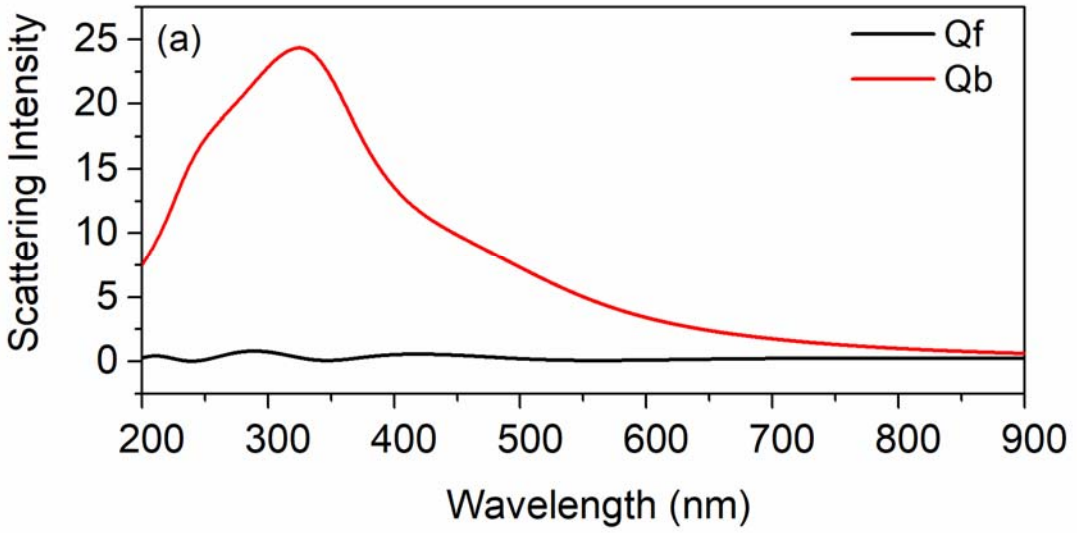
(a)
Qf
Qb
Scattering Intensity
0
5
10
15
20
25
200
300
400
500
600
700
800
900
Wavelength (nm)

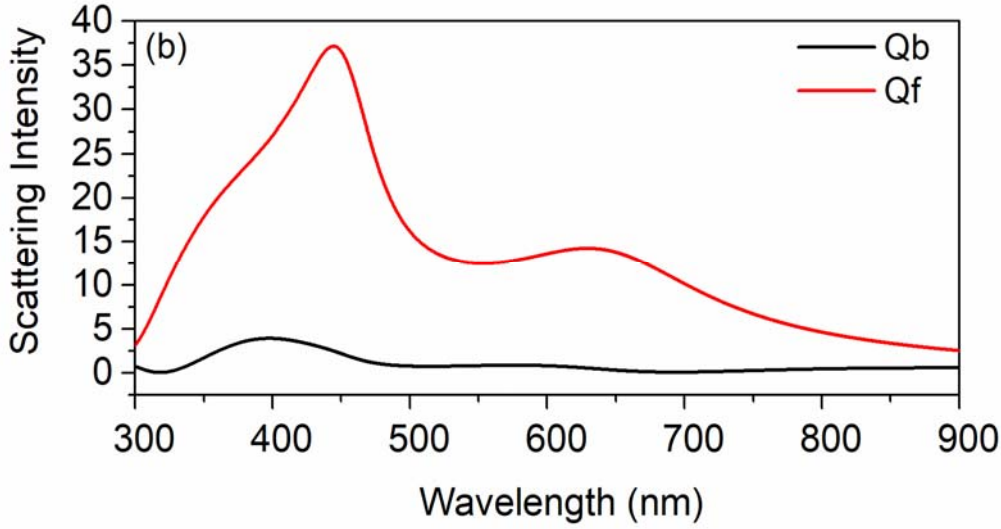
(b)
Qb
Qf
Scattering Intensity
0
5
10
15
20
25
30
35
40
300
400
500
600
700
800
900
Wavelength (nm)

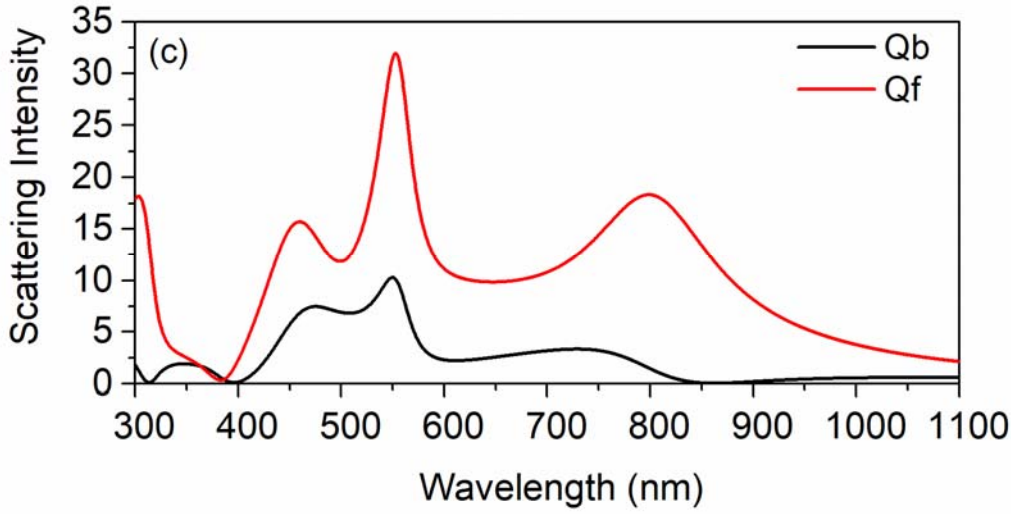
(c)
Qb
Qf
Scattering Intensity
0
5
10
15
20
25
30
35
300
400
500
600
700
800
900
1000
1100
Wavelength (nm)

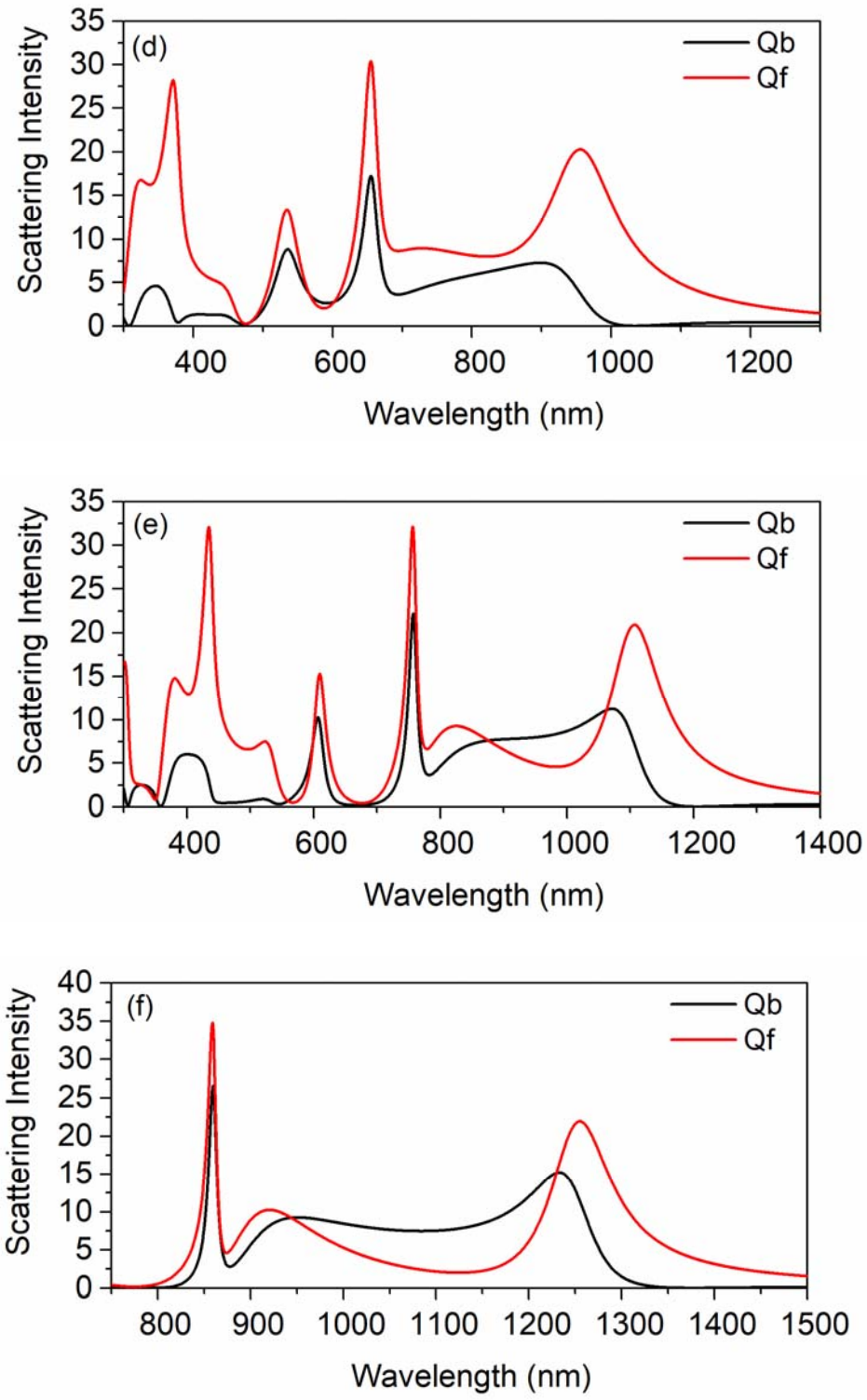

Figure 4.3: Forward and backward scattering efficiencies for nanoparticles with different n values (a) n=1.5, (b) n=2, (c) n=2.5, (d) n=3, (e) n=3.5, (f) n= 4

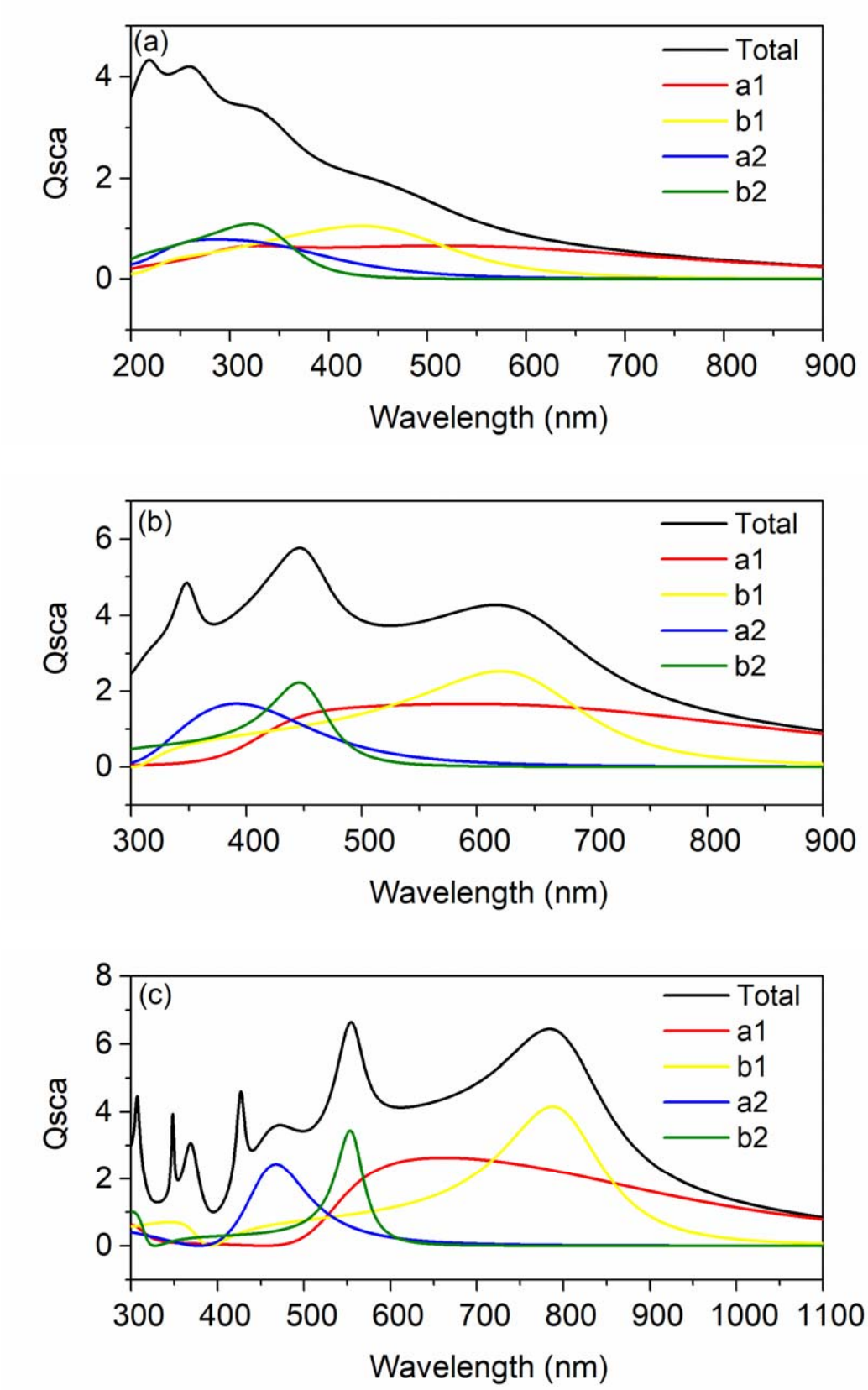
(a)
Total
a1
b1
a2
b2
Qsca
Wavelength (nm)
(b)
Total
a1
b1
a2
b2
Qsca
Wavelength (nm)
(c)
Total
a1
b1
a2
b2
Qsca
Wavelength (nm)

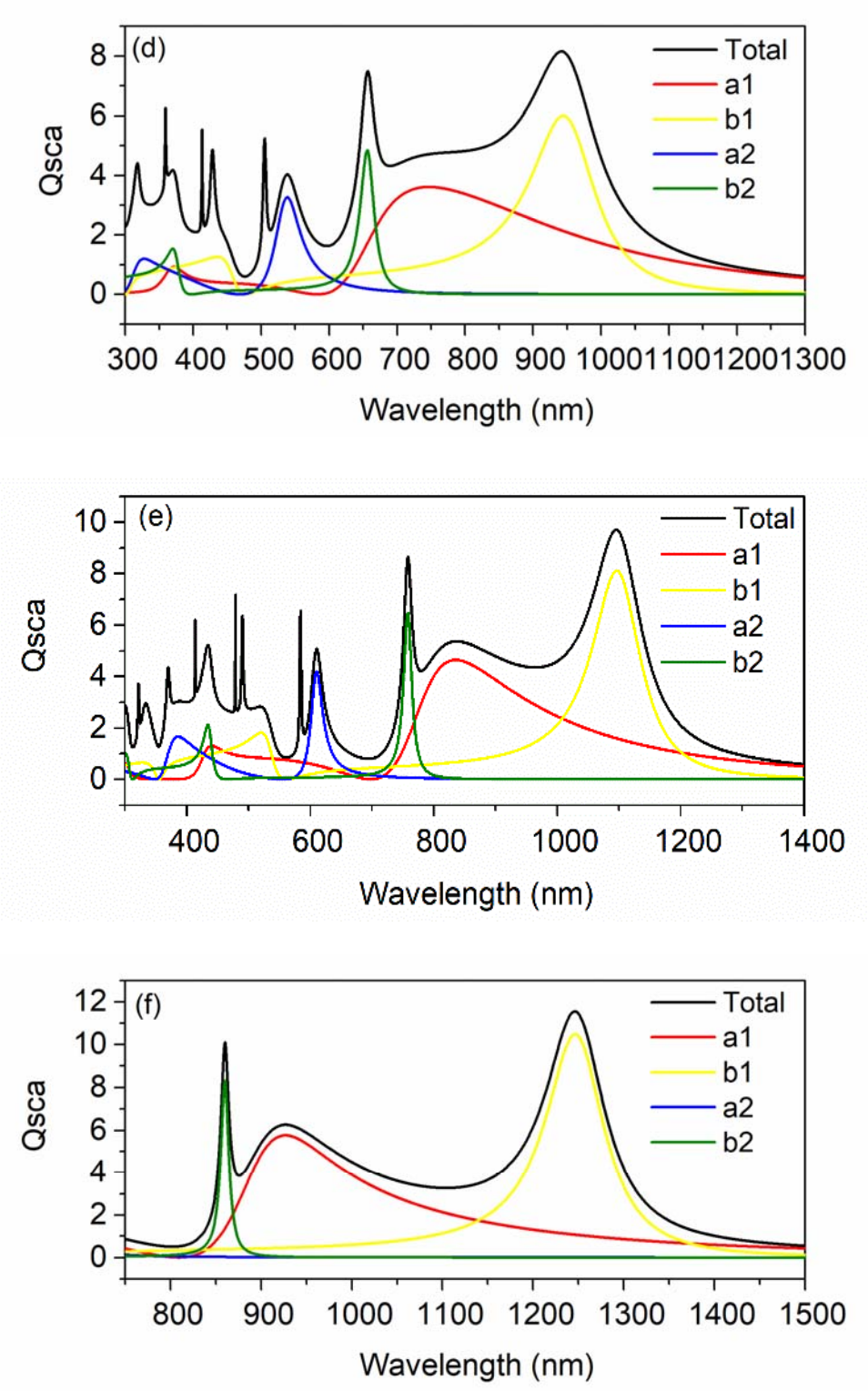

Figure 4.4: Total scattering efficiency with multiple contributions of nanoparticles with different n values (a) n=1.5, (b) n=2, (c) n=2.5, (d) n=3, (e) n=3.5, (f) n= 4

Figure 4.5 plots the forward and backward scattering efficiencies and the scattering pattern at the peak wavelength with different refractive indexes of the materials, i.e., ITO in air, TiO_2 in glass medium and Si in ITO. For the case that ITO (refractive index around 2) nanosphere inside the air medium, as shown in Figures 4.5 (a) and (b), scattering efficiency is relatively lower. However, the forward scattering is much broadened, suggesting that the overall scattering efficiency within the effective solar spectrum is enhanced. Similar results are found for Si (n nearly equals to 4) inside the ITO and TiO2 (around 2.8) in glass (around 1.4), which are shown in Figure 6 (c)-(f). Moreover, further simulations reveal that the larger the refractive index of the nanosphere, the higher the forward scattering efficiency is. The reason is that as the *n* increases, more light around the incident direction is focused, which contributes to enhanced light scattering. The results above confirm the crucial conclusion stated in the last section. Specifically, for the solar absorption application, the refractive index of a nanoparticle should be as high as possible while the ratio of the refractive indexes of the nanosphere and its surrounding medium is kept approximately at 2.

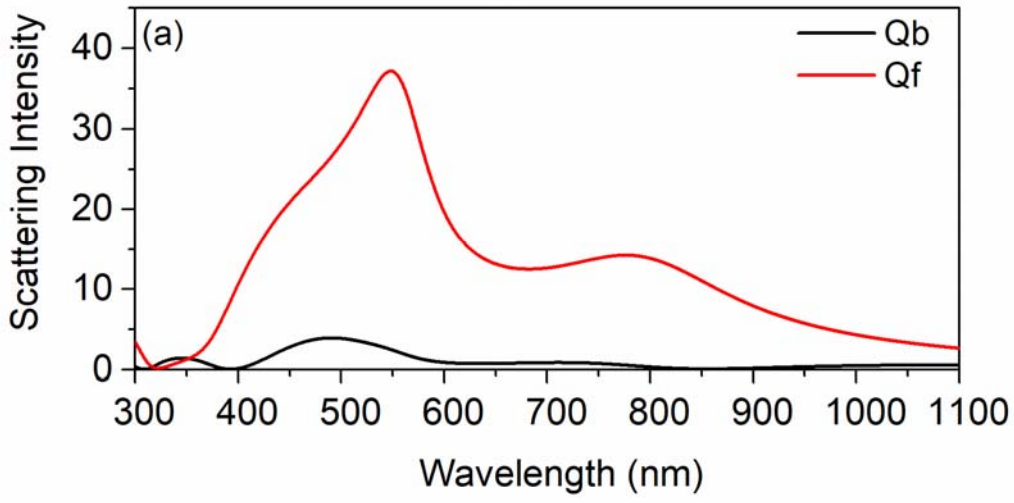

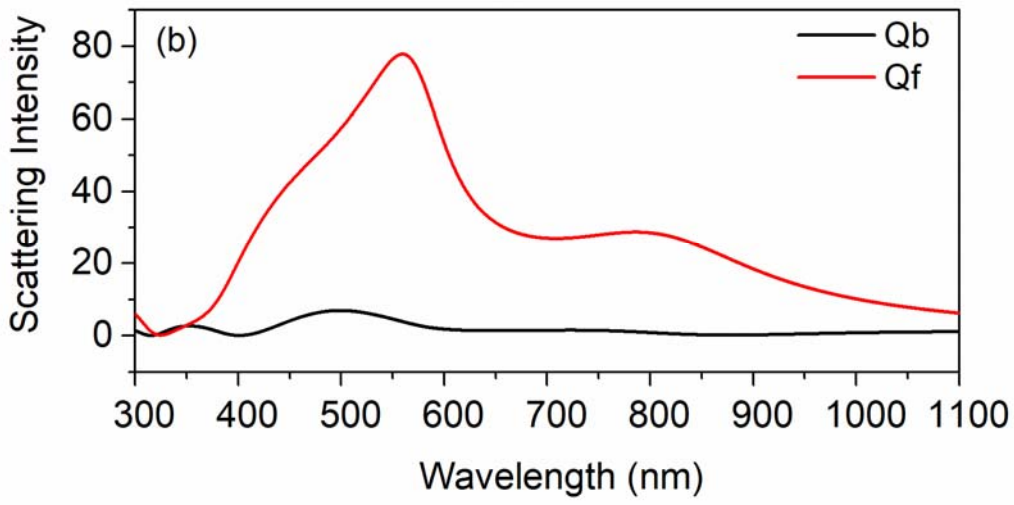
(b)
Qb
Qf
Scattering Intensity
0
20
40
60
80
300
400
500
600
700
800
900
1000
1100
Wavelength (nm)

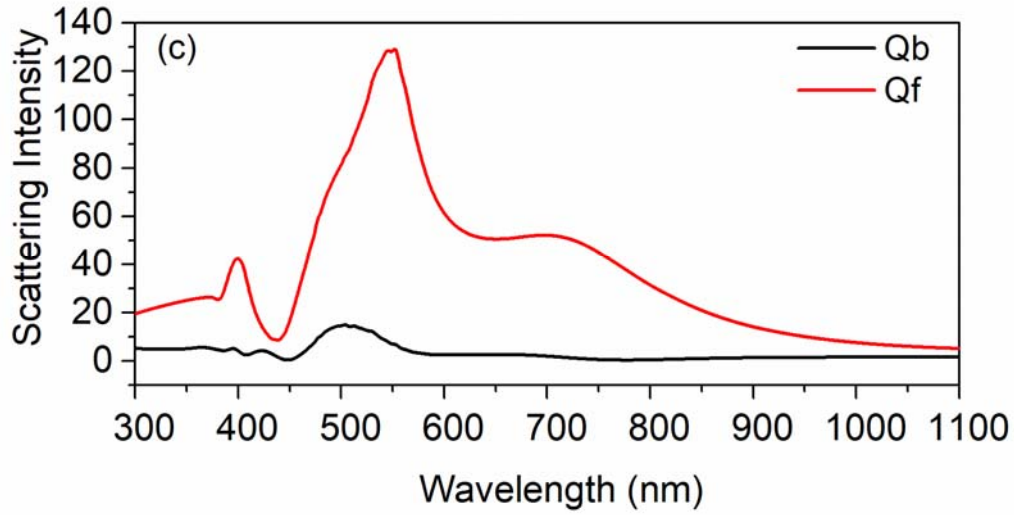
(c)
Qb
Qf
Scattering Intensity
0
20
40
60
80
100
120
140
300
400
500
600
700
800
900
1000
1100
Wavelength (nm)

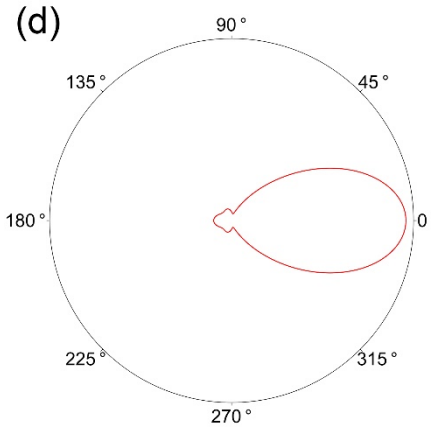
(d)
90 °
135 °
45 °
180 °
0
225 °
315 °
270 °

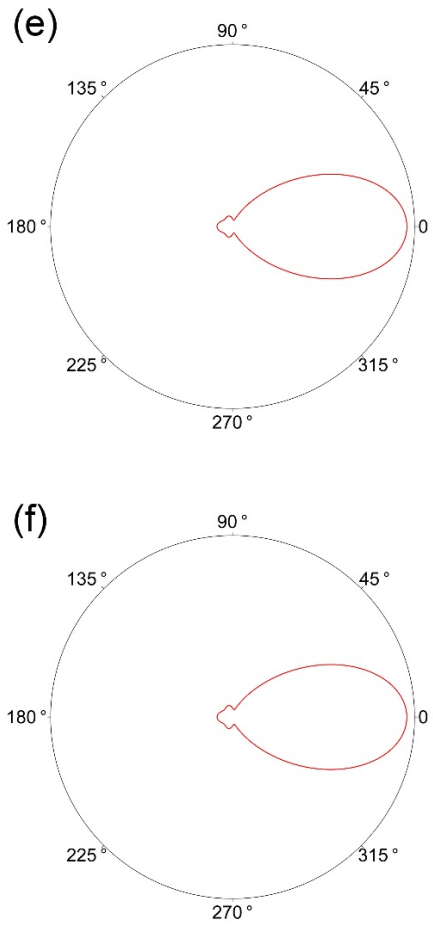

Figure 4.5: Forward and backward scattering efficiencies with different particle and medium combinations (a) ITO (r=185nm) in air, (b) TiO_2 (r=135nm) in glass and (c) Si (r=90nm) in ITO. The scattering pattern at the peak wavelength for each case (d) ITO in air at 550nm, (e) TiO_2 (r=135nm) in glass at 550nm and (f) Si (r=90nm) in ITO at 550nm.

One question may be raised consequently of whether the above design principle still holds for the case of the nanoparticle aggregates. To address this issue, two TiO_2 nanospheres aligned along the electric and the magmatic field axis of the incident light are investigated. The radius of each TiO_2 nanosphere is 135nm, and the two particles are direct contact, with the surrounding medium being glass. The forward and the backward scattering efficiencies for these cases are shown in Figures 4.6 (a) and (b). It is apparent that the forward scattering behavior is not changed much insomuch as that each particle scatters the light forwardly in a relatively narrow angle. Specifically, the interference from the adjacent nanoparticle is insignificant.

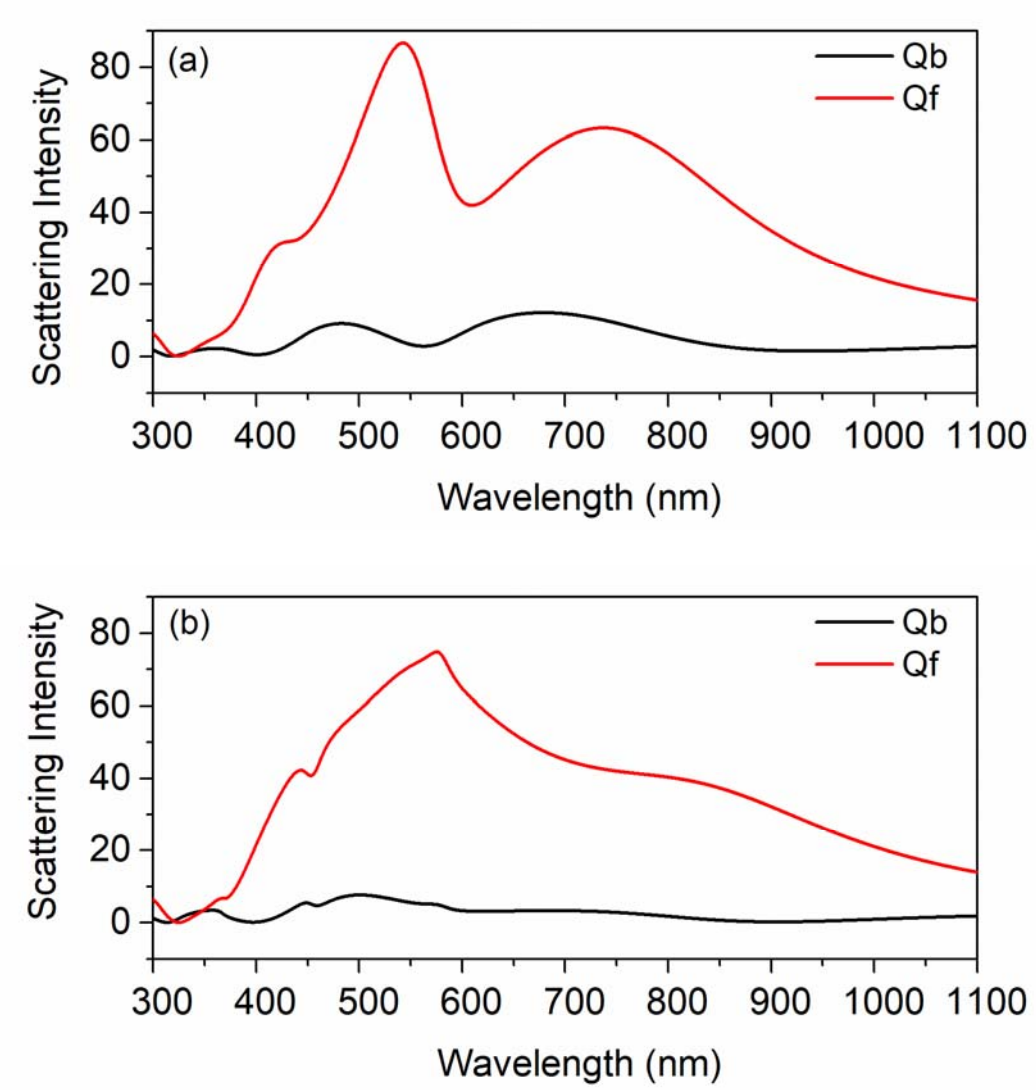

Figure 4.6: Forward and backward scattering efficiencies for two nanoparticles aligned along (a) electric field and (b) magnetic field.

To assess the feasibility of the designed nanostructure for the thin film Si solar cell applications, optical and electrical device simulations are made using the Lumerical FDTD and Device software package. A case under consideration is illustrated in Figure 4.7, where a monolayer of ITO nanoparticles (n=2) is placed atop the Si slab 500nm in thickness. With the refractive index ratio of the ITO nanosphere to the surrounding air set at 2, the forward scattering condition is satisfied.

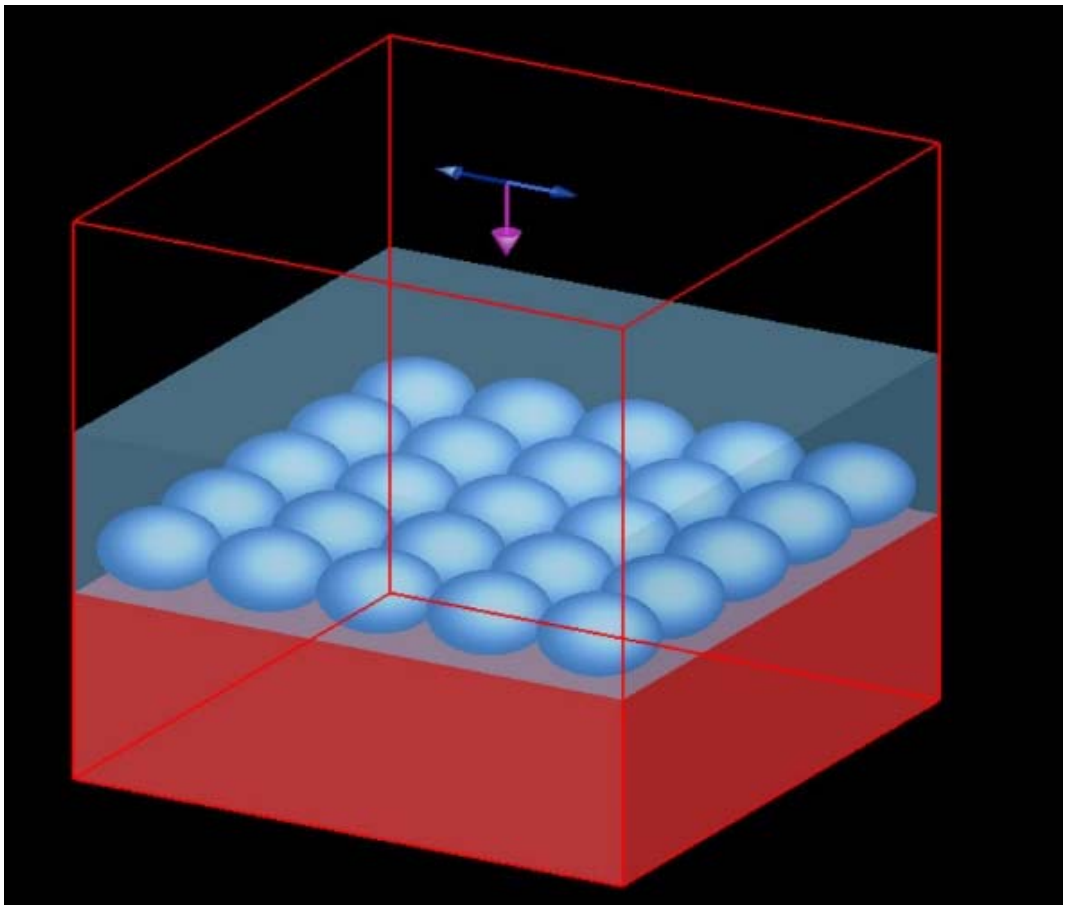

Figure 4.7: The designed structure with nanoparticle arrays placed atop the Si slab

As a comparison, numerical simulations were also carried out for other cases reported in literature, i.e., the moth eye structure in air, Si nanoparticle with ITO, ITO nanoparticles in air, TiO_2 nanoparticles in glass and the flat Si layer. The results of the light absorptions in the Si slab with and without nanostructures are plotted in Figures 4.8 (a), which clearly indicates that among the all cases examined a light trapping enhancement is best with the use of ITO-nanoparticles. From the electric field distributions over the cross-section, which are illustrated in Figures 4.8 (b) and (c), it is clear that the forward scattering by the nanoparticles is preserved. However, the light is strongly reflected at the interface between the nanoparticle and the slab. This may be readily explained by the Snell's law, that is, the relatively large difference of the refractive indexes across

the boundary between the air and the Si slab leads to a distinct reflection. To reduce the undesired reflection, the refractive index of the nanoparticle should be set close to that of the Si slab.

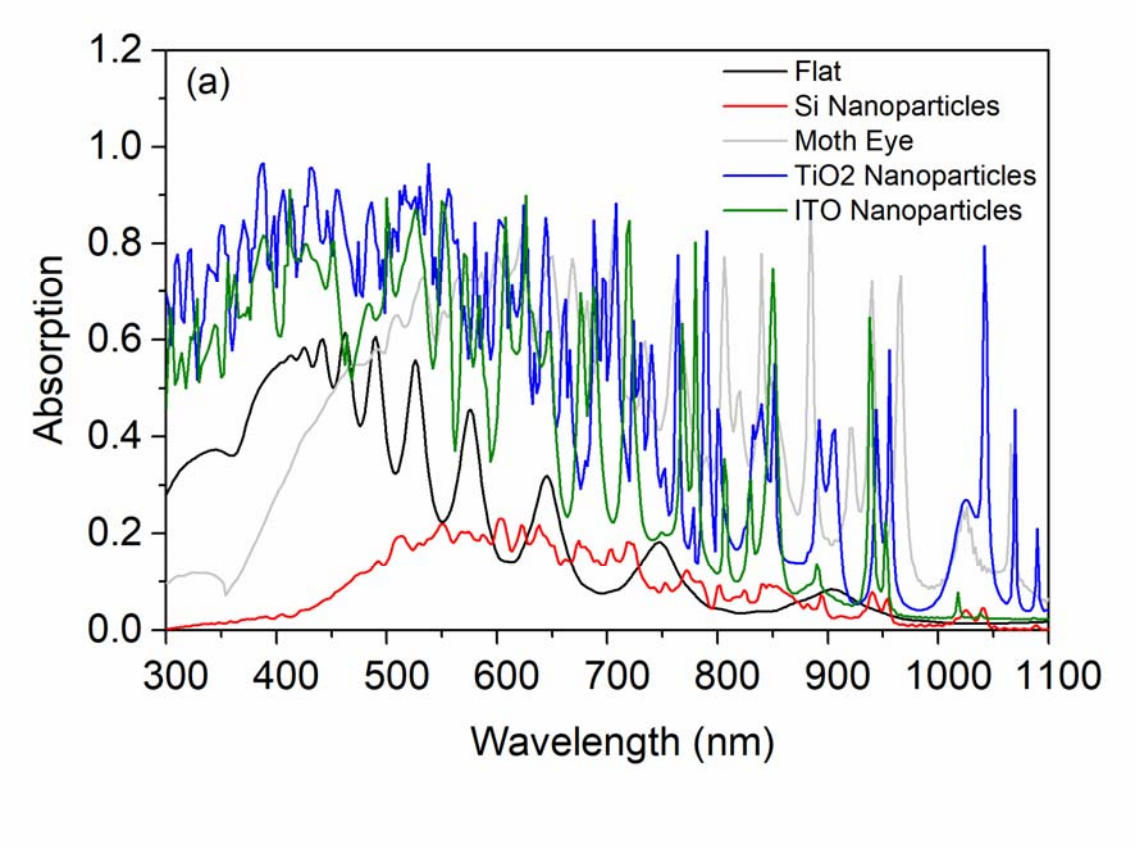

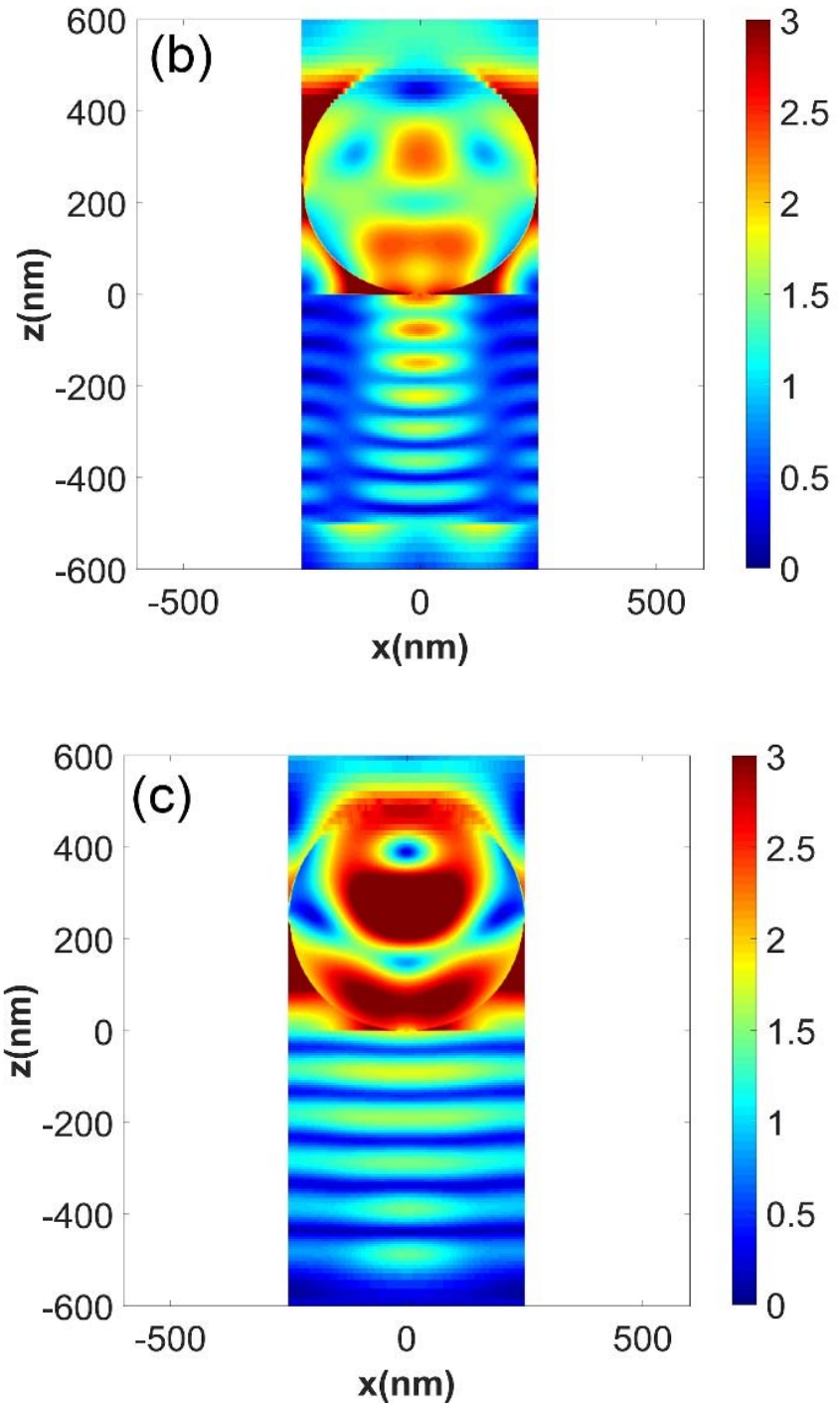

Figure 4.8: (a) Light absorptions inside the Si film with the moth eye structure (grey), Si nanoparticle with ITO as the surrounding medium (red), ITO nanoparticles in air (green), TiO_2 nanoparticles in glass (blue) and the flat Si layer (black). The electric field distribution at the cross-section for ITO nanoparticles with air medium atop the Si slab at (b) 550nm and (c) 692nm.

Accordingly, by combining both the above design principle and the Snell's law, the Si nanoparticle aggregates together with its ITO medium layer considered as a potential candidate. The light absorption inside the Si slab is marked as red in Figure 4.8 (a) for this configuration. Despite the fact the Snell's relation is satisfied, the light trapping results do not appear to be better. Analysis leads the culprit, that is, the Si nanospheres are not lossless over the solar spectrum, due to the nonzero imaginary part of the refractive index. Thus, even the reflection between the nanoparticles and the Si slab is reduced by replacing the ITO arrays with the Si arrays, the loss inside the Si nanoparticles deteriorates the overall absorption as the red curve in Figure 4.8 (a).

Therefore, effort is now turned to seek a lossless material that also has a refractive index close to the Si slab. Examination of a wide range of materials suggests that TiO_2, which has a relatively large n value (2.8) but zero imaginary part, fits into the profile of a potential candidate. To ensure the forward scattering behavior, glass (n=1.4) is chosen as the surrounding medium. The calculated results for this configuration are shown as the blue curve in Figure 4.8 (a). The overall enhancement of absorption in this case is the best and the reflection across the glass/Si boundary is much reduced.

To further guide the light into the Si layer, partial embedment of the TiO_2 nanoparticles into the cell are considered. The electric field distributions for different embedding depths, i.e., 0nm, 25nm, 50nm, 100nm, 150nm and 200nm, are illustrated in Figures 4.9 (a)-(f). As can be observed, the leakage channel is broadened with the nanoparticle embedded. The wider the contact between the nanoparticle and the slab, the more light is leaked forwardly into the slab. After a certain depth of embedment, the nanoparticle starts to lose the forward scattering feature since the influence from the Si slab is no longer negligible. To achieve the best performance, the absorption enhancement in the Si solar cell with varying TiO_2 nanoparticle embedding depths are simulated

and the results are presented in plotted in Figure 4.9 (g). Apparently, when the TiO_2 particle buried 150 nm is into the Si slab, the overall enhancement of the absorption is maximized to 50.23%, which is better than any other cases studied. The short circuit current from electric device simulation also shows an improvement from 12.4 mA/cm^2 to 24.9 mA/cm^2, and the overall solar energy conversion efficiency is increased from 4.47% to 9.73%.

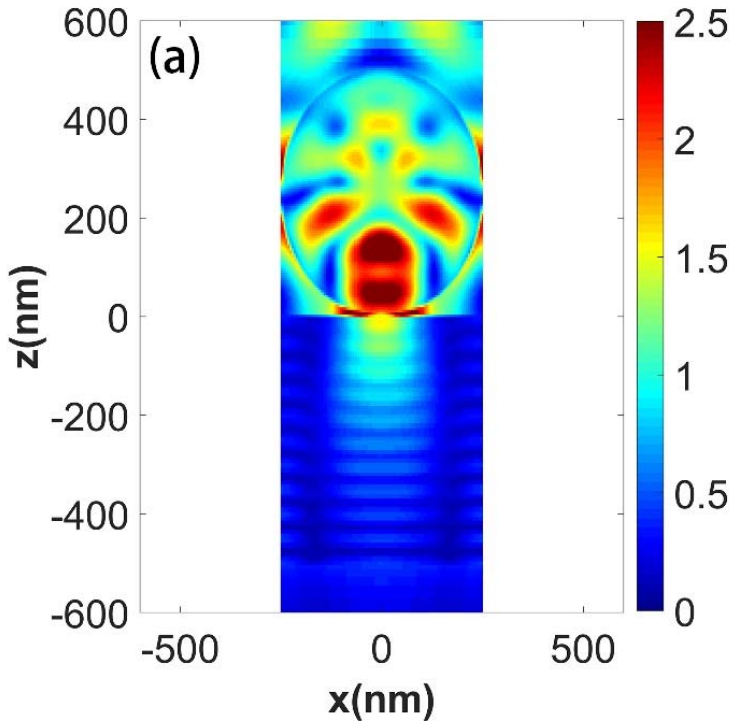

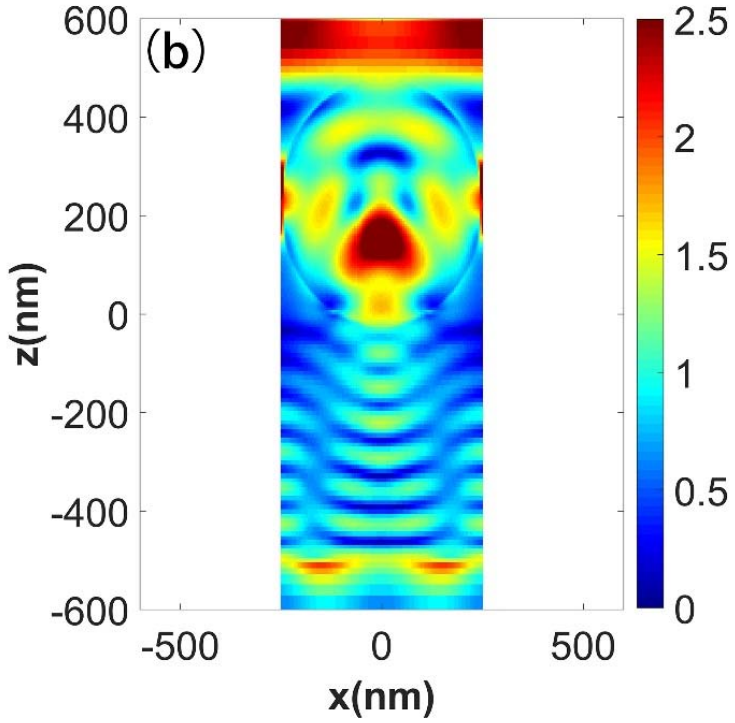
(b)
600
400
200
0
-200
-400
-600
z(nm)
-500
0
500
x(nm)
2.5
2
1.5
1
0.5
0

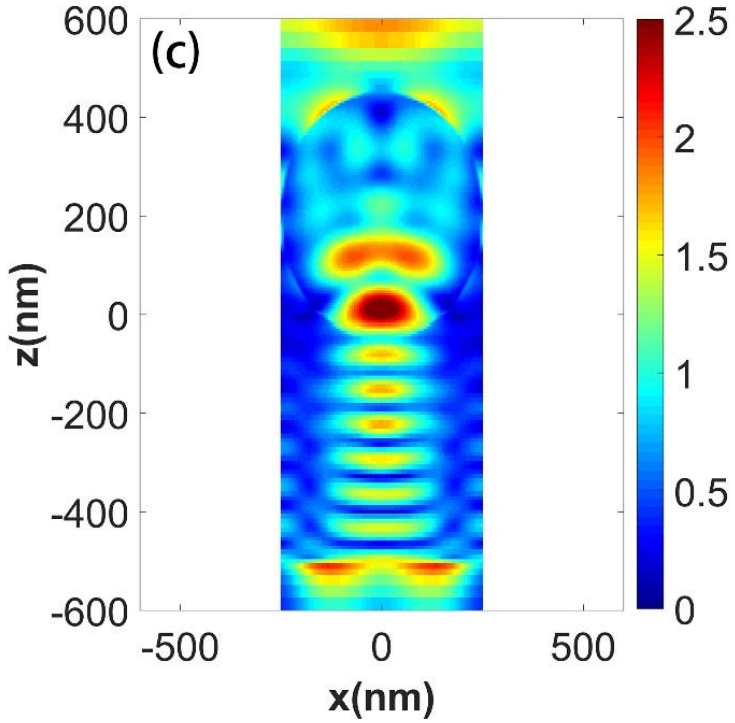
(c)
600
400
200
0
-200
-400
-600
z(nm)
-500
0
500
x(nm)
2.5
2
1.5
1
0.5
0

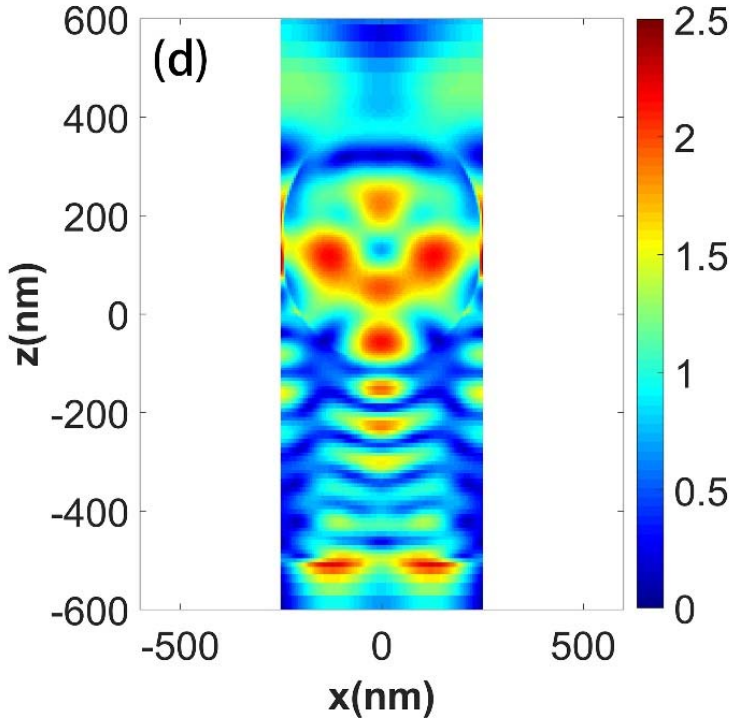
(d)
600
400
200
0
-200
-400
-600
z(nm)
-500
0
500
x(nm)
2.5
2
1.5
1
0.5
0

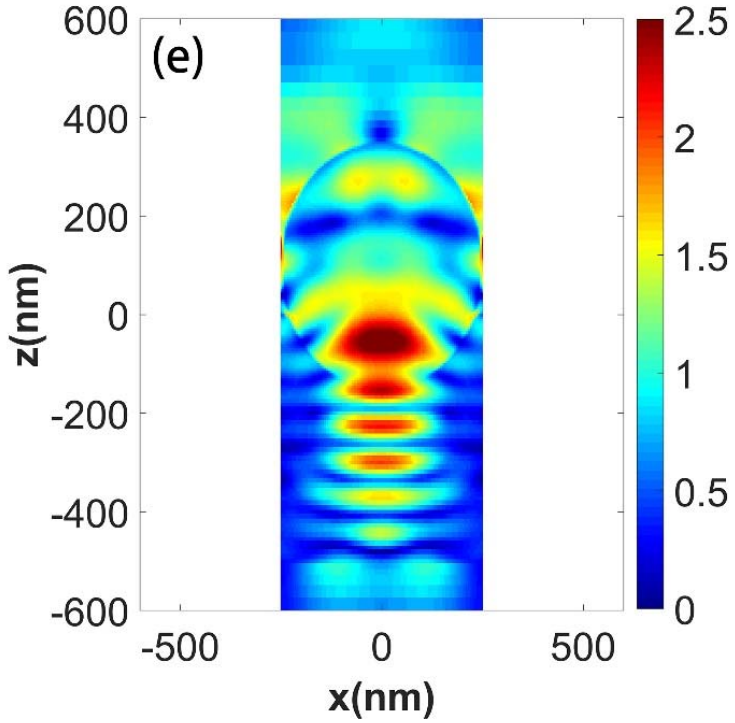
(e)
600
400
200
0
-200
-400
-600
z(nm)
-500
0
500
x(nm)
2.5
2
1.5
1
0.5
0

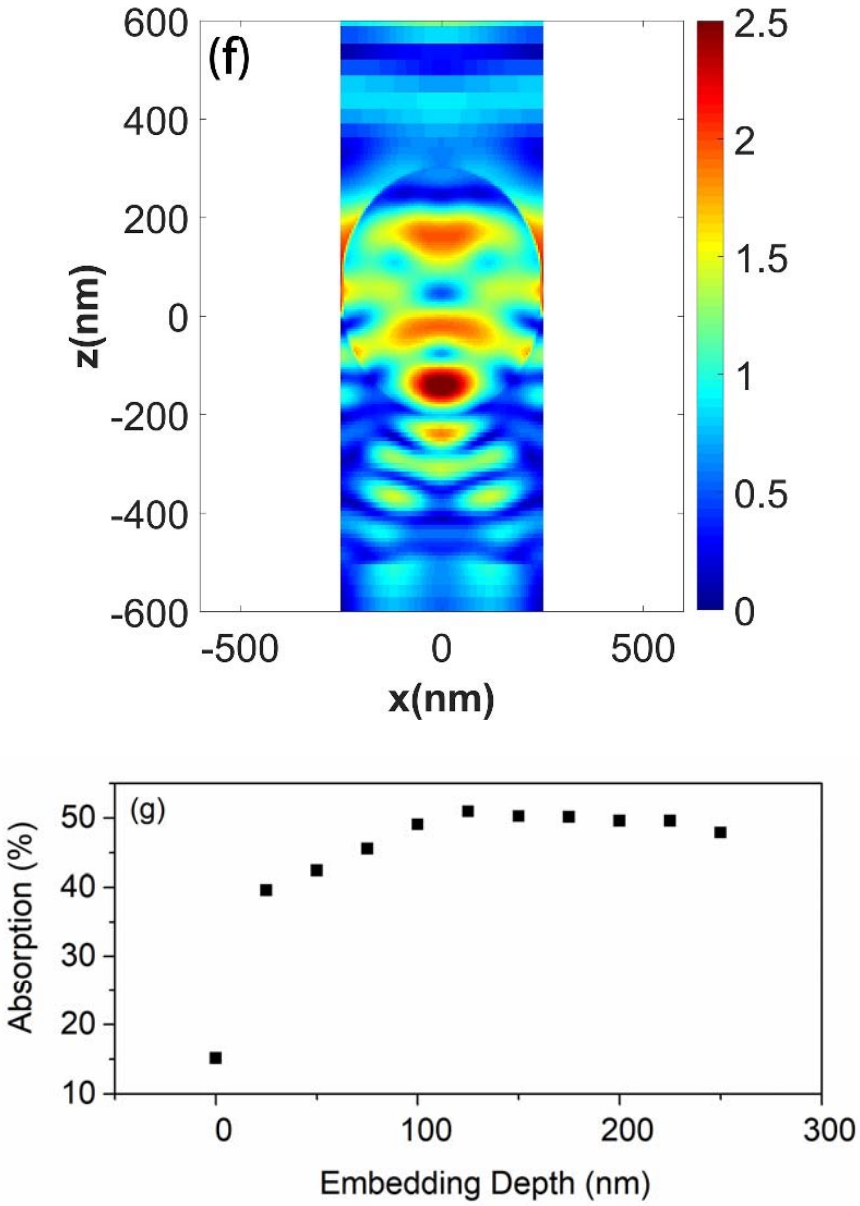

Figure 4.9: (a)-(f) Electric field distribution for different embedding depths as 0nm, 25nm, 50nm, 100nm, 150nm and 200nm. (g) The absorption enhancement compared to the flat case with different TiO_2 nanoparticle embedding depths.

FDTD simulations were also conducted to determine the effect of various parameters on the light trapping performance of the proposed nanostructure, which include the diameter of each nanoparticle D, the embedding depth h and the thickness of silicon thin film t. Figure 4.10 (a) plots the integral light absorption efficiency A_{int} of a 500 nm thick Si film with different combination of

nanoparticle diameters and embedding depths. It is apparent that there exists an optimized ratio between the embedding depth and the nanoparticle diameter, which is about 0.2 for each case. That is, for TiO_2 nanoparticles with different diameters, i.e., 300 nm, 500 nm and 1000 nm, the optimized embedding depth are 60nm, 90nm and 200nm, respectively. This can be explained that more light is guided into the active layer as long as the embedding depth increases. However, beyond a certain point, the nanoparticles start to lose the capability of further increase in scattering, leading to a reduction of the absorption in the silicon layer.

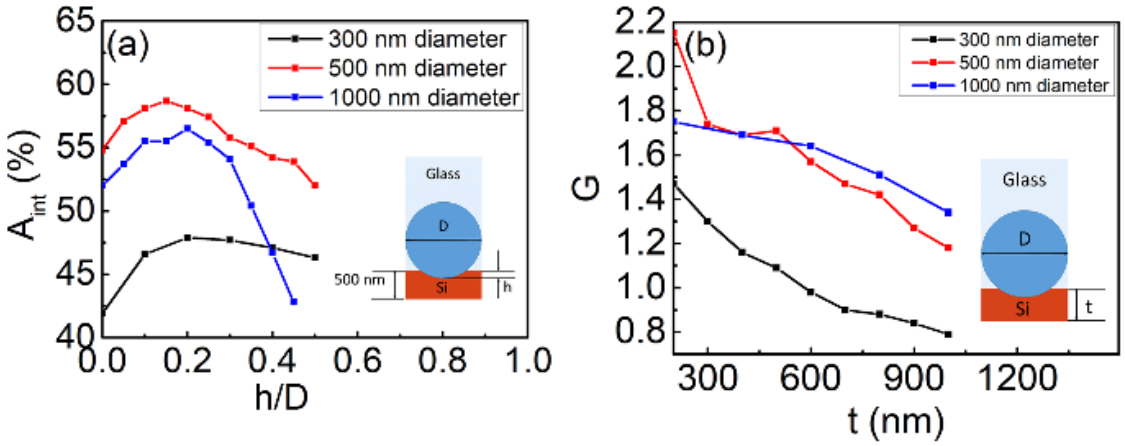

Figure 4.10: (a) Light absorption integrated over the wavelength range (A_{int}) of the Si thin film with different nanoparticle diameters as a function of the ratio between embedding depth h and nanoparticle diameter D. The integral absorption for the flat Si film is 23.68%. (b) Ultimate efficiency enhancement factor G of Si film with different diameters of the nanoparticle as a function of the Si film thickness t. h/D = 20% for each case.

With an optimal embedding ratio, the Si film thickness and the diameter of TiO_2 nanoparticle can be optimized. Figure 4.10 (b) plots the ultimate efficiency enhancement *G* of Si film with different diameters of the TiO_2 nanoparticle as a function of the Si film thickness t. The optimized ratio (h/D=20%) is applied for each case. The ultimate efficiency enhancement *G* decreases as the Si film thickness increases for each case. This is attributed to the fact that the light

absorption is enhanced mostly near the nanoparticle-Si film interface. As the light further propagates into the Si film, less enhancement effect is observed. It is noted that forward scattering usually occurs over a narrow cone. For a thin film, a wide-angle scattering is more beneficial. With partial embedding and closely packed array arrangement, the forward scattering structure discussed in the present study appears to allow sufficient lateral scattering to be achieved.

In passing, we note that nanomanufacturing procedures for creating partial embedding of nanoparticles into thin films now have been well established and can be readily adopted into the existing the silicon solar cell fabrication operations [65]. One possible procedure to fabricate the designed structure can be summarized as follows. Firstly, clean a glass substrate and spin coating a layer of photoresist on it. Secondly, transfer a monolayer of TiO_2 nanoparticles on top of the photoresist coating. Then, deposit a Si film to cover the nanoparticles, which followed by removing the photoresist with acetone. Selectively ion etch the Si film with SF6 plasma to expose the TiO_2 nanoparticles, which forms the partial embedding nanoparticles-Si film structure. Finally, deposit a SiO_2 layer to on top of the whole structure.

4.3 Concluding Remarks

In summary, this section has presented a novel nanostructure, consisting of TiO_2 nanoparticle arrays embraced in a glass medium and partially embedded a thin film Si solar cell, for light trapping over the solar spectrum. An addition-theorem recursive electromagnetic computational algorithm has been applied to identify forward-scattering nanoparticle structures by matching the multi-mode magnetic and electric responses through tuning the structural parameters of nanoparticles or particle clusters in relation to their surrounding media. The TiO_2 nanoparticles in glass medium is considered as an optimal choice. Light reflection is further reduced by embedding the nanoparticles partially into the substrate. The effect of the Si film thickness, the nanoparticle

diameter, and the embedding depth was studied. An short-circuit current density enhancement of 215% over a bare thin film Si cell (or 3.15 times light absorbing) can be achieved with a nanostructure of 500nm TiO_2 nanoparticles with a 90nm embedding depth in a 200nm thick thin film silicon cell.

CHAPTER 5

Light Absorption Enhancement of Gallium Arsenide Solar Cell with Forward Scattering Nanoparticles

5.1 Introduction

In this chapter, we demonstrate a hybrid configuration consists of lossless nanoparticles with forward scattering feature and nanograting back reflector can enhance the performance of a thin film GaAs solar cells. The light scattering efficiency of the so designed nanoparticles aggregates is calculated using the Mie theory and the translational addition theorem. Moreover, the optical process for the configuration, which consists of the nanoparticles and the GaAs solar cells, are modeled numerically by solving Maxwell curl equations. Significant enhancement of the light absorption in the active layer of GaAs solar cell is observed with the proposed nanoparticles due to the forward light scattering from the nanospheres. Moreover, the light loss in the nanoparticles can be avoided by using dielectric material. More incident light is guided inside the GaAs solar cell via embedding the particle partially in the absorbing layer. In addition, the absorption can be further enhanced by adding a rectangular nanograting back reflector, which mainly reflect the light in the long wavelength range. A maximum light absorption improvement as high as 56% has been achieved by combining the forward scattering nanoparticles with the optimized Ag nanograting back reflector compared to a plane GaAs solar cell.

5.2 Results and Discussion

The metal nanoparticles possess both radiative (scattering) and nonradiative (absorption) properties while the dielectrics show only radiative behavior. For the metals, the oscillation of the

electrons cloud generates an induced field, which scatters electromagnetic wave outward. The collision between the moving electrons and the molecules generates the nonradiative absorption. The excellent scattering property of noble metals, i.e., Ag, Au and Al, is beneficial for the solar cell absorption, while the intrinsic losses deteriorates the overall performance. The dielectric nanopheres, without heat losses, usually have low scattering ability. In a word, the ideal nanoparticles for solar cells application need to be lossless and have great scattering ability especially in a certain direction.

The scattering property of Ag and Au are investigated here as representatives for metals. The radii of both cases are 50nm. The total scattering efficiencies of single Ag nanosphere and Au nanosphere are plotted in Figure 5.1 (a) and (b) where a_1, b_1, a_2 and a_2 represent the electric dipole, magnetic dipole, electric quadrupole and magnetic quadrupole components, respectively. It can be seen that the electric dipole component dominates for Ag and Au nanoparticles while all other modes can be neglected. To further study the radiation directions, the scattering patterns of Ag and Au nanospheres at their peak wavelengths, which are 410nm and 540nm respectively, are shown in Figure 5.1 (c) and (d). The results show that both cases have equally distributed radiation along forward and backward directions. That is, the electromagnetic energy scattered in backward direction is lost as the metal nanoparticles applied on top of GaAs solar cells.

In many works, the metal-dielectric core/shell nanoparticles are introduced to enhance the overall solar performance. The light scattering efficiency with all the components for Ag/SiO_2 core/shell structure with 50nm Ag core and 20nm thick SiO_2 shell are plotted in Figure 5.1 (e). Compared to the Ag solid nanosphere, the scattering peak is shifted to 475nm without enhancement of the peak efficiency. This is attributed to that the SiO_2 layer with the refractive index as 1.5 attenuates the incident wave speed, which consequently slows down the oscillation of

the electrons cloud in Ag core. In addition, the dielectric shell layer is beneficial for solar cells performance since it avoid the direct contact between the Ag core and the active absorbing layer.

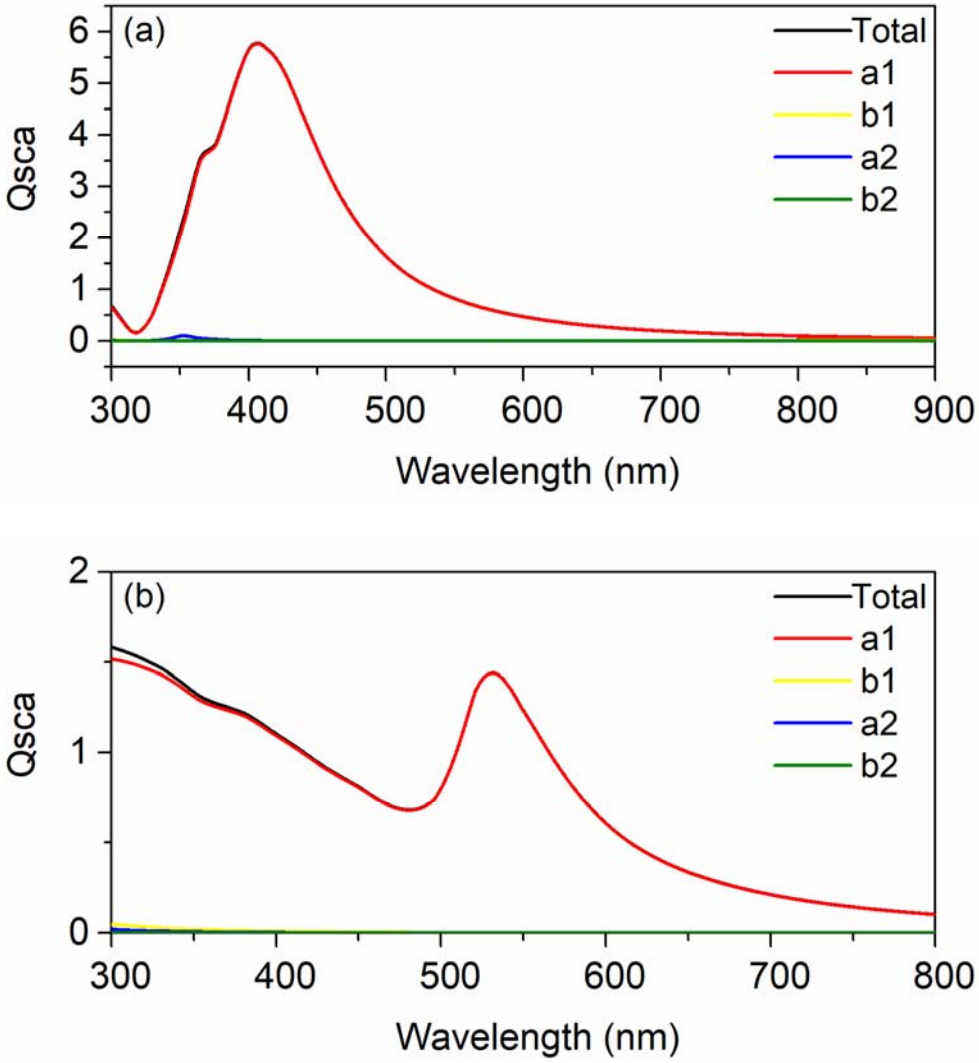

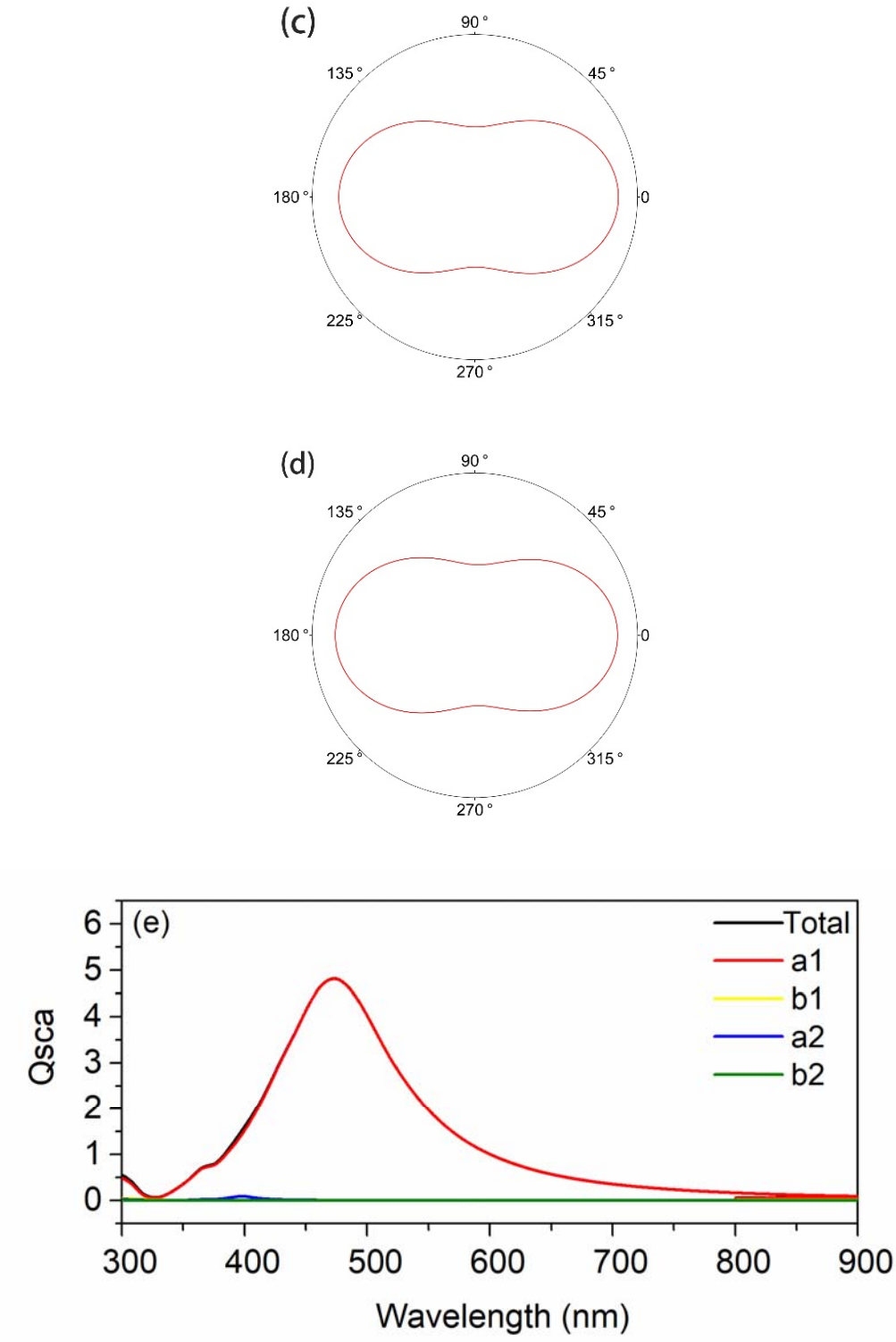

Figure 5.1: Total scattering efficiency with multiple contributions of (a) Ag nanosphere, (b) Au nanosphere and (e) Ag/SiO2 core/shell nanostructure. (c) The scattering pattern of Ag nanosphere at 410 nm. (d) The Scattering pattern of Au nanosphere at 540 nm.

Unlike the metals, nanoaprticles made of dielectrics possess both electric and magnetic modes. In this part, we investigate the light scattering properties for dielectrics and semiconductors with different refractive indices, i.e., SiO_2 (n=1.45), ZrO_2 (n=2.1), TiO_2 (n=2.8) and Si (n=4), to seeking the optimized material for the forward scattering. All the radii of the nanoparticles are set to 150 nm, allowing comparison of the scattering ability. Figure 5.2 (a)-(d) show the scattering efficiency and each mode component for SiO_2, ZrO_2, TiO_2 and Si, individually. From the result, as the refractive index increases, the peaks of each mode shift to the red. The electric and magnetic dipoles for ZrO_2 coincide, which meets the first Kerker's law. As the index increases further, the peaks start to be separated. The mechanism can be explained as follows. The refractive index describes the ability to decelerate the light. The higher the index, the slower the light speed inside the sphere, which results in the lower frequency of the electrons oscillation. Furthermore, the propagating distance of the displacement current in the magnetic dipole mode are longer than that in the electric dipole mode. Therefore, the peak wavelength of the magnetic dipole shifts more to the red than that of the electric dipole. As can be seen in Figure 5.2 (d), the overlapping region of the electric and magnetic dipoles modes fits the second Kerker's law, which can be used to scatter the light in backward direction.

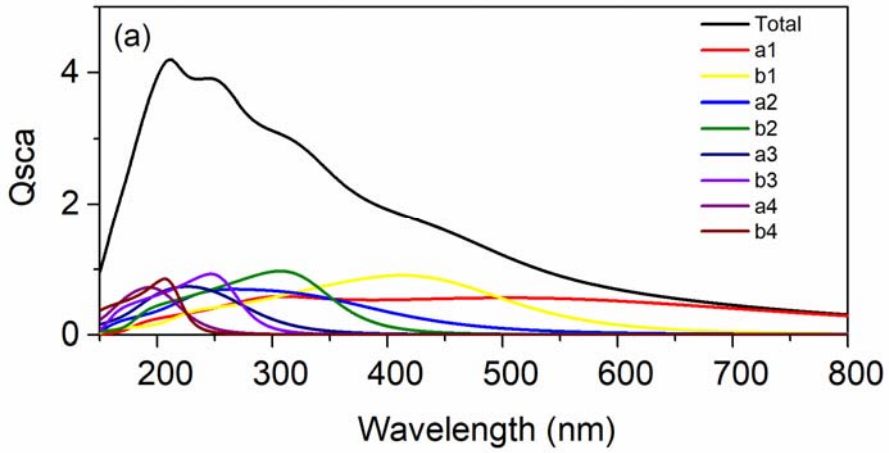

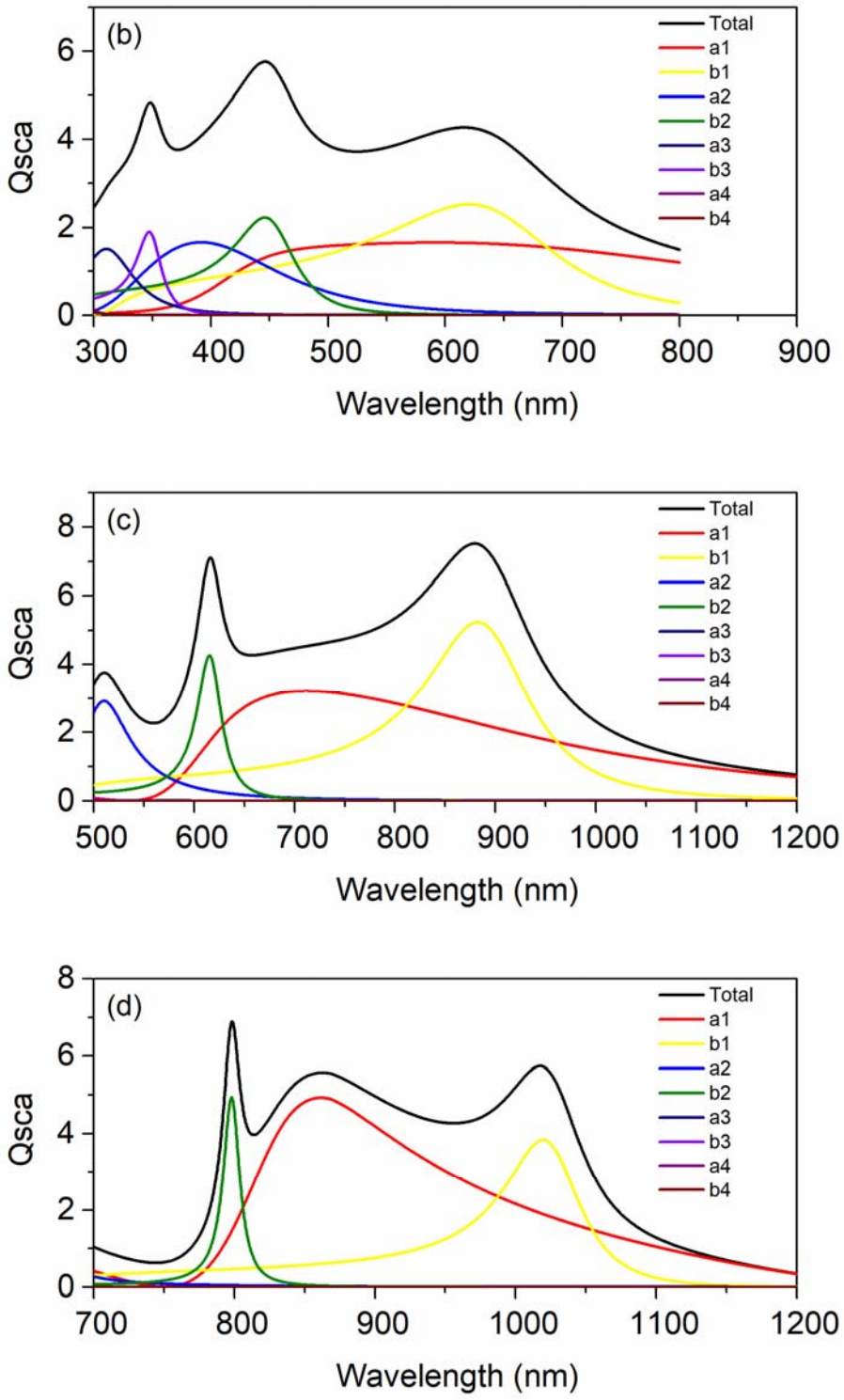

Figure 5.2: Total scattering efficiency with multiple contributions of (a) SiO_2 nanosphere, (b) ZrO_2 nanosphere, (c) TiO_2 nanosphere and (d) Si nanosphere, individually.

To verify the above viewpoint, the forward and backward scattering intensities for all the four nanoparticles are shown in Figure 5.3 (a)-(d). It is obvious that the ZrO_2 nanoparticles provides the highest forward scattering intensity about 36 dues to the overlapping of the modes. Since the refractive index of ZrO_2 is nearly constant about 2.1 for the whole wavelength range, the forward scattering behavior can be tuned for different wavelength by simply varying the radius. In addition, the backward scattering feature for Si nanoparticle between 900nm to 1000nm region, which is shown in Figure 5.3 (d), can be used for light reflecting application. Moreover, the absorption inside the semiconductors cannot be neglected, which will deteriorate the overall solar cell performance. As a result, the design principle need to be seeking a lossless dielectric material with refractive index around 2, which has greater scattering ability in the forward direction.

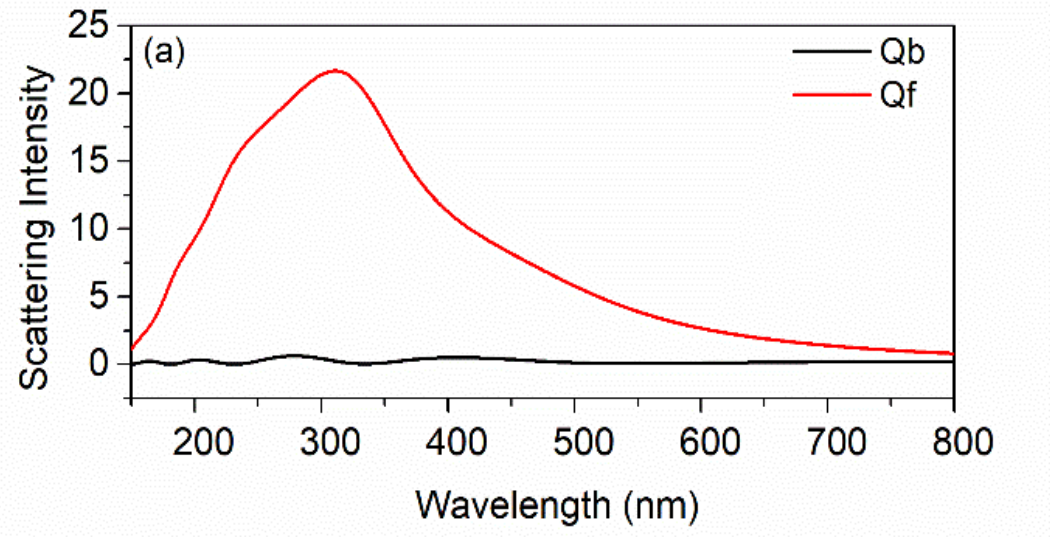

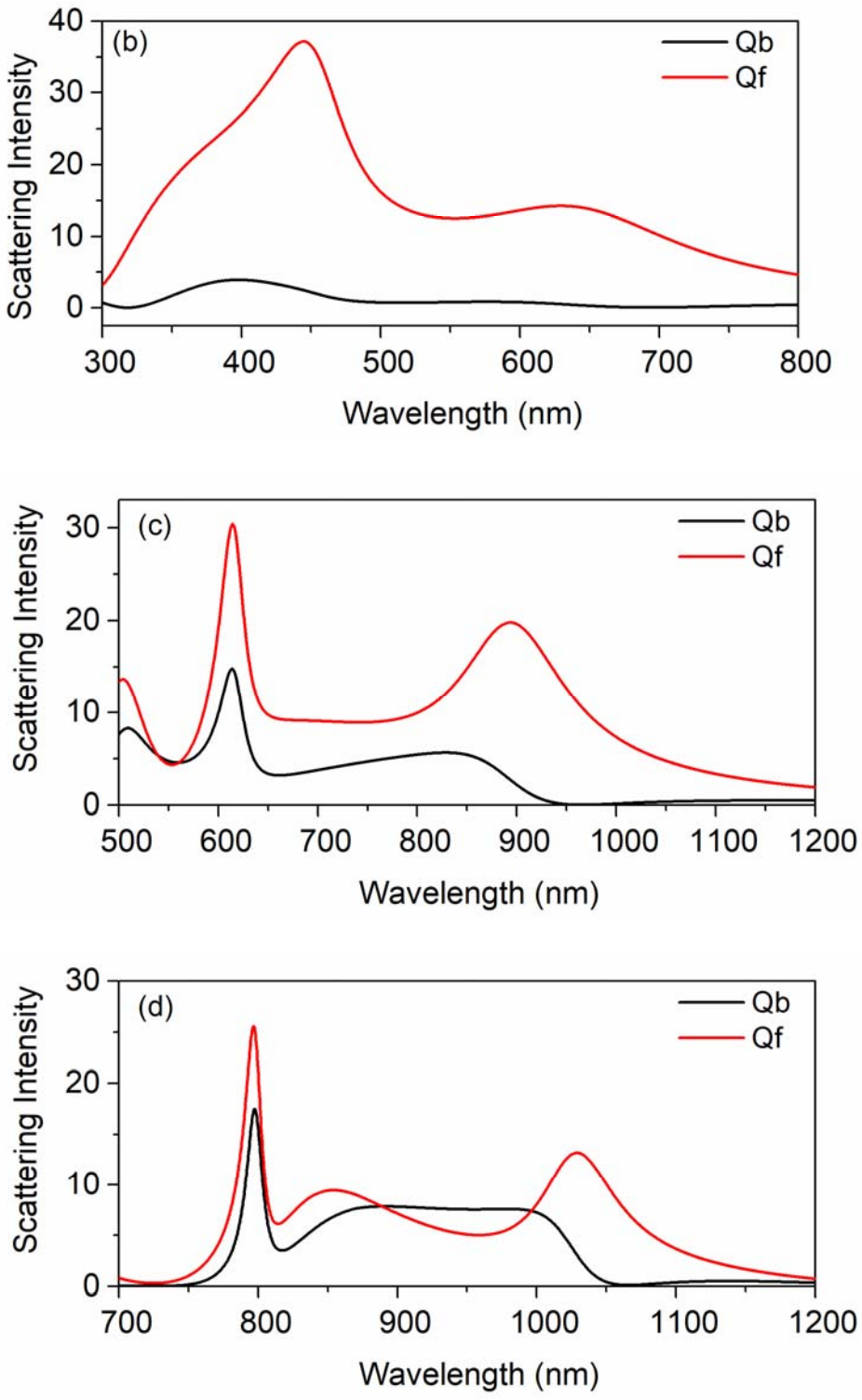

Figure 5.3: Forward and backward scattering intensity of (a) SiO_2 nanosphere, (b) ZrO_2 nanosphere, (c) TiO_2 nanosphere and (d) Si nanosphere, individually.

From the above result, the nanoparticles with refractive index about 2 is optimized for the forward scattering. This condition can be further expanded to the situations where the refractive indices ratio between the nanoparticle and the surrounding medium as 2. The advantage of this conclusion is that the material selection range are expanded. Moreover, the forward scattering intensity can be further enhanced by using higher refractive index dielectric materials as long as the ratio is kept as 2. To confirm this viewpoint, the forward and backward scattering intensities of TiO_2 (n=2.8) nanoparticle in glass medium (n=1.45) is studied and plotted in Figure 5.4 (a). The scattering intensity in forward direction reaches 75 at the peak wavelength. In addition, the Si (n=4) nanoparticle inside ITO (n=2) medium shows a higher forward scattering intensity. However, the semiconductor materials also has absorption loss, which makes them not suitable for guiding the light for the solar cell application. In other word, the TiO_2 nanosphere in glass is the optimized configuration scattering the light forwardly without any heat losses.

To apply the designed TiO_2 nanoparticle with glass medium atop of GaAs solar cells, the forward scattering feature need to be expanded to the nanoparticle arrays. With the help of addition theorem, the forward scattering efficiency of two TiO_2 nanoparticles aligned along the electric filed direction and the magnetic field direction are shown in Figure 5.4 (b) and (c), individually. It can be found that the scattering feature changes less since the light is essentially radiated along the forward direction, which leads to less interaction between particles.

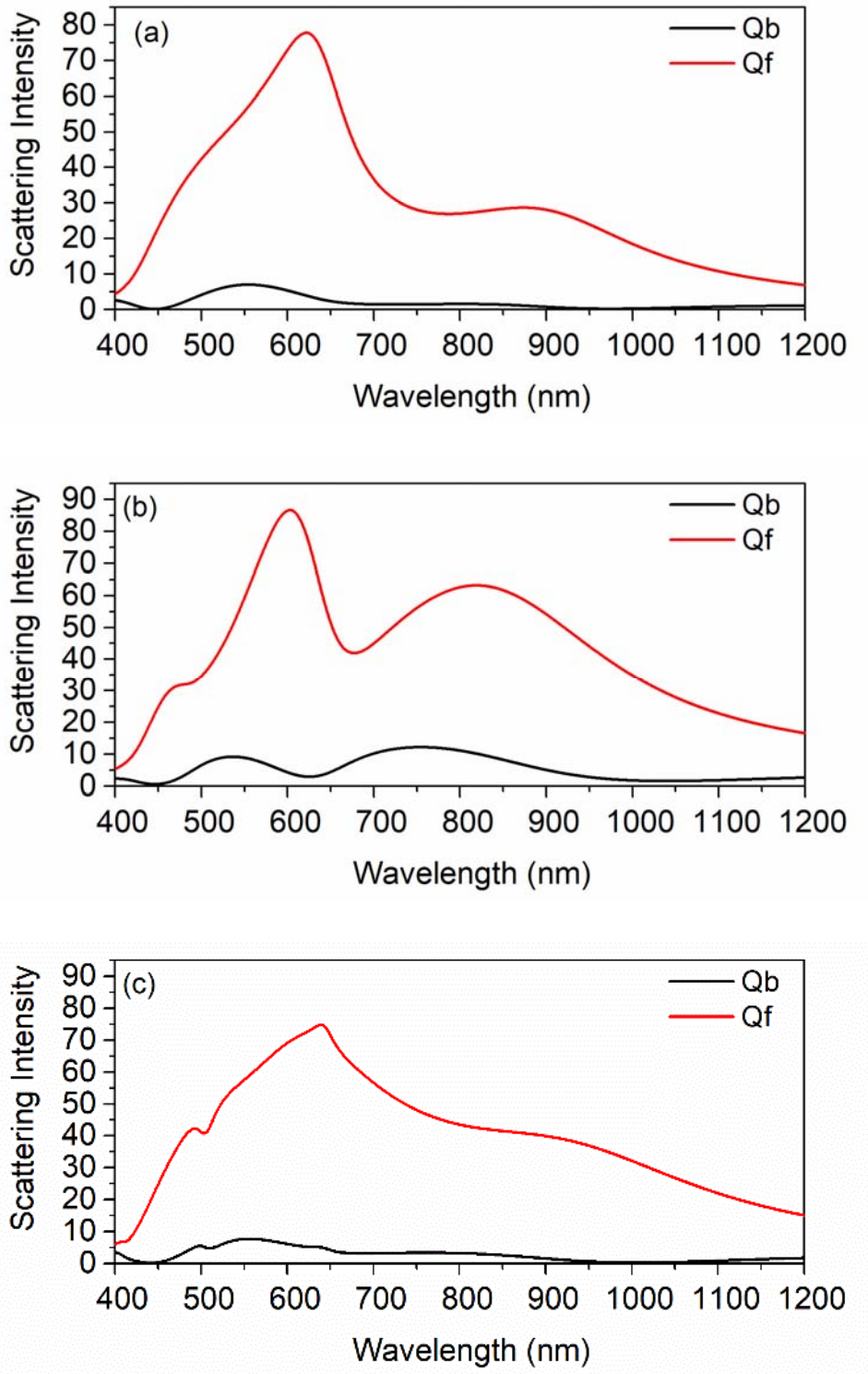

Figure 5.4: Forward and backward scattering intensity of (a) single TiO_2 nanosphere in glass medium, (b) two TiO_2 nanospheres along electric field direction and (c) two TiO_2 nanospheres along magnetic field direction.

TiO_2 nanoparticle with Glass Medium atop and Embedded in GaAs Solar Cells. To investigate the enhancement of solar cell performance with the designed TiO_2 nanoparticles and glass medium atop, the optical and electric process inside the GaAs solar cells are numerically simulated by the Lumerical FDTD and Device packages. The overall system structure is shown in Figure 5.5 (a). The thickness of the GaAs layer is 1700nm. The designed TiO_2 nanoparticles, which embedded in glass and has 250 nm radius, is applied atop of the GaAs solar cells. The light is propagating from the top and two transmission monitors are set at the top and bottom surface of the active layer. The light absorption inside the active layer is determined as the difference of the transmission between the above two layers. The absorption of the GaAs solar cells with TiO_2 nanoparticles and glass atop is plotted in Figure 5.5 (b) compared to that of the plane GaAs solar cells. It can be seen that the absorption is enhanced nearly the whole range of the solar spectrum. However, there still exists reflections between the TiO_2 nanoparticles and the top surface of GaAs solar cells, which can be found in the electric filed distribution profile in Figure 5.5 (c). To further guide the light into the active layer, the TiO_2 nanoparticles are embedded partially inside the GaAs solar cell. As the embedding depth increases, the light absorption is enhanced since the contact surface between the TiO_2 nanoparticles and the solar cells are broadened, where more light can be leaked to the active layer. After a certain depth, the absorption starts to decrease, which is attributed that the further embedding leads to the loss of the forward scattering feature. The optimized depth is found to be 150nm, and the electric field distribution at 560nm is shown in Figure 5.5 (d). It can be seen that more light is leaked into the GaAs solar cell.

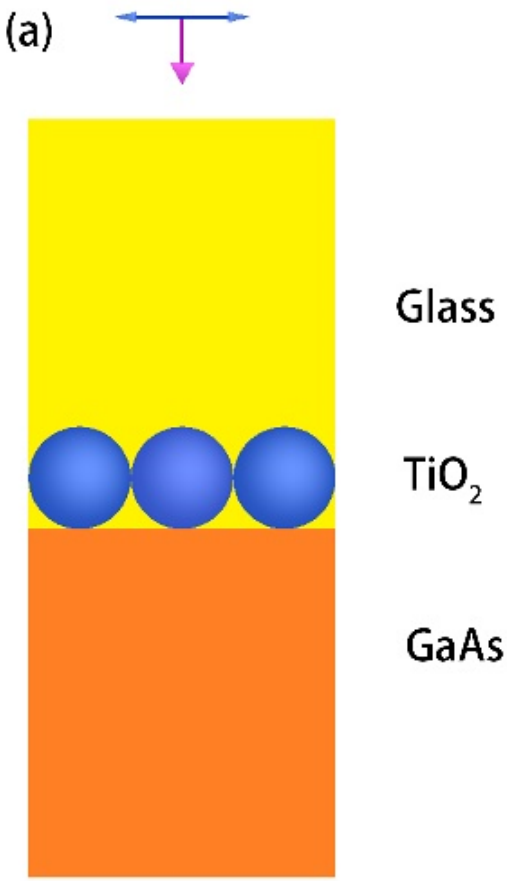
(a)
Glass
TiO2
GaAs

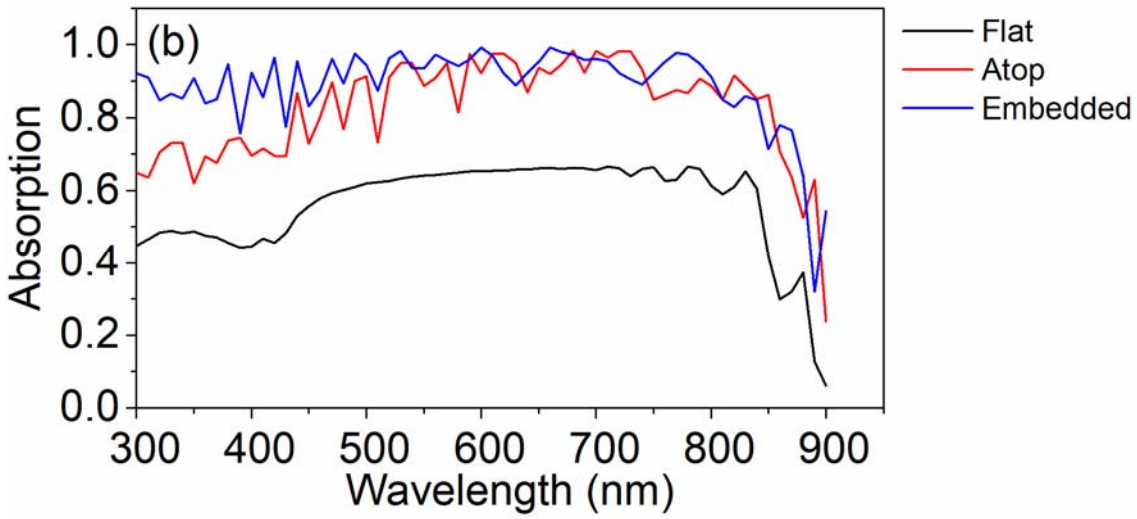
(b)
Absorption
Wavelength (nm)
Flat
Atop
Embedded

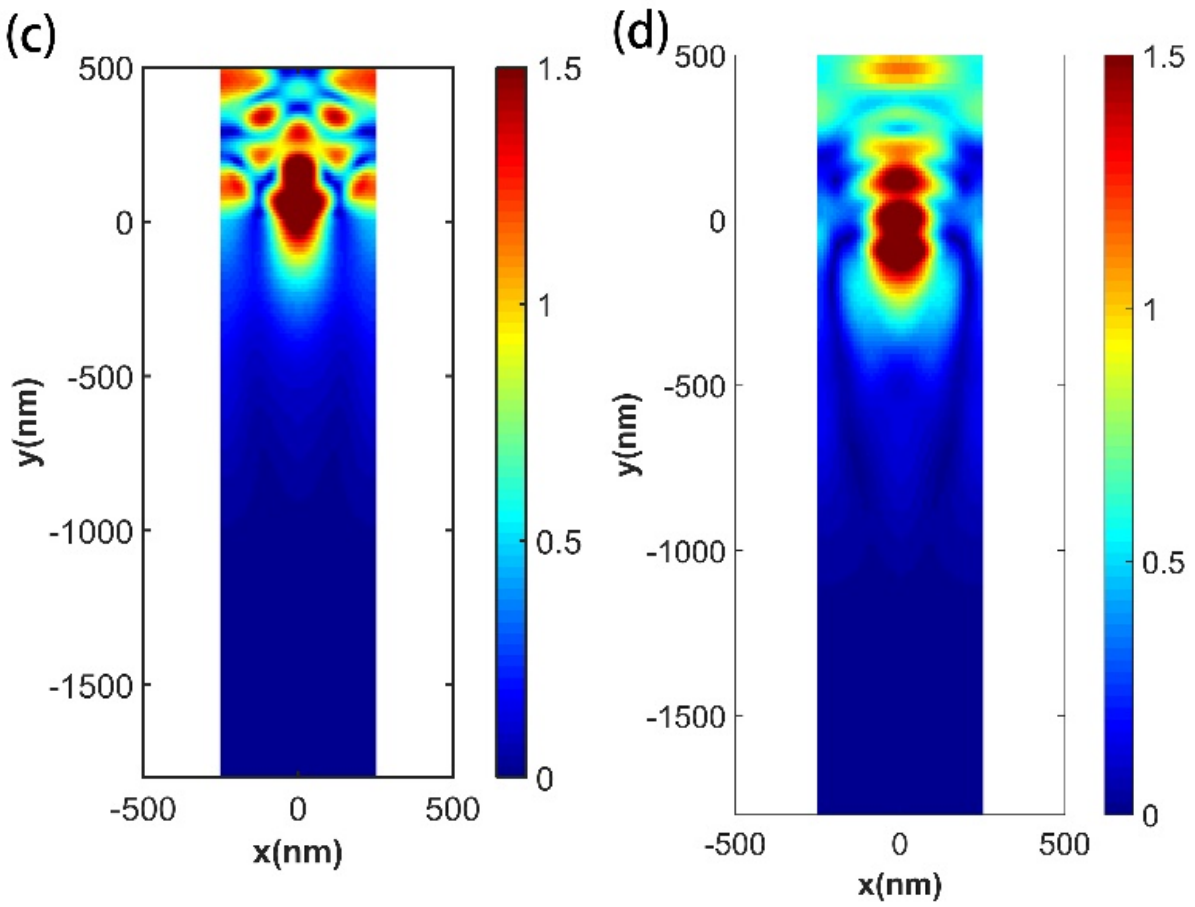

Figure 5.5: (a) The designed structure with nanoparticle arrays placed atop the GaAs slab. (b)The absorptions inside the GaAs solar cell with the TiO2 nanoparticle and glass medium atop (red), embedded 150nm (blue) and the flat GaAs layer (black). The electric field distribution at the cross-section for (c) TiO2 nanoparticle and glass medium atop GaAs slab and (d) 150nm embedded at 560 nm wavelength.

To further improve the absorption inside the active layer, one promising choice is to utilize the nanograting structure as the back reflector. In this work, the hybrid structure consists of the embedded forward scattering particle and a periodic rectangular grating structure are investigated. The overall configuration is shown in Figure 5.6 (a). The combination of the designed top nanoparticles and nanogratings with different heights and widths are simulated and the optimized parameters are determined. The height of the Ag nanograting is 100nm while the width is 300nm. Figure 5.6 (b) plots the absorptions of GaAs solar cell with the hybrid structure (blue), which

includes the top forward scattering nanoparticles with the back reflecting gratings, with the top forward scatter only (red), with the bottom grating reflector only (yellow) and the flat cell (black). As can be seen, the nanograting boosts the absorption in the long wavelength range while the forward scatter does in the short wavelength range. To investigate the physical origin of this absorption enhancement, the electric field of the cross-section at 860 nm for flat GaAs cell, with forward scatter only, with back reflector only and with both forward scatter and back reflector are plotted in Figure 5.6 (c)-(f). It can be seen the top nanoparticles scatters light into the cell, while the bottom nanograting reflects light back to the active layer. The hybrid structure allows the GaAs to absorb more light than that of each structure applied individually. From the simulation result, the hybrid structure with optimized parameters boosts the absorption from 58.8% to 91.5% compared to the flat cells. That is, the overall light absorption has a relative 56% enhancement.

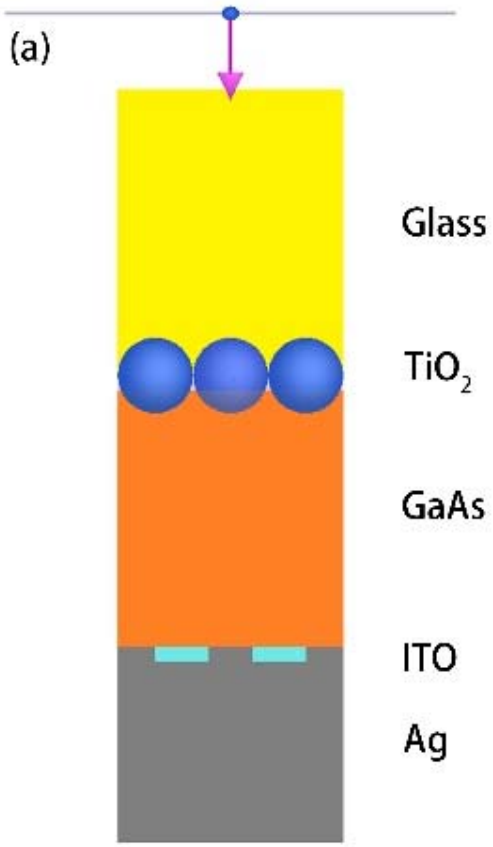

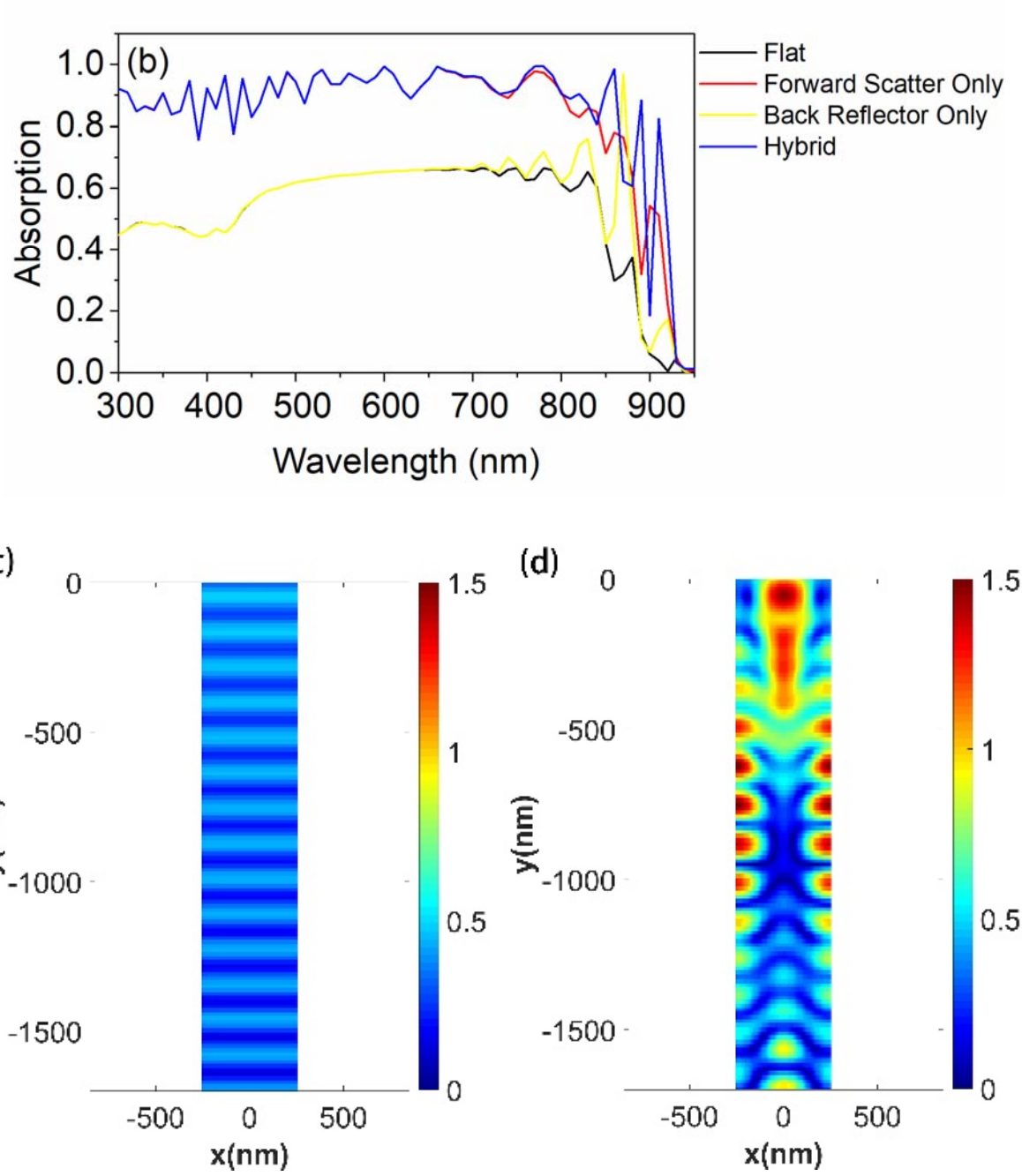
(b)
Absorption
Wavelength (nm)
Flat
Forward Scatter Only
Back Reflector Only
Hybrid
(c)
y(nm)
x(nm)
(d)
y(nm)
x(nm)

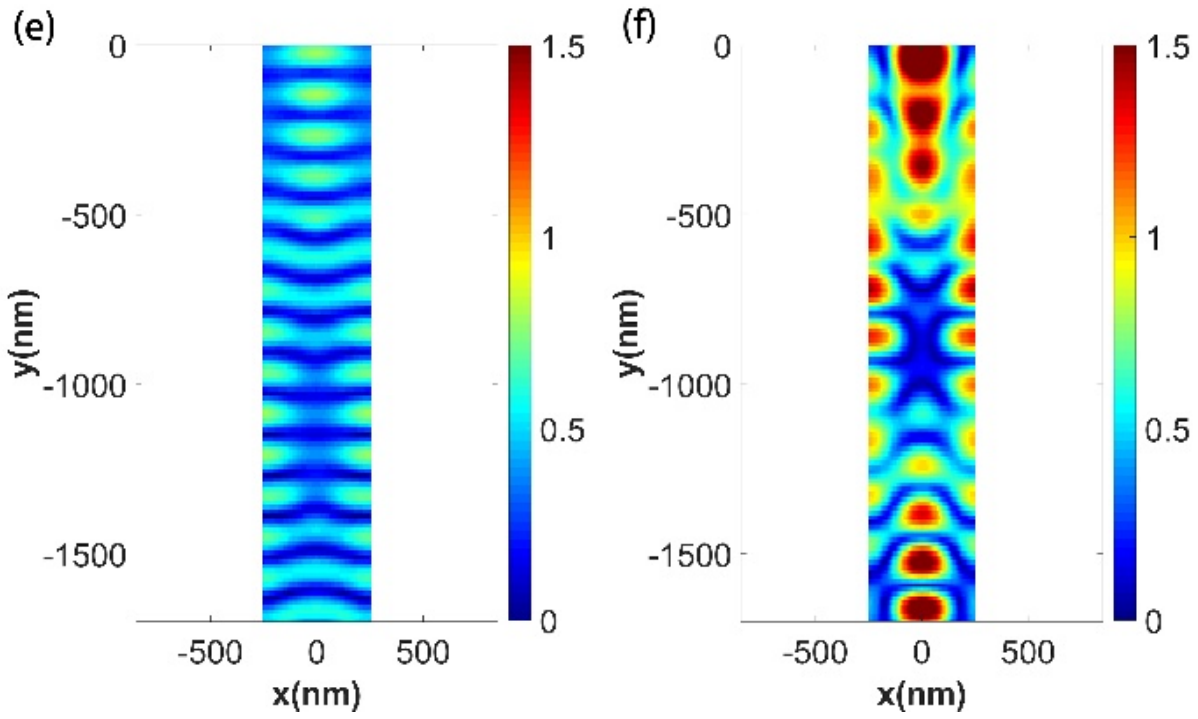

Figure 5.6: (a) The hybrid structure consists of the forward scatter and the nanograting back reflector. (b) The absorptions inside the GaAs solar cell with the top forward scatter only (red), the bottom nanograting only (yellow), the hybrid structure (blue) and the flat GaAs layer (black). The electric field distribution at the cross-section (c) with top forward scatter only (d) with bottom reflector only (e) with hybrid structures and (f) for the flat cell at 860 nm wavelength.

5.3 Concluding Remarks

This section incorporates nanostructure configuration, which consists of dielectric nanoparticles with glass medium, embedded partially inside GaAs solar cells to enhance the light absorption inside the active layer. The physical mechanism of the scattering properties for different materials is studied, which is utilized to guide the development of the forward scattering nanoparticles to meet the first Kerker's law. A back reflector is added to the structure to further enhance the absorption. The optical process of the overall configuration, both the top nanoparticle-medium structure and the bottom Ag nanograting back reflector applied to the GaAs solar cells, are modeled by the Lumerical FDTD package. Significant improvement of the solar cell absorption is observed and is better than that with each nanostructure applied alone.

CHAPTER 6

Light Absorption Enhancement of Core/Shell Nanoparticles

6.1 Introduction

In this chapter, we propose and demonstrate a general condition to enhance the light absorption for core/shell nanoparticles via tuning the electric and magnetic dipole components of the total absorption to the desired frequency. With the help of the analytical solution of the Maxwell equations, obtained by incorporating Mie theory with the addition theorem, we separated the total absorption efficiency into each mode component. We derived the condition for the enhanced absorption, which requires the electric and magnetic dipole modes to possess the same peak wavelength and minimal phase difference. The developed Ge/Au/Ge core/shell structure is superior to conventional nanoparticles, i.e., Au nanoparticle, Au/SiO_2 core/shell nanoparticle and Ge nanoparticle, due to the existence of both electric and magnetic components simultaneously rather than a single mode. The present condition is applicable for different wavelengths and different surrounding mediums, i.e., water and molten salt, for diverse applications. A peak absorption efficiency as high as 3.2 has been achieved of the Ge/Au/Ge core/shell nanoparticle in water compared with the Au nanoparticle of 2 and Ge nanoparticle of 2.3 with the identical radii, respectively. Moreover, the enhanced absorption condition also works for a cluster of nanoparticles. Our findings open possibilities for light-induced heating applications with core/shell nanoparticles.

6.2 Results and Discussion

To better design the core/shell nanoparticles, the physics origin of different modes components should be investigated first. The total extinction consists of the scattering and the absorbing modes, i.e., dipoles, quadrupoles and octupoles. For metals, the electrons are free in the molecules. As the light incident, the free electrons inside metal spheres move along the opposite direction of the applied electric field. That is, the periodic changes of the income field of the plane wave leads to the oscillation of the electron cloud. For different metal materials and nanoparticle sizes, there exists a certain wavelength that the oscillation of the electrons is maximized, which corresponds to the Surface Plasmon Resonance (SPR). The oscillation of the electrons leads to the radiative decay of the electromagnetic energy, which is the scattering portion. As the electrons move due to the applied field, the collision between the electrons and the molecules will contribute to heat loss, which corresponds to the absorption portion. For metal nanoparticles, the most frequent observed mode is the electric dipole absorption and scattering modes. For dielectrics, the electrons are bonded to the molecules, which makes that the electrons cannot move freely inside the particle. However, the electric dipole moment is formed as the medium is polarized by the income field. The summation of all the electric dipole moments leads to the displacement currents, which then constructs different modes, i.e., electric dipole, magnetic dipole, electric quadrupole and magnetic quadrupole. Nonetheless, there only exists scattering modes in dielectric nanoparticles. That is, there is no heat absorption since the imaginary part of the refractive index is zero. For semiconductor materials, there exist both scattering and absorption modes. As the particle size smaller than the wavelength, the dominant modes are electric and magnetic dipoles. The peak frequencies of these two modes are essentially different due to that the displacement current oscillation back and forth for the electric dipole while it moves in the tangential direction to provide the magnetic dipole. The

metal/semiconductor core/shell structure can combine the electric dipole in metals with the electric and magnetic dipoles in semiconductors, which provide the opportunity to enhance the total absorption by overlapping the effective electric and magnetic dipoles. Therefore, the influence of the material properties and nanoparticle sizes on the absorption peak behavior need to be investigated.

Gold nanosphere is a promising representative of metal nanoparticles with excellent absorption properties. Therefore, we investigate the light absorption properties of Au nanospheres in details. The total light absorption efficiency with each mode component of Au nanosphere are shown in Figure 6.1 (a).The electric and magnetic dipoles and quadrupoles are denoted as a_1, b_1, a_2 and b_2, respectively. The radius is set to 80 nm. As can be seen, the total light absorption is mainly from the electric dipole component contribution. The higher order electric modes are relatively weak and can be explained as follows. The oscillation distance for the higher order modes is shorter than that of the dipole, which results in that the peak of higher orders locates at a higher frequency. As the particle size is less than the incident light wavelength, the electric dipole mode is dominated while the higher orders can be neglected. The origin of the magnetic dipole requires the circulation displacement current, which is weak in the metals since the electrons are greatly free in metals.

Due to the extraordinary scattering ability, Ag nanospheres are widely used to trap the light in different nanostructures. Here, the absorption efficiency and each mode components of Ag nanosphere with 80nm radius are calculated and plotted in Figure 6.1 (b). The total absorption is mainly from the electric quadrupole term. Moreover, the absorption ability is relatively lower than that of Au nanoparticle with the same radius. That is, the Ag nanoparticle is more beneficial for the scattering application, while the Au nanoparticle is more favorable for energy absorption.

To further analyze the influence of the particle sizes on the absorption behavior, the absorption efficiency of Au nanospheres with radii of 80nm, 100nm, 120nm and 160nm are plotted in Figure 6.1 (b). It can be seen that as the particle radius increase, the peak wavelength is basically maintained around 520 nm, this is the natural behavior of free electron cloud inside the metal. In addition, the absorption efficiency decreases as the radius becomes larger. This is attributed to that the LSPR is essentially a surface phenomenon, and the enlargement of the radius makes less contribution to the absorption cross section. The scattering efficiency is defined as the ratio of the total absorption cross section and the area. That is, the larger radius leads to less absorption efficiency. In summary, the metal particle, especially gold, is an excellent electric dipole provider. The peak wavelength cannot be tuned directly by varying the radius, which needs to be improved.

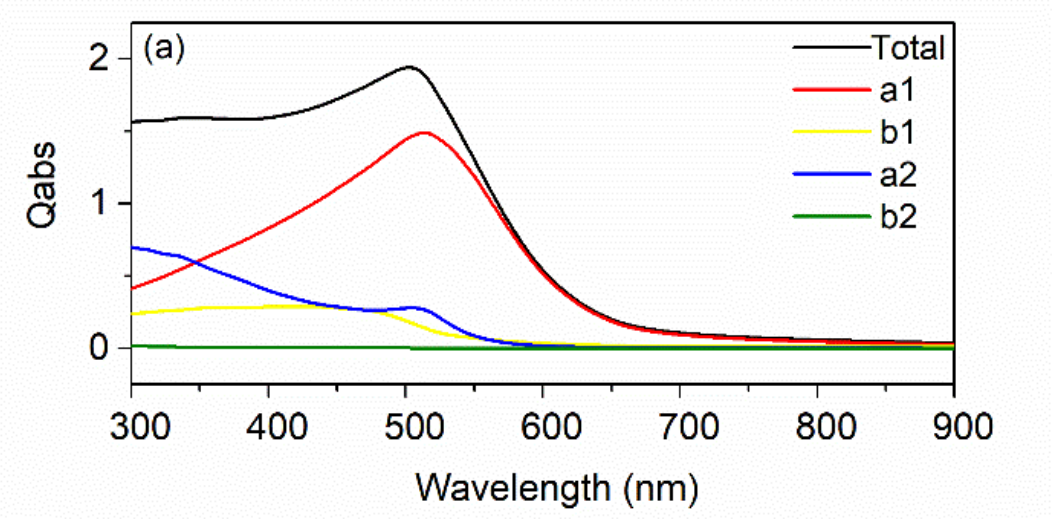

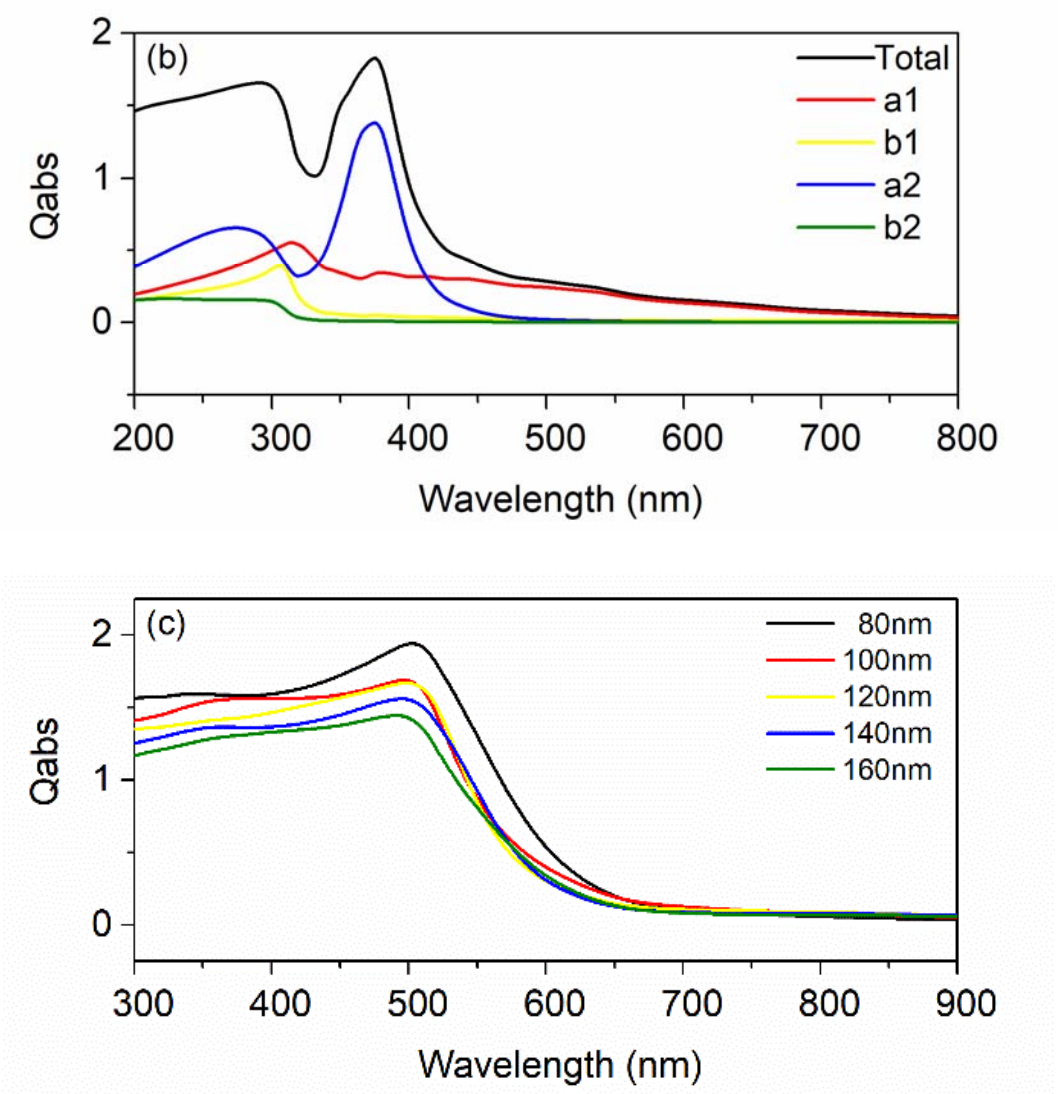

Figure 6.1: Total absorption efficiency with multiple contributions of (a) Au nanosphere and (b) Ag nanosphere. (c) Absorption efficiencies of Au nanospheres with different radii.

To shift the peak wavelength of Au nanoparticle, one commonly used approach is to coat dielectric shells, i.e. SiO_2 and TiO_2, on Au core. The absorption efficiency of Au/SiO_2 core/shell nanoparticles with different shell thickness are shown in Figure 6.2 (a). The radius of the Au core is fixed to 80nm while the SiO_2 shell thickness varies from 10nm to 50nm with 10nm as the increment. As can be seen that with the dielectric shells, the absorption peak shift to the longer wavelength. Moreover, the thicker the shell, the further the peak is moved. This behavior can be explained as follows. The wave speed inside the dielectric equals the light speed divided by the

real part of the refractive index. That is, the light is slowed down when it travels across the dielectric layer, which results in the lower oscillation frequency of the electrons cloud. Then, the absorption peak is shifted to the longer wavelength. In addition, inspection of the absorption peak efficiencies with different shell thicknesses further reveals that the thicker dielectric shell, the lower total absorption efficiency. This is due to that the dielectric material itself has no absorption, but it occupies a certain volume fraction in the core/shell structure. In a word, the dielectric shell layer can be used to tune the peak wavelength, but not help for the total absorption.

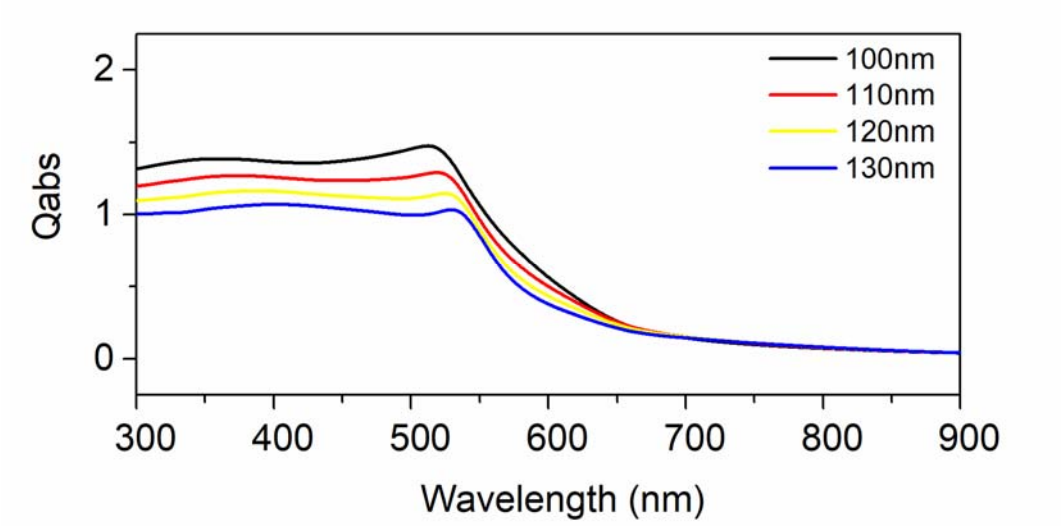

Figure 6.2: Light absorption efficiencies of Au/SiO_2 core/shell nanospheres with different SiO_2 shell radii. The Au core radius is fixed to 80nm.

In many works, the metals are utilized as the shell layer while the dielectrics being the core. Here, the SiO_2/Au core/shell nanospheres are studied to illustrate the behavior of such nanostructure. The absorption efficiencies of SiO_2/Au core/shell nanospheres with different Au shell layer radius are plotted in Figure 6.3. The radius of the SiO_2 core is maintained to 80nm while the radius of the Au shell varies from 100nm to 130nm with 10nm as the increment. The result shows that the SiO_2 core shifts the peak to the red compared to the peak of solid Au nanoparticles. That is, the light is slowed down in the dielectrics, which leads to the lower oscillation frequency

of the electrons. As the Au layer thickness increases, the peak moves back to the shorter wavelength region. This is explained that as the volume fraction of the Au material increases, the absorption behavior of the overall core/shell structure approaches to the solid Au nanoparticles. In one word, the addition of the SiO_2 core provides the peak movement to a certain degree and helps less to the absorption ability.

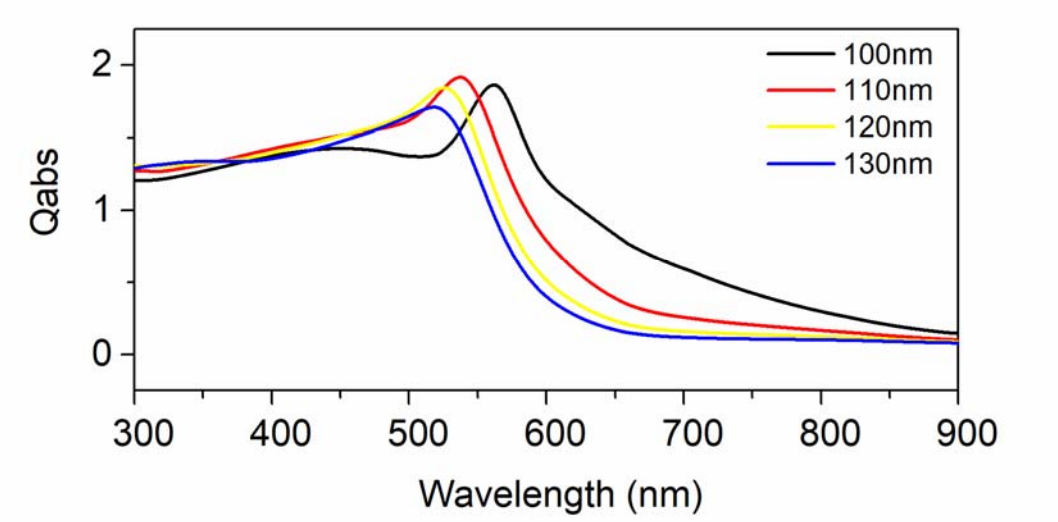

Figure 6.3: Light absorption efficiencies of SiO_2/Au core/shell nanospheres with different Au shell radii. The SiO_2 core radius is fixed to 80nm.

Semiconductor solid nanospheres and nanoshells possess both electric and magnetic dipole components for the total absorption. As an example, we calculate the total absorption with each mode component of Si nanosphere with the radius of 80nm and the result is shown in Figure 6.4 (a). The result reveals that the total absorption mainly consists of the electric and magnetic dipole components. The peak of the magnetic dipole locates at a lower frequency than that of the electric dipole, which is due to the longer distance the circulation displacement current needs to propagate during each oscillation. The contributions of electric and magnetic dipole components for different nanoparticle sizes are plotted separately in Figure 6.4 (b) and (c). As can be seen that with a larger radius, both electric and magnetic dipole peak shift to the red and with a lower absorption

efficiency. In addition, the peaks of the above two modes cannot be engineered to the same frequency in semiconductor nanospheres. That is, Si nanosphere can be utilized to provide both electric and magnetic dipole components with tunable peak wavelength. The total absorption efficiency and each component of Ge and GaAs nanoparticles with the same radius are plotted in Figure 6.4 (d) and (e), respectively. It can be seen that the Ge nanoparticle mainly provides the magnetic dipole peak at a longer wavelength. That is, the absorption behavior of the Ge nanosphere is similar to the Si nanosphere except for its lower band gap, which results in a longer peak wavelength. Figure 6.4 (e) reveals that the magnetic dipole peak of the GaAs nanoparticles is close to that of the Si nanoparticles. It worth to mention that by simply reducing the radius, the peak of the Ge nanosphere can be tuned to the shorter wavelength region, which is close to that of Si and GaAs, but with a lower magnitude of the absorption peak. That is, the Si and GaAs is more beneficial in a shorter wavelength region while the Ge nanoparticles are helpful for a longer wavelength region. Moreover, in order to absorb more light, the semiconductor nanoparticles need to be modified to overlap the electric and magnetic dipoles.

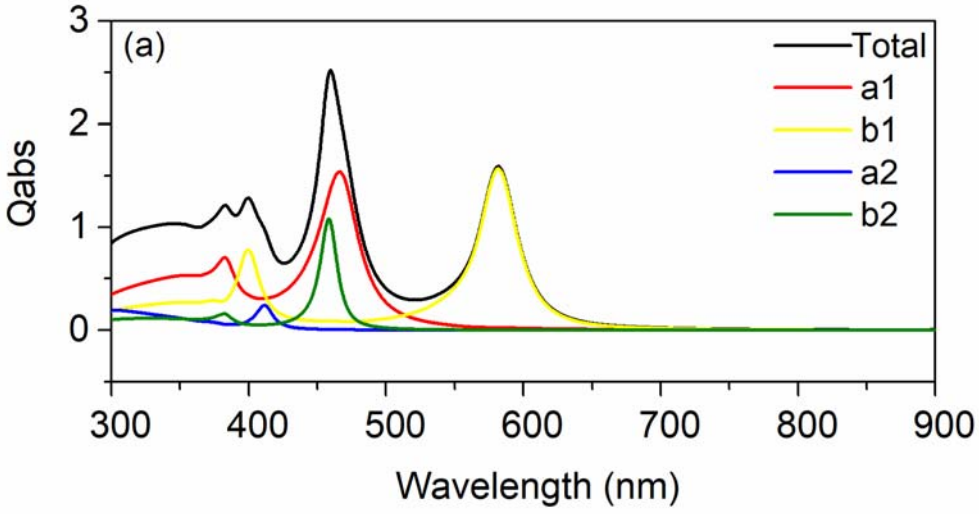

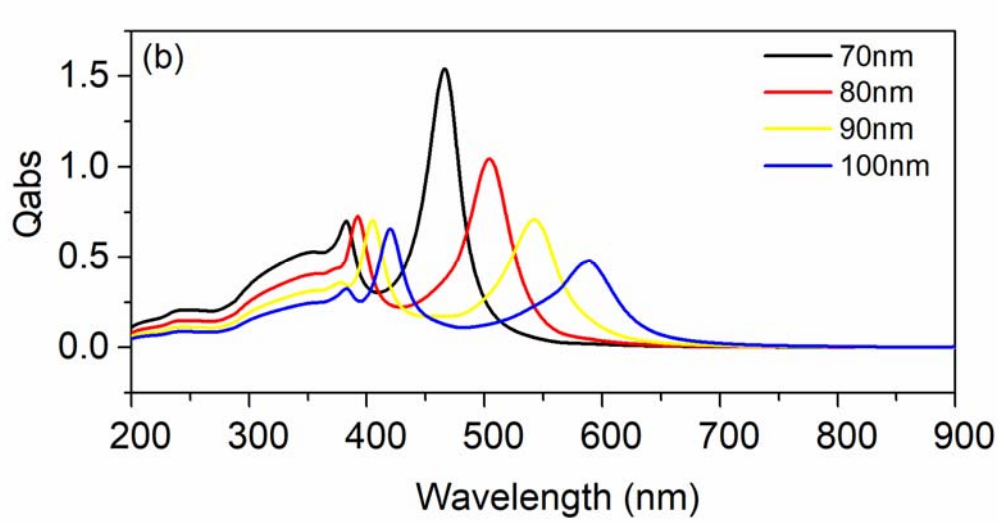
(b)
70nm
80nm
90nm
100nm
Qabs
1.5
1.0
0.5
0.0
200
300
400
500
600
700
800
900
Wavelength (nm)

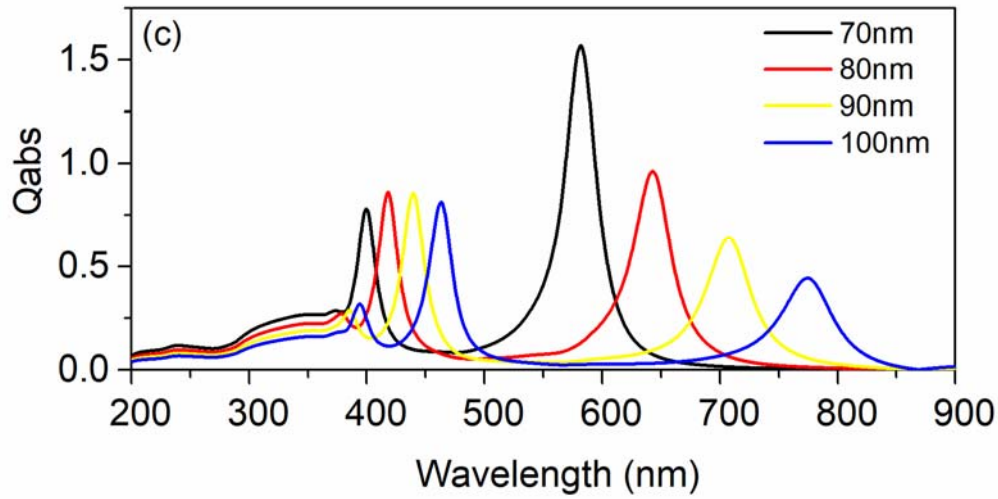
(c)
70nm
80nm
90nm
100nm
Qabs
1.5
1.0
0.5
0.0
200
300
400
500
600
700
800
900
Wavelength (nm)

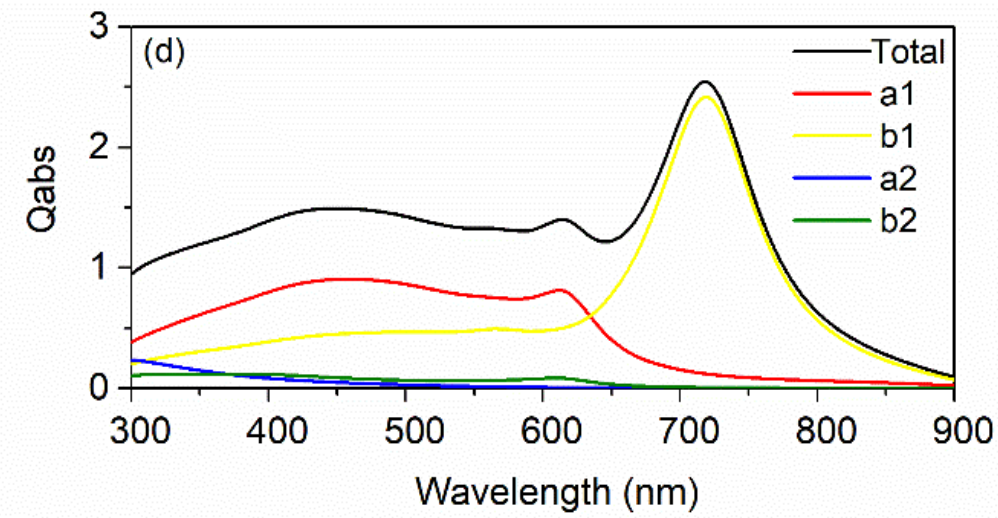
(d)
Total
a1
b1
a2
b2
Qabs
3
2
1
0
300
400
500
600
700
800
900
Wavelength (nm)

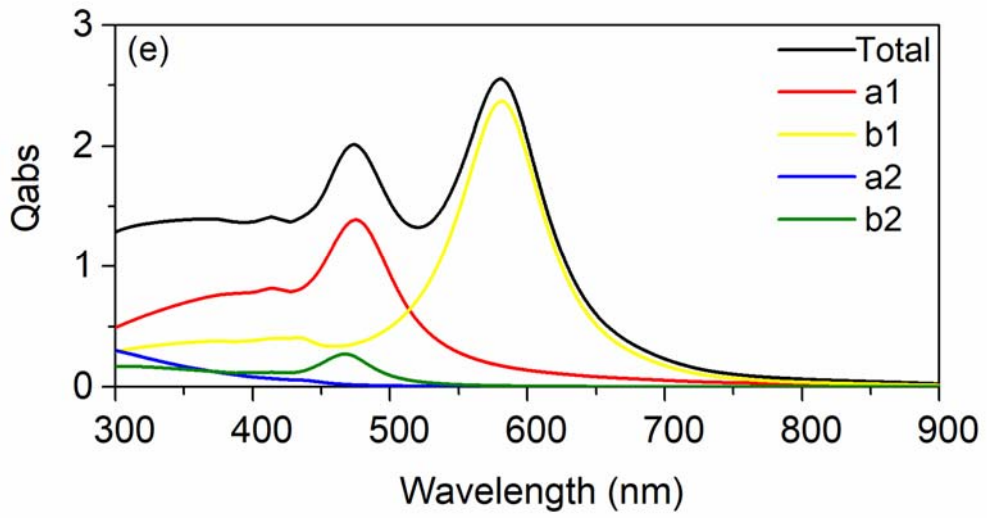

Figure 6.4: Total absorption efficiency with multiple contributions of (a) Si nanosphere, (d) Ge nanosphere and (e) GaAs nanosphere. The radius of each case is 70nm. (b) The electric dipole contribution for Si nanosphere of different radius. (c) The magnetic dipole contribution for Si nanosphere of different radius.

According to the above analysis, a generalized method to boost the absorption can be developed as coupling electric and magnetic dipole components by the metal/semiconductor core/shell nanoparticles. The metal layer provides the electric dipole while the semiconductor portion supplies both electric and magnetic dipoles. As a result, the core/shell structure possesses hybrid dipoles and can be tuned to the same wavelength by changing the thickness of each layer. Figure 6.5 (a), (b) and (c) show the total absorption efficiency and all the mode components of Au nanosphere, Si nanosphere and the designed Si/Au/Si core/shell structure with 80nm as the same outmost layer radius. The radius of each layer for the Si/Au/Si core/shell structure is 50nm, 62nm and 80nm, respectively. It can be seen that the designed core/shell structure has higher absorption efficiency, which is 3.5 at the peak, than that of both Si and Au solid nanoparticles. It is attributed to the coupling of the electric (marked as red) and magnetic (marked as yellow) dipoles.

It is worth to mention that the nanostructure developed here is superior to that with metal/dielectric nanoparticles, such as Au/SiO_2 core/shell nanospherical particle, for two reasons.

Firstly, the semiconductor material has a relatively higher refractive index, which provides the magnetic dipole mode and can be tuned to coincide with the electric dipole mode. The overlapping of the above two modes can enhance the oscillation of electrons inside the particles compared to each mode only. Secondly, unlike the lossless dielectrics, the semiconductor materials also supply excited electrons, which is beneficial to the overall absorption.

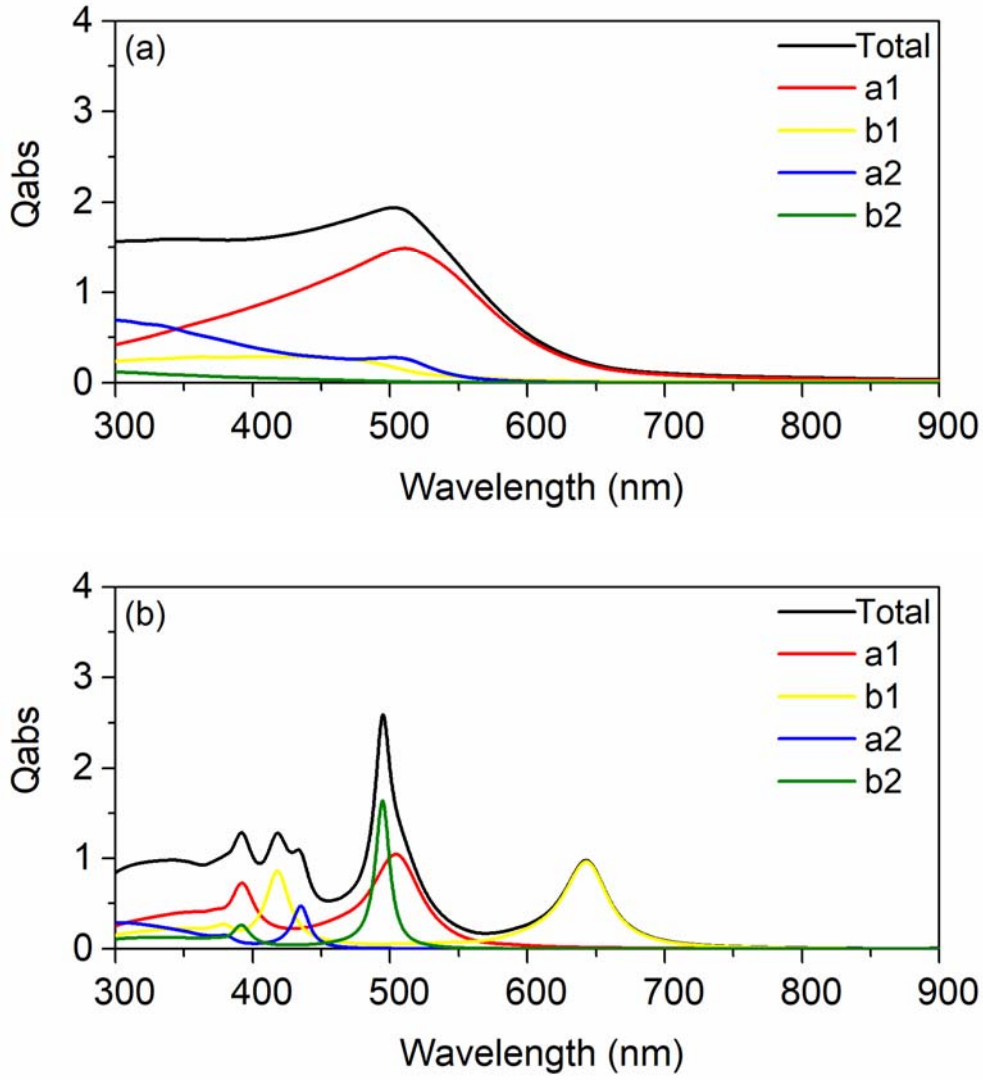

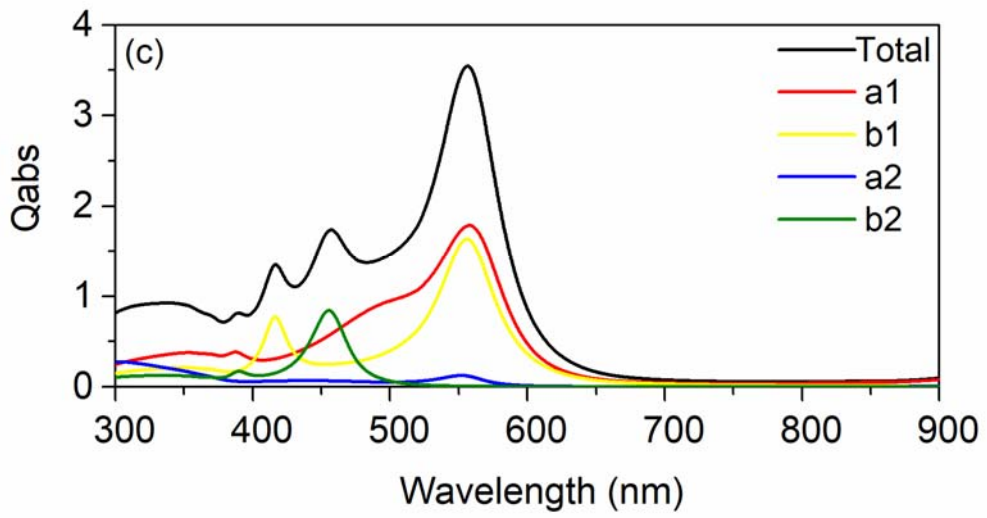

Figure 6.5: Total absorption efficiency with multiple contributions of (a) Au nanosphere and (b) Si nanosphere and (c) Si/Au/Si core/shell nanostructure.

The above result shows that the designed Si/Au/Si single core/shell nanoparticle can enhance the absorption. One question raised instinctively that whether the overlapping condition still holds for multiple nanoparticles. Thus, the light scattering efficiency along the forward direction, backward direction and the direction perpendicular to the propagation of the developed Si/Au/Si core/shell nanostructures are plotted in Figure 6.6 (a). From the result, we can see that the light is mainly scattered forwardly. That is, for the nanoparticle aggregate not aligned too close, the scattering light from a certain nanosphere will not influence the adjacent particles. Instead, the forward scattering behavior is beneficial to the next particle along the incident direction. The light scattering pattern at 560nm, which is the peak wavelength of the designed nanostructure, is shown in Figure 6.6 (b). As can be seen that the light is scattered forwardly with nearly zero backward reflection and less perpendicular components.

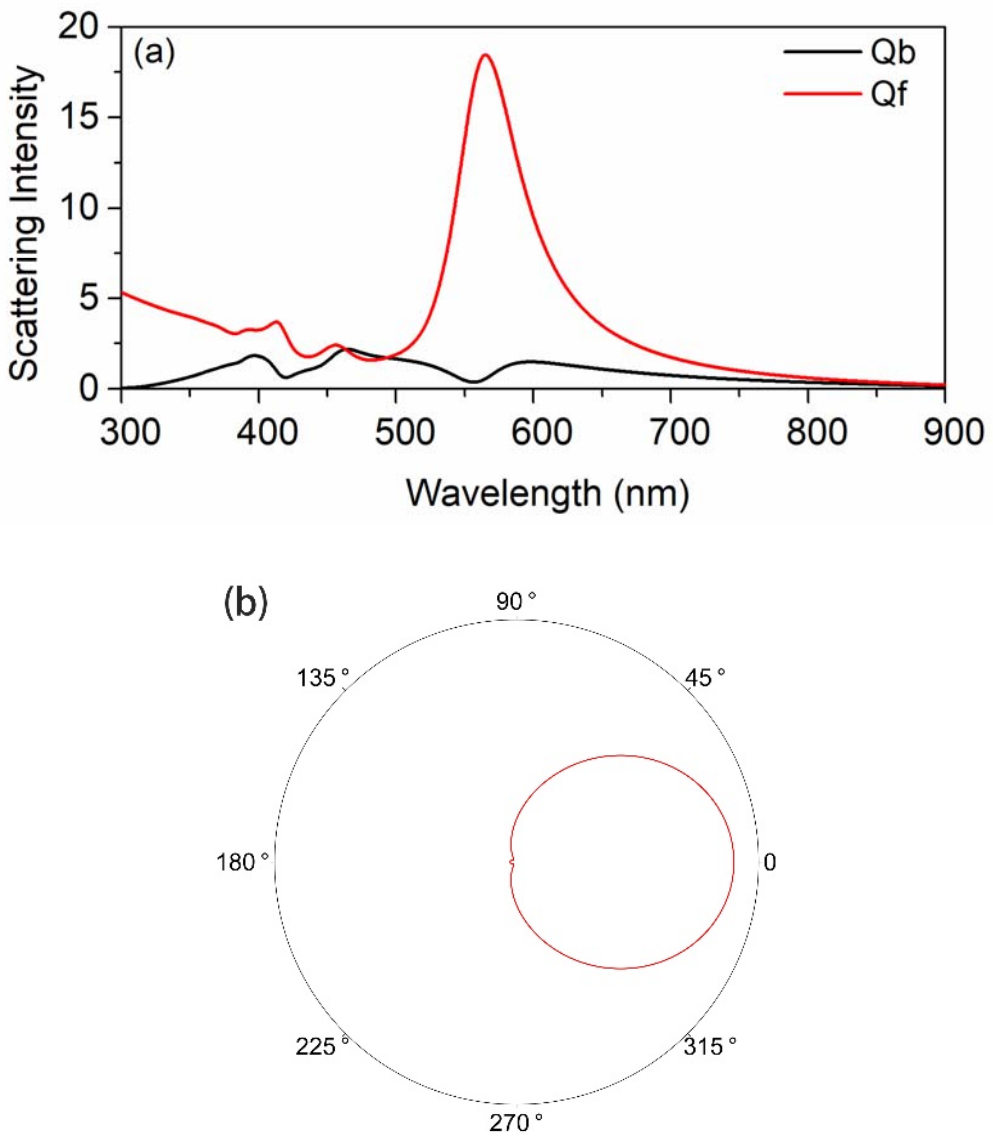

Figure 6.6: (a) Light scattering intensity along forward and backward directions for Si/Au/Si core/shell nanostructure. (b) Scattering pattern for Si/Au/Si core/shell nanostructure at 560nm wavelength.

For different applications, the coupling condition needs to be tunable for different wavelength region. Here, we show that the peak can be tuned simply by varying the radius of each layer of the Si/Au/Si structure. Figure 6.7 (a) shows the total absorption with each mode components for the Si/Au/Si core/shell structure with 55-72-100nm being the radius for each layer, respectively. From Figure 6.7 (a), it can be seen that the peaks of both electric dipole and magnetic

dipole are shifted to 650nm. However, the peak magnitude is reduced below 2, which was about 3.5 for the Si/Au/Si core/shell structure with 50-62-80nm.

As stated above, the Ge layer is more beneficial than Si in a longer wavelength. The imaginary part of the refractive index of Ge is much larger than that of Si in this region, which can provide more absorption, while the overlapping feature is maintained since the real part of the refractive indices of Ge and Si are about the same. The total absorption with each mode components for the Ge/Au/Ge core/shell structure is shown in Figure 6.7 (b). The radii of the Ge core, the Au layer and the outer Ge layer are 50nm, 63nm, and 80nm, respectively. It's obvious that both the electric and magnetic dipoles are located about 670nm and with about 3.5 as the overall absorption efficiency.

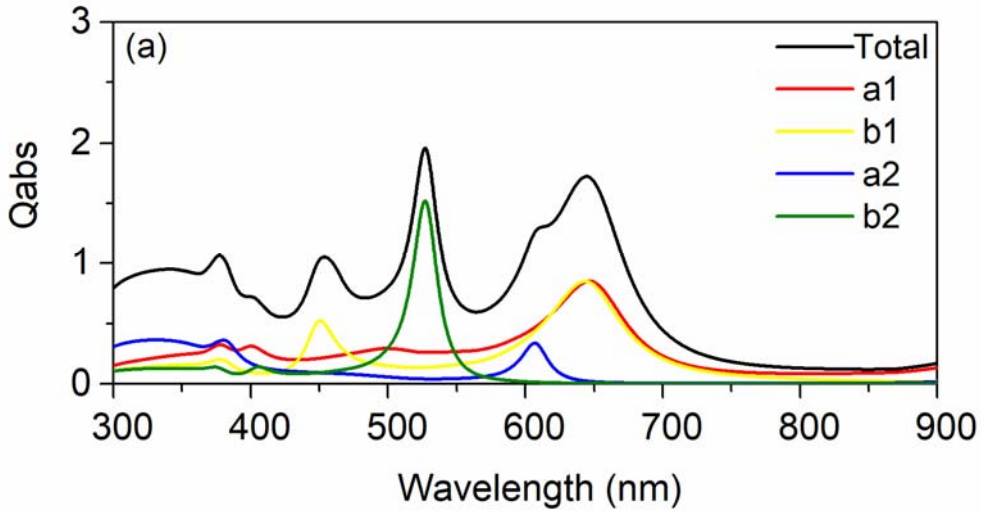

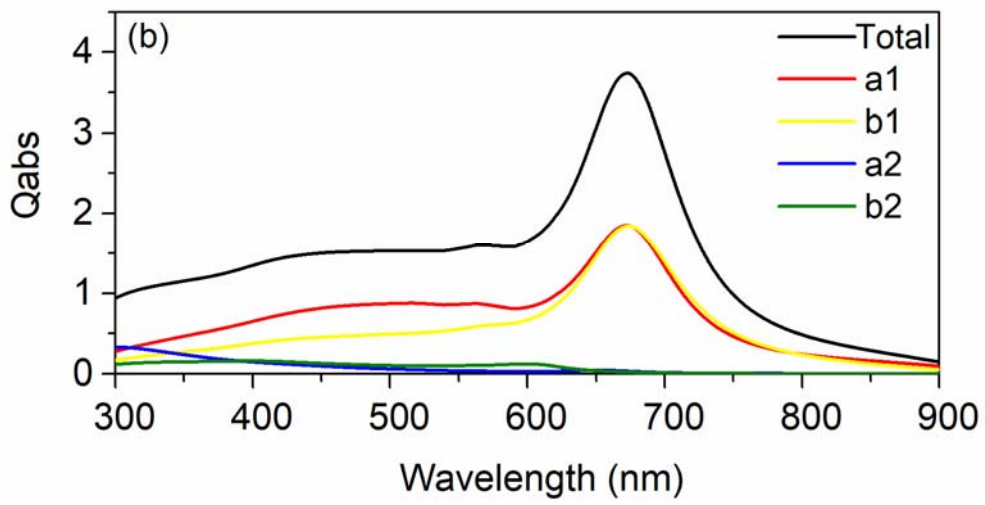

Figure 6.7: Total absorption efficiency with multiple contributions of (a) Si/Au/Si nanosphere and (b) Ge/Au/Ge nanosphere.

The absorbing nanoparticles commonly suspended in working fluid such as water and chemical medium for thermal heating usage. In this section, the coupling condition is accommodated to the water medium. The total absorption efficiency with multiple contributions of Ge/Au/Ge core/shell nanoparticle with 50nm, 62nm and 80nm as the radius of each layer are shown in Figure 6.8 (a). It can be seen that the peak wavelength of the absorption locates around 700nm with the electric and magnetic dipoles coincide. The absorption peak can also be tuned by varying the thickness of each layer. Figure 6.8 (b) shows that the peak is tuned to 650nm with 45nm, 55nm and 70nm being the radii of the Ge core, the Au shell and the Ge outer layer.

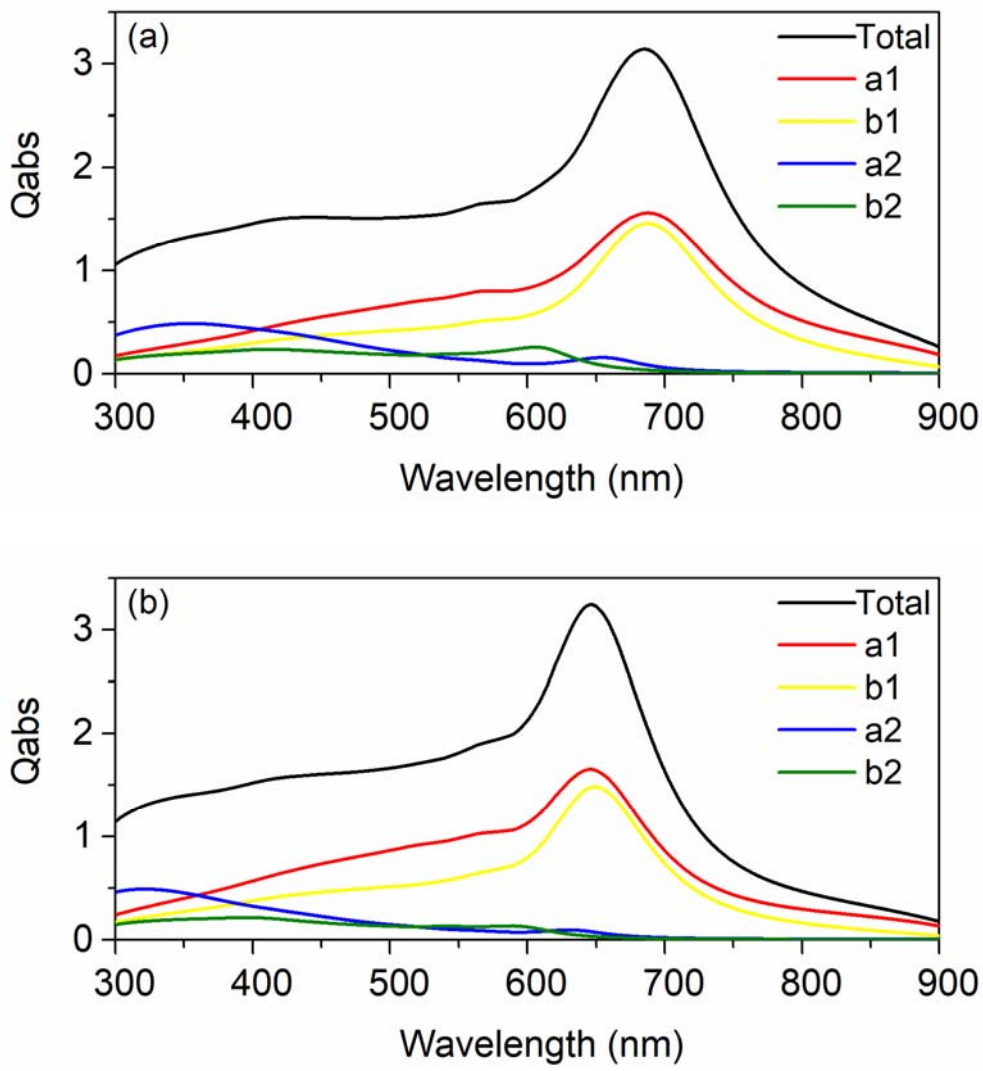

Figure 6.8: Total absorption efficiency with multiple contributions of Ge/Au/Ge core/shell nanoparticles in water with (a) 50-62-80nm and (b) 45-55-70nm being the radius of each layer.

6.3 Concluding Remarks

This part has reported a method to boost the absorption property of nanoparticles by coupling the electric and magnetic dipole components. The development of the metal-semiconductor core-shell structure is based on the Mie theory for multilayered nanoparticles. The physical origin and the optical behavior of the absorption of nanoparticles with different materials, i.e., Au, Si and Au-SiO_2 nanospheres, are discussed. The designed Si/Au/Si core-shell nanoparticle is illustrated to have better absorption than that of Au nanosphere and Si nanosphere with the same outmost radius.

Moreover, the coupling condition is proved to work for different wavelengths and different surrounding mediums. This work provides a new concept to achieve enhanced nanoparticles absorption for a various thermal application.

CHAPTER 7

Forward and Backward Light Scattering by Nanoshell Clusters

7.1 Introduction

In this chapter, we demonstrate two classes of directional light scattering nanoshell clusters, either scatters the light along the forward direction or the backward direction. That is, the designed core/shell nanoparticle cluster scatters the light mainly along forward/backward direction, while each single particle itself cannot scatter the light along that direction. Furthermore, the mechanism behind is analyzed by decomposing the total scattering efficiency into each component, i.e., the light scattered from each individual particle and the inter-particle interactions. Moreover, we present that the directional scattering feature can be tuned to different wavelength by simply changing the radii of the core/shell nanoparticles.

7.2 Method of Solution

The formula to calculate the total scattering efficiency of multiple multilayered nanoparticle cluster, which is introduced in Chapter 3, is commonly used in research. However, to explore the physical mechanism of the scattering behavior of the entire cluster, the light scattered from each single particle and the interactions between particles need to be calculated individually. In this case, another form of the total scattering efficiency is utilized [66],

$$C_{\text{sca}} = \frac{4\pi}{k^2}\sum_{n}^{\infty}\sum_{m=-n}^{n}\sum_{l}^{L}\left(\left(a_{mn}^{l}a_{mn}^{*l}+b_{mn}^{l}b_{mn}^{*l}\right)\frac{n(n+1)}{2n+1}\frac{(n+m)!}{(n-m)!}\right.$$
$$\left.+2\mathrm{Re}\sum_{\nu}^{\infty}\sum_{\mu=-\nu}^{\nu}\sum_{\lambda>l}^{L}\left[\left(a_{mn}^{l}a_{mn}^{*\lambda}+b_{mn}^{l}b_{mn}^{*\lambda}\right)C_{mn\mu\nu}+\left(b_{mn}^{l}a_{mn}^{*\lambda}+a_{mn}^{l}b_{mn}^{*\lambda}\right)D_{mn\mu\nu}\right]\right)$$

$$C_{mn\mu\nu} = \frac{(-1)^{\mu+n}}{2}\frac{(n+m)!}{(n-m)!}\sum_{p=|n-\nu|}^{n+\nu} i^{p+n+\nu} c(m,n,\mu,\nu)\, j_p(ku_{\lambda l}) P_p^{m-\mu}(\cos\theta_{\lambda l})\, \mathrm{e}^{i(m-\mu)\varphi_{\lambda l}}$$

$$c(m,n,\mu,\nu) = \left[n(n+1)+\nu(\nu+1)-p(p+1)\right]\frac{(p-m+\mu)!}{(p+m-\mu)!}a(-m,n,\mu,\nu,p)$$

$$D_{mn\mu\nu} = (-1)^{\mu+1}\sum_{p=|n-\nu|}^{n+\nu} i^{\nu-n+p}\,\frac{1-(-1)^{p+n+\nu}}{2}(2p+1)\begin{pmatrix} p & n & \nu \\ 0 & 1 & -1 \end{pmatrix}\begin{pmatrix} p & n & \nu \\ -m+\mu & m & -\mu \end{pmatrix}$$
$$\sqrt{\frac{(\nu+\mu)!}{(\nu-\mu)!}\frac{(n+m)!}{(n-m)!}\frac{(p-m+\mu)!}{(p+m-\mu)!}}\, j_p(kr) P_p^{m-\mu}(\cos\theta_{\mathrm{R}}) e^{i(m-\mu)\varphi_R} \qquad (7.1)$$

where the total scattering efficiency is divided into several categories, i.e., each electric mode contribution from individual particle, each magnetic mode contribution from individual particle, the interaction of electric modes between different particles, the interaction of magnetic modes between different particles, and the interaction of electric mode of one particle with the magnetic mode of another particle. By analyzing each scattering component, the physical origins of both forward scattering cluster and backward scattering cluster can be explained.

7.3 Results and Discussion

7.3.1 Forward Scattering Cluster

Figure 7.1 plots the forward and backward scattering intensity of a TiO_2/Si core shell nanoparticle. The radius of TiO_2 core is 30 nm, while that of the silicon outer layer is 70 nm. Result shows that the nanoshell mainly scatters light along the backward direction with a wide wavelength range from 450 nm to 580 nm. The physics behind is the combination of the electric dipole mode component with an out of phase magnetic dipole mode component, which is well known as the second Kerker's condition.

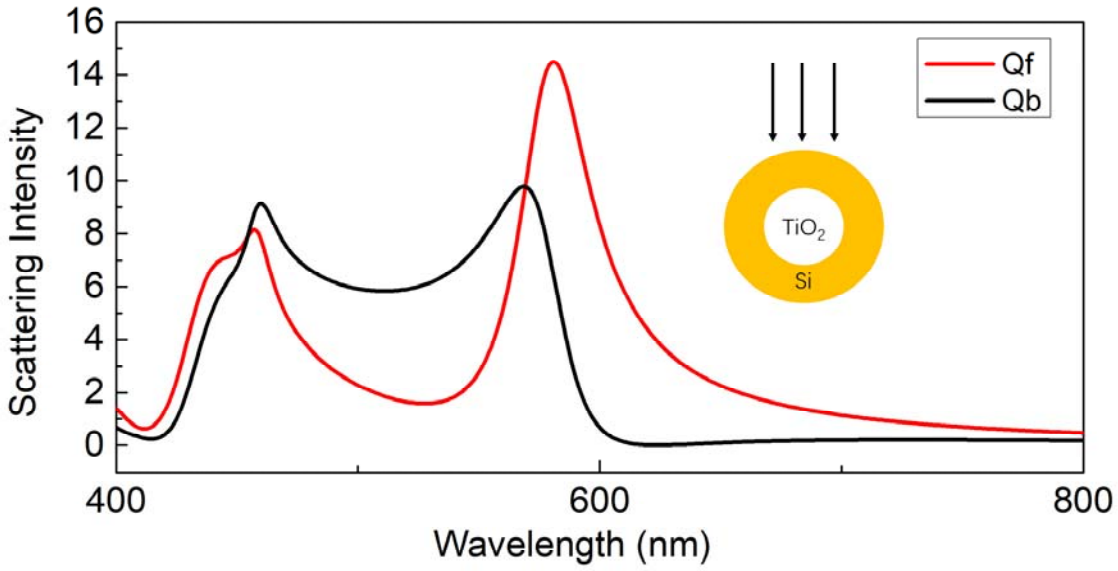

Figure 7.1: Forward (Q_f) and backward (Q_b) scattering intensity of a single TiO_2/Si core/shell nanoparticle. The TiO_2 core and silicon shell are of 30 nm radius and 40 nm thick.

For nanoparticle cluster, the scattered light is composed of not only the part from each individual particle, but also the interaction between particles, which depends on several factors, i.e., the gap between particles and the arrangement of the cluster. Thus, the scattered light can be tuned to different behavior even with the same individual nanoparticles. Figure 7.2 shows the forward and backward scattering intensity of the designed nanoshell cluster, which consists 5 TiO_2/Si core/shell nanoparticles spaced in E-H plane. The radii of TiO_2 core and Si shell of each individual particle are identical to the above backward scattering one (shown in Figure 7.1). The result shows that the designed cluster scatters the light mainly along the forward direction, which is quite different from the scattering behavior of individual particle.

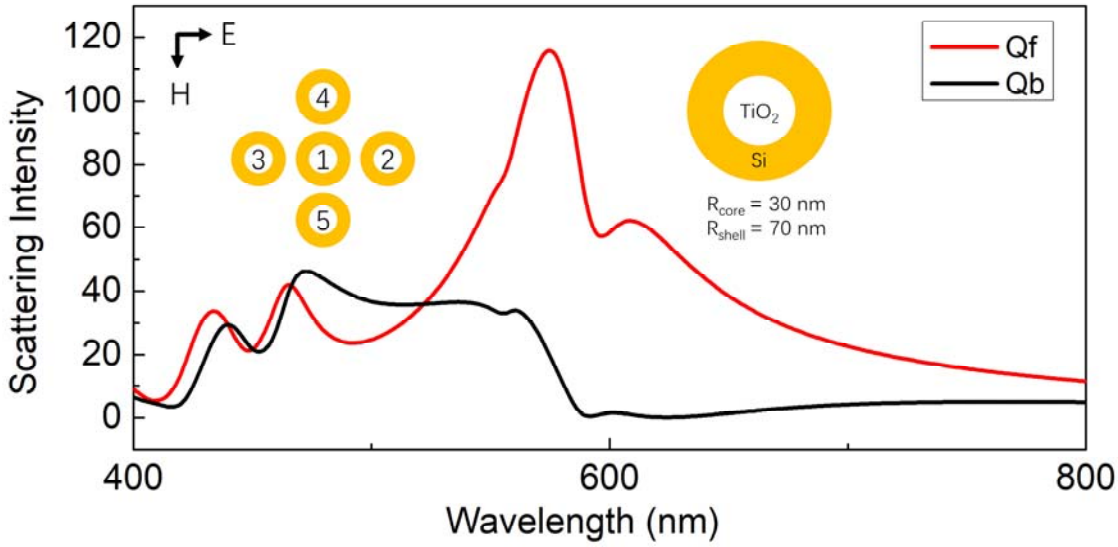

Figure 7.2: The forward (Q_f) and backward (Q_b) scattering intensity of 5 TiO_2/Si core/shell nanoparticles spaced in E-H plane. The gap between each two particles is 20 nm.

To study the physical mechanism behind this effect, the total scattering efficiency is divided into different components, which consists of the contribution from the electric (a_1) and magnetic (b_1) dipole mode of each individual particle, and the interaction of different modes between each two particles. The most relevant ones are plotted in Figure 7.3. Note that the electric and magnetic dipole modes of each particle are denoted as P_ia_1 and P_ib_1, individually, where *i* is the index of the particle. The interaction part is mainly from that between particles along the electric field direction, i.e., P_1a_1 with P_2a_1, P_1b_1 with P_2b_1 and P_2b_1 with P_3b_1. Moreover, the peak of interaction between electric dipole modes shift to longer wavelength compared to that of its individual particle. This is reasonable that each two particles along electric field direction form an effective ellipsoid, which has a longer diameter. With longer distance, the resonant frequency of the electrons is slowed, which results in the red shift of the peak. For the interactions between magnetic dipoles, the peak is not changed much, which reinforces the part of each individual particle. As a whole, the overall effective electric modes of the entire cluster are shifted towards the effective magnetic modes, which leads to the forward scattering feature.

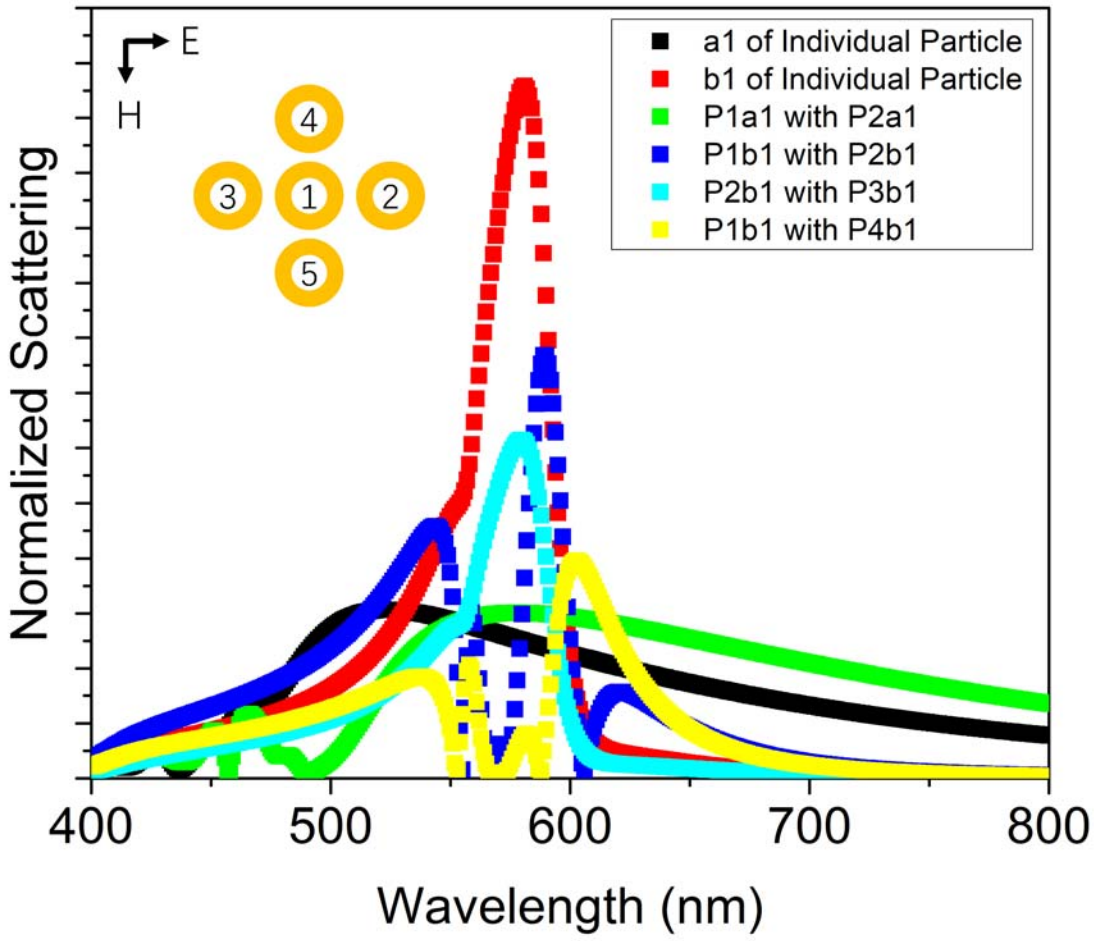

Figure 7.3: The scattering efficiency of individual electric (denoted as a_1) and magnetic (denoted as b_1) dipoles components and the relevant interparticle interactions.

Compared to the solid nanosphere, core/shell nanostructure has advantage that the peak wavelength can be tuned to different ranges. Figure 7.4 plots the forward and backward scattering intensity of 5 TiO_2/Si core/shell particles with the same arrangement. The radii of the core and the outer layer are tuned to 40nm and 90nm, respectively. It shows that the forward scattering peak is engineered to around 700 nm. Moreover, the peak wavelength is tunable with different surrounding medium by following the same procedures, which is beneficial for different light scattering applications.

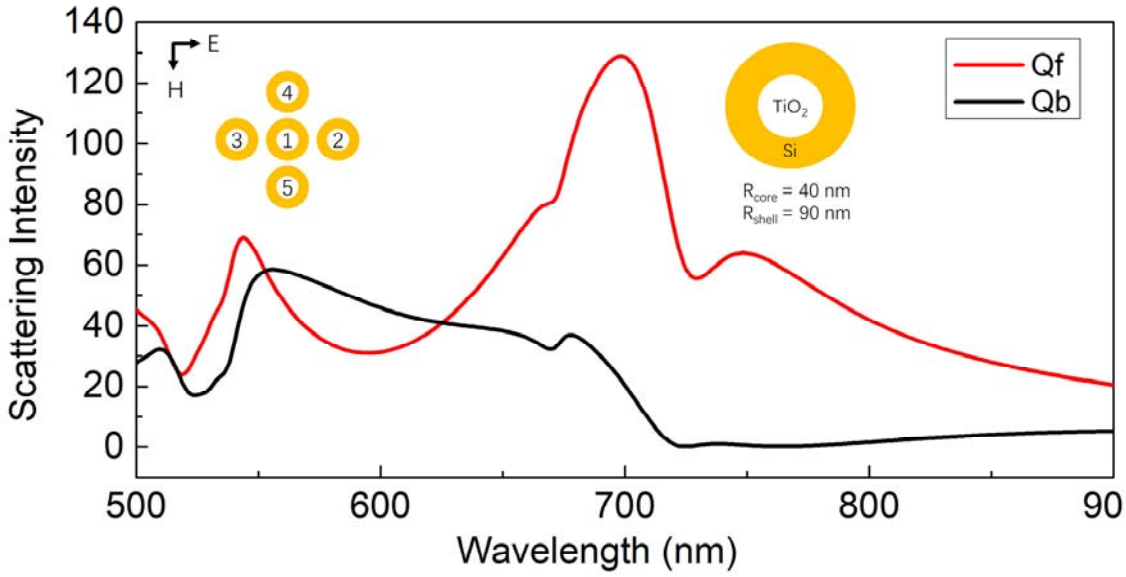

Figure 7.4: The forward (Q_f) and backward (Q_b) scattering intensity of 5 TiO_2/Si core/shell nanoparticles spaced in E-H plane. The TiO_2 core and silicon shell are tuned to 40 nm radius and 50 nm thick.

From the above analysis, it can be seen that the interactions between particles along the electric field contribute mostly than the other terms. Figure 7.5 shows the forward and backward scattering intensity of 3 TiO_2/Si core/shell nanoparticles spaced along the electric field direction. The light is mainly scattered in forward direction, which is due to the overlapping of the effective electric and magnetic dipole modes. We plot the scattering intensity of particles along magnetic field in Figure 7.6. The cluster scatters the light along backward direction. The reason is the peaks of the electric and magnetic dipole modes are separated. Finally, we analyze the case where 5 particles are aligned along the electric field, as plotted in Figure 7.7. The forward scattering intensity reaches 150, which is much larger than the case that 5 particles in E-H plane (see Figure 7.4).

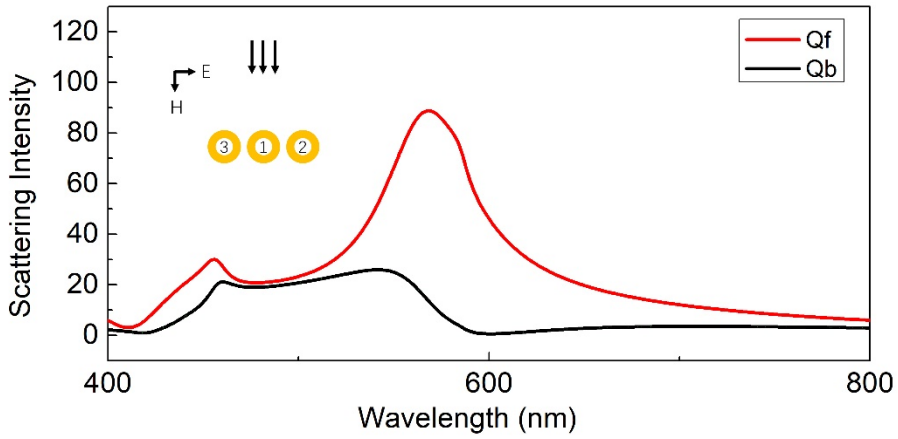

Figure 7.5: The forward (Q_f) and backward (Q_b) scattering intensity of 3 TiO_2/Si core/shell nanoparticles spaced along electric field direction.

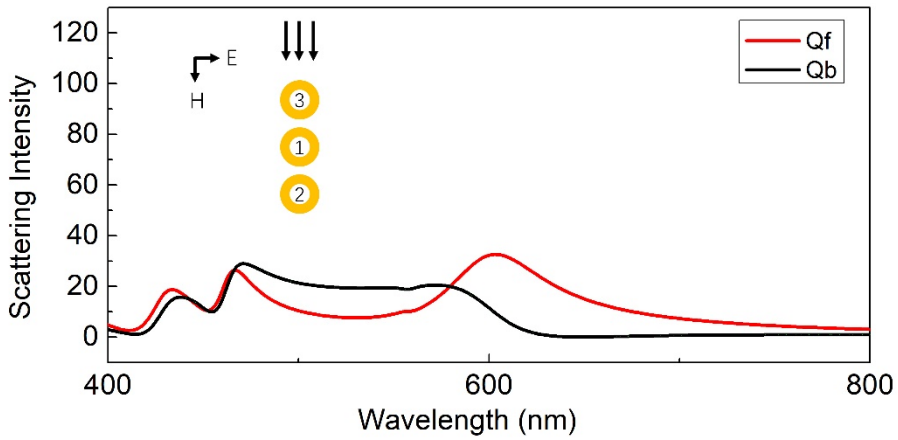

Figure 7.6: The forward (Q_f) and backward (Q_b) scattering intensity of 3 TiO_2/Si core/shell nanoparticles spaced along magnetic field direction.

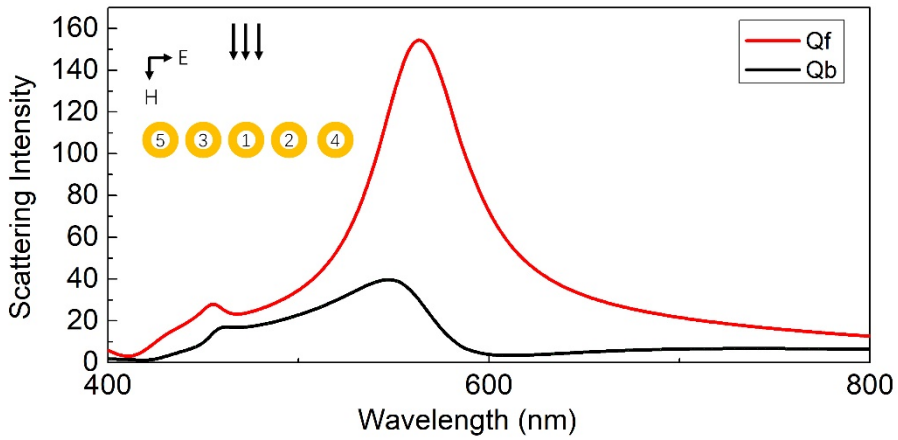

Figure 7.7: The forward (Q_f) and backward (Q_b) scattering intensity of 5 TiO_2/Si core/shell nanoparticles spaced along electric field direction.

7.3.2 Backward Scattering Cluster

In this section, we show that the backward scattering nanoparticles cluster can be obtained with individual non-backward scattering particle. To start with, we check the scattering intensity of a single Ag nanoshell, which is plotted in Figure 7.8. The inner and outer radii of 45 nm and 60 nm, respectively. It can be seen that the amounts of light scattered along forward and backward directions are basically identical, which is the behavior of electric dipole mode. Note that for metal shell, i.e., Ag nanoshell and Au nanoshell, the scattered light is mainly from the electric dipole mode.

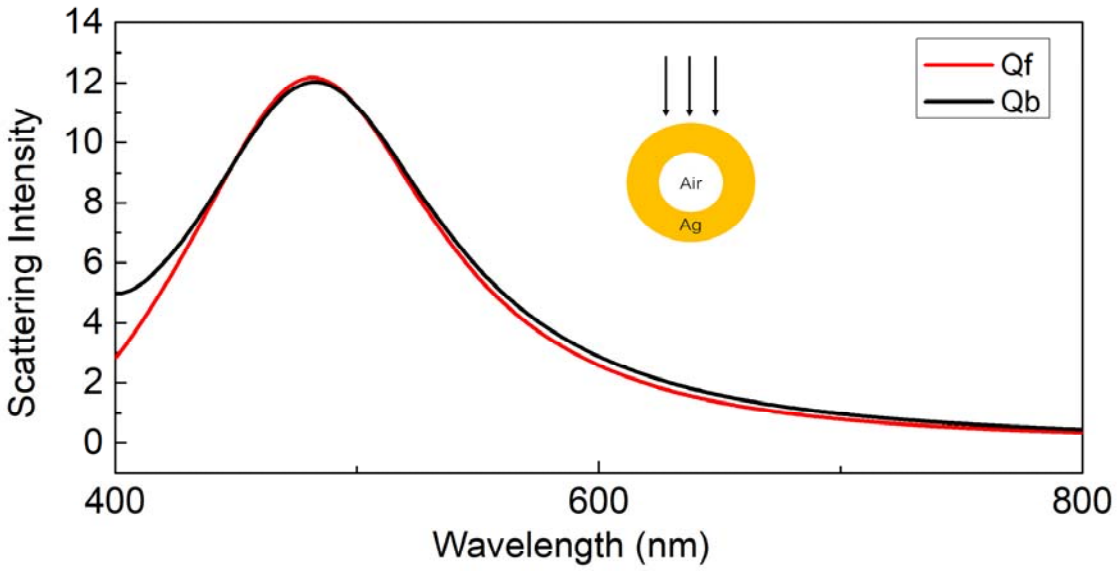

Figure 7.8: Forward (Q_f) and backward (Q_b) scattering intensity of a single Ag nanoshell. The air core and silver shell are of 45 nm radius and 15 nm thick.

As particles are assembled into cluster, i.e, 5 particles in H-k plane shown in Figure 7.9, the scattering behavior is changed. It can be seen that the light scattered by the overall cluster is mainly along the backward direction in such arrangement. To investigate the physical mechanism of this effect, the total scattering efficiency is divided into the contributions from individual particle and the interactions between particles. Figure 7.10 plots the scattering efficiency of

individual particle and relevant interaction components. It is seen that the interparticle effects between particles along the k direction contributes most to the overall scattered light.

To inspect the interaction between particles along the propagation direction, each nanoshell can be treated as a dipole source. It is known that the total radiation intensity from two electric dipole sources can be expressed as $I = 4I_0 cos^2(\pi \frac{d}{\lambda} cos\Theta + \frac{\delta}{2})$, where I_0, d and δ are the intensity of the source, the distance between two sources, and the phase difference between the two sources. Θ represents the angle that the observation point in far-field deviated from the k direction. In this case, light strikes particles along the propagation direction consequently, which results in that the phase difference δ between two particles (equivalent dipole sources) is related to the distance d between the center of each particle as $\delta = 2\pi \frac{d}{\lambda}$. By setting Θ to either 0 or π, the light intensities along forward or backward direction can be obtained. With simple algebraic manipulation, the ratio of the forward to backward scattering intensity can be expressed as $\frac{Qf}{Qb} = cos^2(2\pi \frac{d}{\lambda})$. The value of the ratio oscillates between 0 and 1 as the distance d increases. That is, the overall forward scattering intensity is always smaller or equal to that along backward direction. Moreover, the forward to backward scattering ratio is minimized when the distance is odd times of quarter-wavelength, i.e., 1/4 λ, 3/4 λ, 5/4 λ etc. In this case, the distance between each two Ag shell equals to the summation of the gap and twice of its outmost layer radius, which is 130 nm. As shown in Figure 7.9, the light scattered along backward direction is maximized around 520 nm.

In addition, the backward scattering feature can be tuned to different wavelength by simply changing the inner and outer radii of the Ag nanoshell as shown in Figure 7.11.

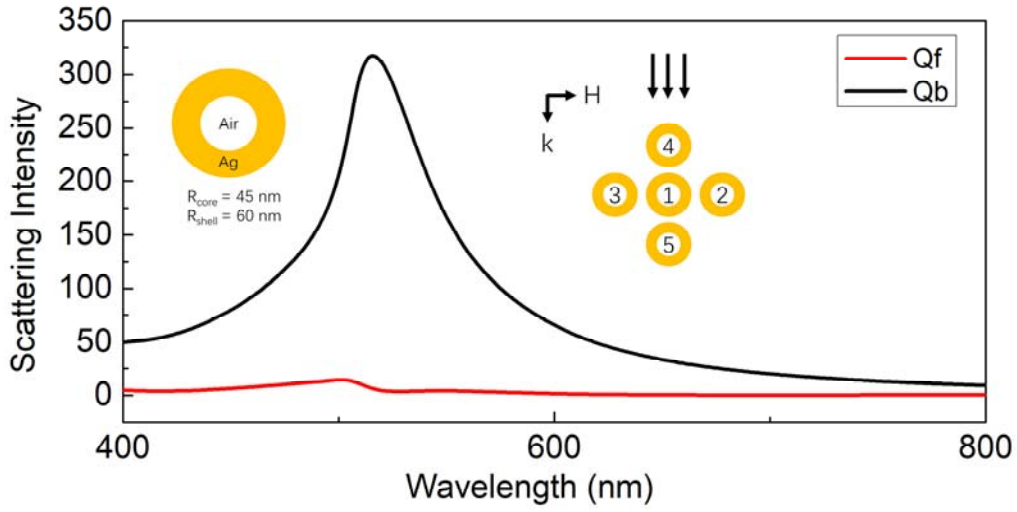

Figure 7.9: Forward (Q_f) and backward (Q_b) scattering intensity of 5 Air-Ag core/shell nanoparticles spaced in E-H plane. The gap between each two particles is 10 nm.

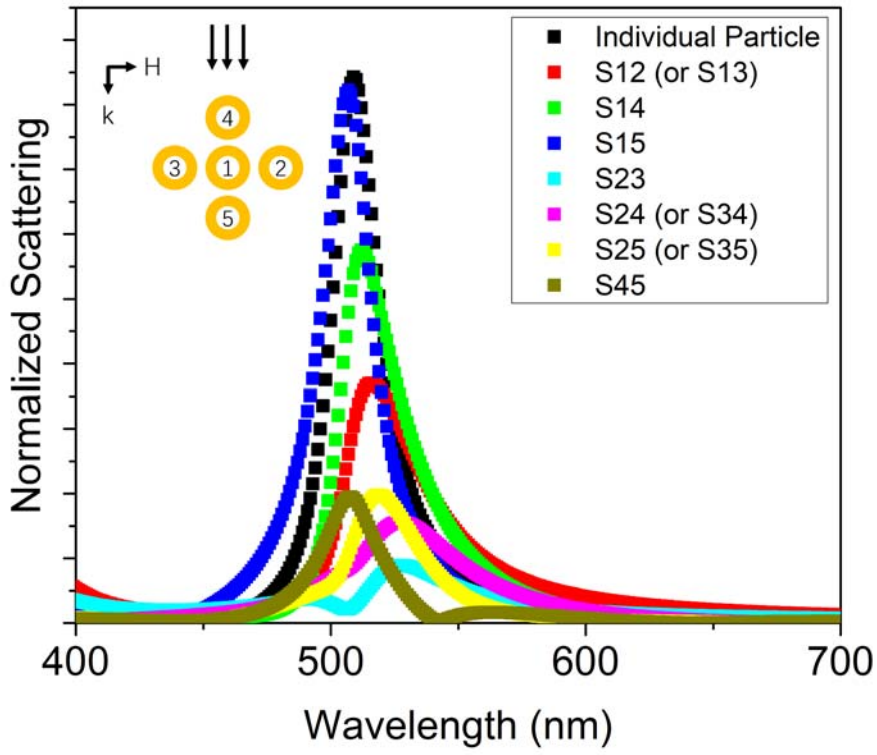

Figure 7.10: Scattering efficiency of individual electric dipole mode and the relevant inter-particle electric dipole mode interactions. Each interaction is denoted as S_{ij}, where i and j represent the index of the particles, respectively.

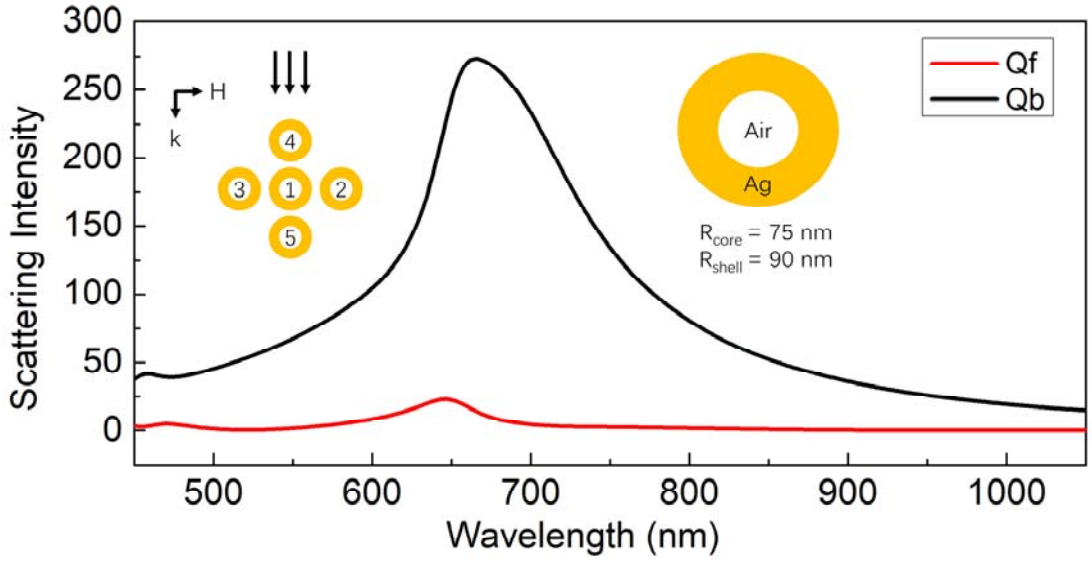

Figure 7.11: The forward (Q_f) and backward (Q_b) scattering intensity of 5 Air-Ag core/shell nanoparticles spaced in E-H plane. The air core and silver shell are of 75 nm radius and 15 nm thick.

As the interactions between particles along the wave propagation direction contribute mostly for the backward scattering feature of the entire cluster, 3 and 5 particles aligned along k direction are investigated and plotted in Figure 7.12 and Figure 7.13, respectively. Figure 7.12 reveals that 3 particles along the k direction can scatter the light as much as that of 5 particles spaced in H-k plane. With 5 particles along k direction, as shown in Figure 7.13, the backward scattering intensity is further enhanced.

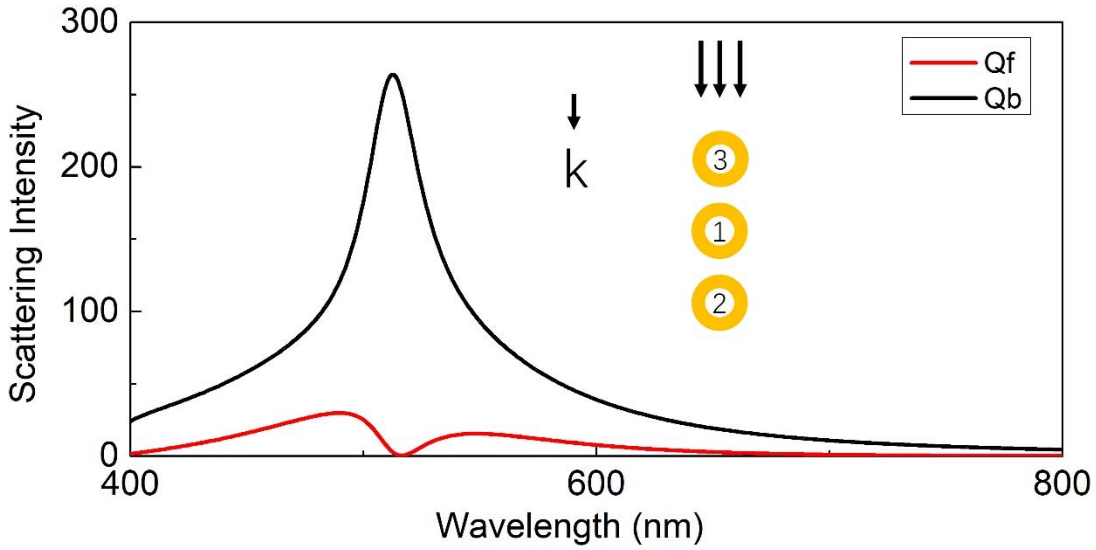

Figure 7.12: The forward (Q_f) and backward (Q_b) scattering intensity of 3 Air-Ag core/shell nanoparticles spaced along k direction.

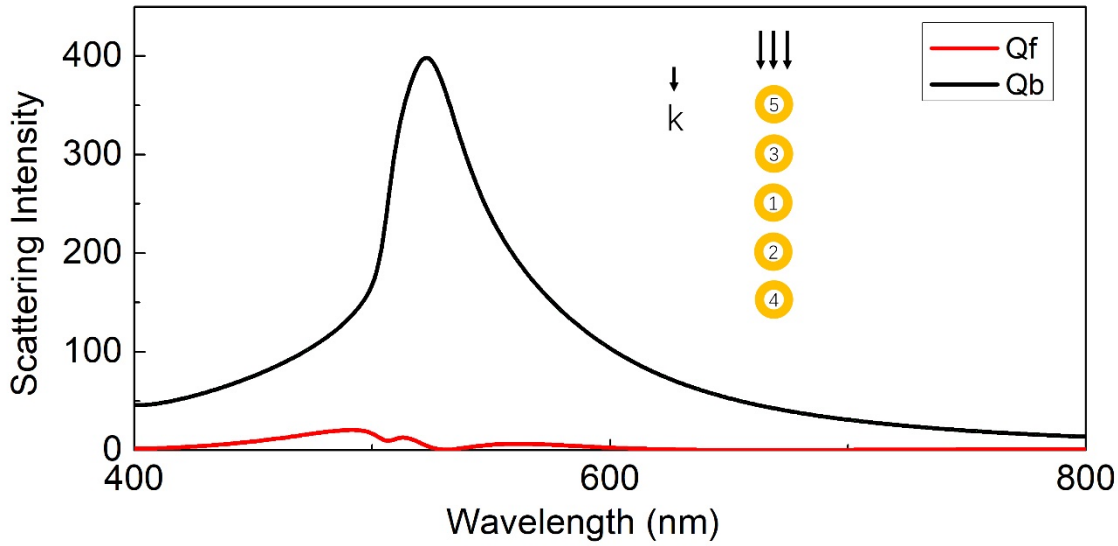

Figure 7.13: The forward (Q_f) and backward (Q_b) scattering intensity of 5 Air-Ag core/shell nanoparticles spaced along k direction.

7.4 Concluding Remarks

This section introduces two types of light scattering nanoparticles aggregates. One type is the forward scattering nanoshell cluster. The entire configuration as a whole, scatters light forwardly, while each single nanoshell is non-forward scatter. The mechanism is discussed by analyzing the

inter-particle interactions. The particles along electric field direction is found to shift the overall effective electric dipole mode toward the magnetic dipole part, resulting the forward scattering feature. The other type is the backward scattering nanoparticle cluster. It's found that the inter-particle interaction between particles along the light propagation direction contributes to the backward scattering feature. That is, the distance induced response phase lag between particles results in the backward scattering of the entire cluster. Finally, both forward and backward scattering feature of the clusters can be tuned for different wavelength range for specific applications.

CHAPTER 8

Conclusion

In this research, core/shell nanoparticle or nanoparticle cluster is designed to scatter light, either along forward or backward direction, or possess excellent light absorbing ability. The design and calculation are based on the Mie theory with the addition-theorem recursive algorithm for electromagnetic scattering particles.

Firstly, by tuning parameters of the particle, i.e., radius and refractive index of each layer, the electric and magnetic modes are overlapped, resulting the forward scattering feature. Dielectric nanoparticles with an appropriate surrounding medium are proved to scatters light forwardly in broaden band without heat loss. Through numerical simulation, significant light absorption enhancement in thin film solar cell is observed with the designed nanoparticles partially embedded atop active layer.

Second, we demonstrate the light absorption of nanoparticle can be enhanced by overlapping the electric and magnetic mode components of the total absorption. We also show the designed principle works for different wavelengths and surrounding mediums.

Finally, we presents nanoshell clusters with either forward or backward scattering ability, which is not possessed by its single nanoshell. The total scattering efficiency is divided into the individual scattering components and inter-particle interactions. We find that the forward scattering characteristic of the cluster comes from the interactions between particles along electric field, while the backward scattering feature is mainly the result of the interactions between particles along the light propagation direction.

BIBLIOGRAPHY

[1] P. K. Nayak, S. Mahesh, H. J. Snaith, and D. Cahen, "Photovoltaic solar cell technologies: analysing the state of the art," Nat. Rev. Mater. (2019).

[2] Y. Tian and C. Y. Zhao, "A review of solar collectors and thermal energy storage in solar thermal applications," Appl. Energy **104**, 538–553 (2013).

[3] A. O. Id, D. Zanardo, E. Ghedini, and F. Menegazzo, "Solar Fuels by Heterogeneous Photocatalysis : From Understanding Chemical Bases to Process Development," (x), (2018).

[4] T. D. Lee and A. U. Ebong, "A review of thin film solar cell technologies and challenges," Renew. Sustain. Energy Rev. **70**, 1286–1297 (2017).

[5] H. Sai, K. Saito, N. Hozuki, and M. Kondo, "Relationship between the cell thickness and the optimum period of textured back reflectors in thin-film microcrystalline silicon solar cells," Appl. Phys. Lett. **102**, 3–7 (2013).

[6] H. Sai, T. Matsui, T. Koida, K. Matsubara, M. Kondo, S. Sugiyama, H. Katayama, Y. Takeuchi, and I. Yoshida, "Triple-junction thin-film silicon solar cell fabricated on periodically textured substrate with a stabilized efficiency of 13.6%," Appl. Phys. Lett. **106**, 2–6 (2015).

[7] H. Sai, T. Matsui, and K. Matsubara, "Stabilized 14.0%-efficient triple-junction thin-film silicon solar cell," Appl. Phys. Lett. **109**, 2–6 (2016).

[8] V. E. Ferry, M. A. Verschuuren, M. C. van Lare, R. E. I. Schropp, H. A. Atwater, and A. Polman, "Optimized Spatial Correlations for Broadband Light Trapping," Nano Lett. **11**, 4239–4245 (2011).

[9] M. G. Deceglie, V. E. Ferry, A. P. Alivisatos, and H. A. Atwater, "Design of nanostructured solar cells using coupled optical and electrical modeling," Nano Lett. **12**, 2894–2900 (2012).

[10] P. Pathi, A. Peer, and R. Biswas, "Nano-Photonic Structures for Light Trapping in Ultra-Thin Crystalline Silicon Solar Cells," Nanomaterials **7**, 17 (2017).

[11] S. M. Kang, S. Jang, J. K. Lee, J. Yoon, D. E. Yoo, J. W. Lee, M. Choi, and N. G. Park, "Moth-Eye TiO2 Layer for Improving Light Harvesting Efficiency in Perovskite Solar Cells," Small **12**, 2443–2449 (2016).

[12] X. Liu, Y. Da, and Y. Xuan, "Full-spectrum light management by pseudo-disordered moth-eye structures for thin film solar cells," Opt. Express **25**, A824 (2017).

[13] W. Qarony, M. I. Hossain, R. Dewan, S. Fischer, V. B. Meyer-Rochow, A. Salleo, D. Knipp, and Y. H. Tsang, "Approaching Perfect Light Incoupling in Perovskite and Silicon Thin Film Solar Cells by Moth Eye Surface Textures," Adv. Theory Simulations **1800030**, 1800030 (2018).

[14] S. Mokkapati, F. J. Beck, A. Polman, and K. R. Catchpole, "Designing periodic arrays of metal nanoparticles for light-trapping applications in solar cells," Appl. Phys. Lett. **95**, 1–3 (2009).

[15] P. Spinelli, M. Hebbink, R. De Waele, L. Black, F. Lenzmann, and A. Polman, "Optical impedance matching using coupled plasmonic nanoparticle arrays," Nano Lett. **11**, 1760–1765 (2011).

[16] L. Van Dijk, J. Van De Groep, L. W. Veldhuizen, M. Di Vece, A. Polman, and R. E. I. Schropp, "Plasmonic Scattering Back Reflector for Light Trapping in Flat Nano-Crystalline Silicon Solar Cells," ACS Photonics **3**, 685–691 (2016).

[17] Y. Kim, N. D. Lam, K. Kim, W. K. Park, and J. Lee, "Ge nanopillar solar cells epitaxially grown by metalorganic chemical vapor deposition," Sci. Rep. **7**, 1–9 (2017).

[18] W. Wang, S. Wu, K. Reinhardt, Y. Lu, and S. Chen, "Broadband light absorption enhancement in thin-film silicon solar cells," Nano Lett. **10**, 2012–2018 (2010).

[19] Y. Shang, S. Hao, C. Yang, and G. Chen, "Enhancing Solar Cell Efficiency Using Photon Upconversion Materials," Nanomaterials **5**, 1782–1809 (2015).

[20] W. Ye, R. Long, H. Huang, and Y. Xiong, "Journal of Materials Chemistry C Accepted Manuscript Journal of Materials Chemistry C Accepted Manuscript," 1–3 (2016).

[21] H. Malekzad, P. S. Zangabad, H. Mirshekari, M. Karimi, and M. R. Hamblin, "Noble metal nanoparticles in biosensors : recent studies and applications," **6**(3), 301–329 (2017).

[22] P. D. Howes, R. Chandrawati, and M. M. Stevens, "biological sensors," **346**(6205), (2014).

[23] H. H. Nguyen, J. Park, S. Kang, and M. Kim, "Surface Plasmon Resonance: A Versatile Technique for Biosensor Applications," 10481–10510 (2015).

[24] C. Hou, S. Hou, Y. Hsueh, J. Lin, H. Wu, and F. Lin, "Biomaterials The in vivo performance of biomagnetic hydroxyapatite nanoparticles in cancer hyperthermia therapy," Biomaterials **30**(23–24), 3956–3960 (2009).

[25] N. S. Abadeer and C. J. Murphy, "Recent Progress in Cancer Thermal Therapy Using Gold Nanoparticles," (2016).

[26] R. Das, J. Alonso, Z. Amghouz, E. Garaio, P. Gorria, J. A. Blanco, M. H. Phan, and H. Srikanth, "Boosted Hyperthermia Therapy by Combined AC Magnetic and Photothermal Exposures in Ag/Fe 3 O 4 Nano fl owers," (2016).

[27] M. Valenti, M. P. Jonsson, G. Biskos, A. Schmidt-ott, and W. A. Smith, "Plasmonic nanoparticle-semiconductor composites for efficient solar water splitting," J. Mater. Chem. A Mater. energy Sustain. **4**, 17891–17912 (2016).

[28] P. Zhang, T. Wang, and J. Gong, "Mechanistic Understanding of the Plasmonic Enhancement for Solar Water Splitting," 5328–5342 (2015).

[29] F. Papers, "Bimetallic and Plasmonic Ag–Au on TiO 2 for Solar Water Splitting: An Active Nanocomposite for Entire Visible- Light-Region Absorption," 1–9 (2016).

[30] L. Zhou, Y. Tan, J. Wang, W. Xu, Y. Yuan, W. Cai, and S. Zhu, "3D self-assembly of aluminium nanoparticles for plasmon-enhanced solar desalination," Nat. Photonics **10**(6), 393–398 (2016).

[31] M. Shang, N. Li, S. Zhang, T. Zhao, C. Zhang, C. Liu, H. Li, and Z. Wang, "Full-Spectrum Solar-to-Heat Conversion Membrane with Interfacial Plasmonic Heating Ability for High-Efficiency Desalination of Seawater," (2018).

[32] L. Zhang, J. Xing, X. Wen, J. Chai, S. Wang, and Q. Xiong, "Plasmonic heating from indium nanoparticles on a fl oating microporous membrane for enhanced solar seawater desalination †," 12843–12849 (2017).

[33] G. L. Liu, J. Kim, Y. U. Lu, and L. P. Lee, "Optofluidic control using photothermal nanoparticles," 27–32 (2005).

[34] J. Chen, Z. Kang, G. Wang, F. Chuen, and S. Kai, "Lab on a Chip Accepted Manuscript Lab on a Chip Accepted Manuscript," 1–3 (2015).

[35] F. Winterer, C. M. Maier, and T. Lohmu, "Soft Matter Optofluidic transport and manipulation of plasmonic nanoparticles by thermocapillary convection †," 628–634 (2018).

[36] J. Kim, M. D. Kumar, J. Yun, H. Park, E. Lee, D. Kim, H. Kim, M. Kim, J. Yi, H. Kim, C. Jeong, J. Kim, D. Kumar, J. Yun, and H. Park, "Transparent conductor-embedding

nanolens for Si solar cells Transparent conductor-embedding nanolens for Si solar cells," **151904**, (2015).

[37] J. A. Lloyd, S. H. Ng, A. C. Y. Liu, Y. Zhu, W. Chao, T. Coenen, J. Etheridge, and D. E. Go, "Plasmonic Nanolenses : Electrostatic Self-," (2017).

[38] R. Liang, J. Dai, L. Xu, J. He, S. Wang, Y. Peng, and H. Wang, "High Light Extraction Efficiency of Deep Ultraviolet LEDs Enhanced Using Nanolens Arrays," 1–6 (2018).

[39] R. Sun, K. Peng, B. Hu, Y. Hu, F. Zhang, S. Lee, R. Sun, K. Peng, B. Hu, Y. Hu, F. Zhang, and S. Lee, "Plasmon enhanced broadband optical absorption in ultrathin silicon nanobowl array for photoactive devices applications Plasmon enhanced broadband optical absorption in ultrathin silicon nanobowl array for photoactive devices applications," **013107**, (2015).

[40] Z. Yang, X. Li, S. Wu, P. Gao, and J. Ye, "High-efficiency photon capturing in ultrathin silicon solar cells with front nanobowl texture and truncated-nanopyramid reflector," **40**(6), 1077–1080 (2015).

[41] V. A. Online, H. Wei, J. Huang, C. Hsu, F. Chang, K. Ho, and C. Chu, "Environmental Science," 1192–1198 (2013).

[42] P. Liu, S. Yang, Y. Ma, X. Lu, Y. Jia, D. Ding, and Y. Chen, "Materials Science in Semiconductor Processing Design of Ag nanograting for broadband absorption enhancement in amorphous silicon thin fi lm solar cells," Mater. Sci. Semicond. Process. **39**, 760–763 (2015).

[43] C. L. Tan, A. Karar, K. Alameh, and Y. T. Lee, "Optical absorption enhancement of hybrid- photodetector incorporating metal nanogratings and embedded metal nanoparticles," **21**(2), 1763–1767 (2013).

[44] A. L. Fannin, B. R. Wenner, J. W. Allen, M. S. Allen, A. L. Fannin, B. R. Wenner, J. W. Allen, M. S. Allen, and R. Magnusson, "Properties of mixed metal – dielectric nanogratings for application in resonant absorption , sensing , and display," **56**(12), (2017).

[45] Z. Su, J. Yin, and X. Zhao, "Soft and broadband infrared metamaterial absorber based on gold nanorod / liquid crystal hybrid with tunable total absorption," Nat. Publ. Gr. (November), 1–9 (2015).

[46] L. Wang, Y. Huang, C. Li, J. Chen, and X. Sun, "Hierarchical composites of polyaniline nanorod arrays covalently-grafted on the surfaces of graphene @ Fe 3 O 4 @ C with high microwave absorption performance," Compos. Sci. Technol. **108**, 1–8 (2015).

[47] L. Zhou, C. Zhao, B. Giri, P. Allen, X. Xu, and H. Joshi, "High Light Absorption and Charge Separation E ffi ciency at Low Applied Voltage from Sb-Doped SnO 2 /BiVO 4 Core/Shell Nanorod- Array Photoanodes," (2016).

[48] S. Baek, J. Noh, C. Lee, B. Kim, M. Seo, and J. Lee, "Plasmonic Forward Scattering Effect in Organic Solar Cells : A Powerful Optical Engineering Method," **1**, 1–7 (2013).

[49] D. Qu, F. Liu, X. Pan, J. Yu, X. Li, W. Xie, Q. Xu, and Y. Huang, "Plasmonic Core-Shell Nanoparticle Enhanced Optical Absorption in Thin Film Organic Solar Cells," 924–928 (2011).

[50] J. Grandidier, D. M. Callahan, J. N. Munday, and H. A. Atwater, "Light absorption enhancement in thin-film solar cells using whispering gallery modes in dielectric nanospheres," Adv. Mater. **23**, 1272–1276 (2011).

[51] Z. Yang, A. Shang, L. Qin, Y. Zhan, C. Zhang, P. Gao, J. Ye, and X. Li, "Broadband and wide-angle light harvesting by ultra-thin silicon solar cells with partially embedded dielectric spheres," Opt. Lett. **41**, 1329 (2016).

[52] B. Wang and P. W. Leu, "High index of refraction nanosphere coatings for light trapping in crystalline silicon thin film solar cells," Nano Energy **13**, 226–232 (2015).

[53] C. Liu, C. C. Mi, S. Member, and B. Q. Li, "Energy Absorption of Gold Nanoshells in Hyperthermia Therapy," **7**(3), 206–214 (2008).

[54] T. Y. Olson, A. M. Schwartzberg, C. A. Orme, C. E. Talley, B. O. Connell, and J. Z. Zhang, "Hollow Gold - Silver Double-Shell Nanospheres : Structure , Optical Absorption , and Surface-Enhanced Raman Scattering," 6319–6329 (2008).

[55] Z. Wang, X. Quan, Z. Zhang, and P. Cheng, "Journal of Quantitative Spectroscopy & Radiative Transfer Optical absorption of carbon-gold core-shell nanoparticles," **205**, 291–298 (2018).

[56] J. Li, S. K. Cushing, J. Bright, F. Meng, T. R. Senty, P. Zheng, A. D. Bristow, and N. Wu, "Ag@Cu_2O Core-Shell Nanoparticles as Visible-Light Plasmonic Photocatalysts" **3**, 47-51 (2013).

[57] B. Q. Li and C. Liu, "Multi-scattering of electromagnetic waves by nanoshell aggregates," (2012).

[58] C. F. Bohren and D. R. Huffman, “Absorption and scattering of light by small particles,” vol. 1, no. 1. 1983.

[59] C. Liu and B. Q. Li, "Computational multiscattering of spherical multilayered gold nanoshells," J. Phys. Chem. C **115**, 5323–5333 (2011).

[60] S. Seymour, “Addition Theorems for Spherical Wave Functions,” *Q. Appl. Math.,* vol. 19, no. 1, pp. 15–24, 1961.

[61] O. R. Cruzan, “Translational addition theorems for spherical vector wave functions,” *Q. Appl. Math.*, vol. 20, pp. 33–40, 1962.

[62] M. Kerker, D.-S. Wang, and C. L. Giles, “Electromagnetic scattering by magnetic spheres,” *J. Opt. Soc. Am.*, vol. 73, no. 6, p. 765, 1983.

[63] Kerker, M, “The Scattering of Light and Other Electromagnetic Radiation,” Chap (Vol. 7), 1969.

[64] A. Taflove and S. C. Hagness, “Computational Electrodynamics: The Finite-Difference Time-Domain Method,” Third Edition. 2005.

[65] H. Yang, B. Q. Li, X. Jiang, and W. Yu, "Nano-fabrication of depth-varying amorphous silicon crescent shell array for light trapping," Nanotechnology. **28**, 505301 (2017).

[66] C. Liu and B. Q. Li, "Energy Absorption in Gold Nanoshells," **23**, 74–82 (2013).